UNSTEADY TWO-PHASE FLOW INSTRUMENTATION AND MEASUREMENT

Thesis by

Robert J.N.Bernier

In Partial Fulfillment of the Requirements

for the Degree of

Doctor of Philosophy

California Institute of Technology

Pasadena, California

1982

(Submitted August 20,1981)

ACKNOWLEDGMENT

ABSTRACT

The performance of a transverse field electromagnetic flowmeter in a steady two-phase flow was investigated analytically for a disperse and an annular flow regime. In both cases the flowmeter output voltage was found to be proportional to the mean velocity of the liquid phase. Experiments in a steady air-water mixture showed good agreement with the analysis.

An impedance void fraction meter was designed and built to conduct measurements of unsteady void fractions. Short electrodes excited by voltages of opposite polarity were used in combination with a highly sensitive signal processor. The steady state calibration indicated that the meter was somewhat sensitive to the void fraction distribution for the bubbly flow regime. However, the transition to a churn turbulent regime greatly affected the meter steady state response. The dynamic capability of the void fraction meter was estimated by comparison of the statistical properties of the voltage fluctuations in a nominally steady bubbly flow with those of a shot-noise process. The filter function associated with the finite volume of the electric field within the fluid cell could be determined from the measured autocorrelation function and was shown to be mainly a function of the velocity of the disperse phase. Also some properties of the disperse phase could be inferred from the statistical analysis.

Two void fraction meters were used to measure the propagation speed of kinematic shocks in an air-water bubbly mixture for various void fractions and water flow rates. The relative velocity of the disperse phase calculated from these measurements decreased with an increase in the disperse phase concentration. However, this effect disappeared at higher

water flow rates and the relative velocity became independent of void fraction. Measurements of the propagation speed of shocks of decreasing strength provided a good verification of the kinematic wave theory. The shock thicknesses could also be determined leading to the conclusion that an important diffusion mechanism was responsible for arresting the steepening of the wave.

Cross-correlations of the fluctuating voltage of two void fraction meters in a steady bubbly flow were determined. The speed measured by this technique was identified as the infinitesimal wave speed of the void fraction and not the velocity of the dispersed phase as postulated by some authors. The normalized cross-correlation maxima showed that the small amplitude void fraction disturbances were short-lived structures, which were created and diffused on a continuous basis. The cross spectral density revealed that the waves present in these disturbances were non-dispersive.

TABLE OF CONTENTS

TABLE OF CONTENTS (continued)

TABLE OF CONTENTS (continued)

TABLE OF CONTENTS (continued)

TABLE OF CONTENTS (continued)

LIST OF FIGURES

LIST OF FIGURES (continued)

LIST OF FIGURES (continued)

LIST OF FIGURES (continued)

LIST OF FIGURES (continued)

LIST OF FIGURES (continued)

LIST OF TABLES

NOMENCLATURE

a	Inner cylinder radius
b	Electromagnetic flowmeter wall radius
d	Manometer displacement
e	Integer
f	Function of the radial coordinate
h	Filter function
h*	Filter function
i	$\sqrt{-1}$
j	Average volumetric flux
j_g	Gas volumetric flux
j_ℓ	Liquid volumetric flux
j_{gj}	Gas drift flux
j*	Current flux
k	Filter function scaling factor
ℓ	Distance between pressure taps
m	Impedance void fraction meter steady state calibration slope
n	Integer
p	Pressure
q	Outward normal
r	Radial coordinate
t	Time
t_o	Characteristic time
t_e	Point in time
u	Liquid velocity
u*	Nondimensional liquid velocity

NOMENCLATURE (continued)

u_s	Liquid velocity below the kinematic shock
v	Gas velocity
v^*	Nondimensional gas velocity
v_s	Disperse phase structure velocity
$v_{g\ell}$	Disperse phase relative velocity
$v_{s\ell}$	Disperse phase structure relative velocity
x	Stationary stochastic process
y	Stationary stochastic process
z	vertical coordinate
A	Pipe cross-section
B	Magnetic field intensity
C	Capacitance
C_i	Infinitesimal wave speed
C_i^*	Infinitesimal wave speed relative to the liquid velocity
C_s	Kinematic shock speed
C_s^*	Kinematic shock speed relative to the liquid velocity
C_s^{**}	Speed of kinematic shocks with decreasing strength
D	Bubble diameter
E	Expected value operator
H	Filter function Fourier transform
L_o	Characteristic length
P	Probability density function
Q	Volumetric flow rate
R	Resistance
R	Correlation function

NOMENCLATURE (continued)

R^* Correlation function

S Power spectrum function

T Time interval

U Propagation speed of a permanent wave form

U_o Characteristic speed

V Void fraction meter output voltage

V_1 Upstream void fraction meter voltage

V_2 Downstream void fraction meter voltage

W Cylinder axial velocity

X Complex attenuation factor

Z Electrical impedance

α Void fraction

α_o Void fraction initial value

β Kinematic wave diffusion coefficient

δ Delta function

δ^* Shock thickness

ϵ Dielectric constant

ϵ_o Free space permittivity

η Number of bubbles per unit time

θ Azimuthal coordinate

$\theta_{\tilde{V}_1 \tilde{V}_2}$ Cross-spectral density polar angle

κ Filter constant

κ^* Filter constant

λ Wavelength

μ Poisson distribution parameter

NOMENCLATURE (continued)

ν	Kinematic viscosity
ξ	Wave coordinate
ρ	Density
σ	Conductivity
σ_o	Conductivity of a continuum
σ_i	Conductivity of spherical inclusions
τ	Time
τ^*	Cross-correlation time delay
τ'	Wave time delay
τ_b	Volume of a bubble
ϕ	Electrical potential
ϕ^*	Electrical potential disturbance
Φ	Normalized cross-correlation function
χ	Viscous relaxation time
ω	Circular frequency

Subscripts:

1	Condition below a kinematic shock
2	Condition above a kinematic shock
a	Air
g	Gas
ℓ	Liquid
m	Spatial average
SP	Single-phase
TP	Two-phase

NOMENCLATURE (continued)

~   Vector

Superscripts:

~   Fluctuating quantity

—   Average value

I. INTRODUCTION

1.1 General Background

Multi-phase and/or multi-component flows have been part of our technology for quite a long time. Chemical plants have used slurries and fluidized beds well before a renewed interest in these flows was spurred by concerns over the safety of nuclear power plants. The momentum imparted to the research in this field is likely to continue with the emerging technology of synthetic fuels; the latter has reached the critical stage of being scaled up to commercial size. The success of its implementation will require a concerted effort toward improvements in the control and instrumentation of a process involving multi-phase flows [28].

The progress in instrumentation, component design and processes is closely linked to our understanding of the mechanics of these flows. Examples of devastating effects of these flows are numerous in the literature. For instance, cavitation erosion is responsible for the premature replacement of costly pump impellers [27]. Let-down valves in coal gasification systems may last only a few days in the adverse environment of coal slurries [11]. In general, it is not possible to eliminate these problems, but a better understanding of these flows combined with the proper choice of material can extend significantly the life of a component. Thermohydraulic instabilities associated with these flows have even more serious implications. They can jeopardize the integrity of the entire plant by causing severe mechanical

vibrations. They also disturb control systems and affect the heat transfer mechanisms. Recently, General Electric had to modify the Mark I nuclear reactor design because of the structural overloads created by the rapid condensation of vapor when forced into a pool of water (chugging instability) [17]. Three Mile Island is also illustrative of the damage caused by a boiling crisis initiated by an improper control of the reactor.

The study of these instabilities is greatly complicated by a multitude of possible flow regimes. In a two-phase flow, these regimes cover the whole range of interface topologies. A wide variety of names has been used to describe these types of flow and their classification, although useful, remains highly subjective. For a vertical upward flow Hewitt [7] distinguishes five dominant patterns as illustrated in Fig. 1.1a;*the bubbly flow, the slug flow, the churn flow, the annular flow, and the wispy-annular flow. The mechanisms leading to the establishment of a particular flow regime are complex. However, their occurrence is qualitatively depicted on a flow regime map as in Fig. 1.1b. The superficial momentum fluxes of each phase determine an area where each flow regime is likely to exist. In practice, the flow regime boundaries are not clearly defined and more than one flow pattern can coexist in their vicinity. One of the difficulties in modeling a two-phase flow is due to the distinctive interphase and/or wall mass, momentum and energy transfer properties of each flow regime. Following a disturbance, a steady flow regime can recast itself in a succession of other regimes seeking an equilibrium between internal and imposed pressure drops.

---

*Figures are at the end of each chapter.

-3-

Thermohydraulic instabilities are numerous and their description is summarized in a review paper by Bouré et al. [6]. In addition to the usual system of acoustic waves, these instabilities are excited by a system of kinematic waves, sometimes called density or continuity waves because their speed is close to the convective speed of the fluids. Although these systems of waves are coupled, high-frequency instabilities are generally associated with dynamic waves while kinematic waves are characterized by a low frequency spectrum. Kinematic waves are usually more important in two-phase flow instabilities. They are usually considered as part of the triggering mechanisms which lead to a change in flow regimes. Self-sustained density wave oscillations are frequently observed in boiling systems and are extensively described in Ref. [5].

The idea of kinematic waves was first introduced by Lighthill and Whitham [30,31] to analyze flood waves and traffic on highways, and by Kinch [26] who applied it to sedimentation processes. Subsequently, it was extensively used by Zuber [48] and Wallis [45] to describe the propagation speed of the void fraction in a two-phase disperse flow regime. Zuber and Staub [49] also carried out measurements of such waves in pipe flows of a water-vapor system perturbed by small amplitude oscillation of the heating power to the test section. The experimental results showed good agreement with the kinematic wave formulation.

1.2 Goals of the Research

The measurement of both systems of waves can yield valuable information with which to assess the validity of various models of

multi-phase flows. Experimental studies on acoustic wave propagation are numerous, but little is known about kinematic waves. It is the purpose of this thesis to explore in more detail the propagation of the void fraction in the form of waves.

The lack of data on kinematic waves is not due to a lack of interest in the topic, but rather to limited availability of instruments with adequate dynamic response. Reviews of two-phase flow instruments (see, for example, Hewitt [20,21] and Jones and Delhaye [25]) emphasize the fact that few instruments can be used for transient measurement of the void fraction. For instance, the whole class of local probes is not adequate because of the intrinsic time averaging process involved in the measurement. This thesis first presents the development and evaluation of instruments designed for this purpose. This is followed by a presentation of experimental results on kinematic shocks in an air-water bubbly system. These results are then used to establish the existence of a natural system of small amplitude waves in a nominally steady bubbly flow.

1.3 Electromagnetic Flowmeter

The first instrument we investigated was the transverse field electromagnetic flowmeter. Although not used during the course of our experimental work, we felt that this instrument had some unexplored potential in two-phase flow applications. Despite the experiments of Heineman et al. [18] and later of Hori et al. [22], it is quite surprising that the electromagnetic flowmeter has not been more widely used. In Chapter II, along with steady state data, we present some

theoretical considerations on the behavior of an electromagnetic flow-
meter in both bubbly and annular flow regimes.

1.4 Impedance Void Fraction Meter

In the past, the only accessible method to measure transient void
fraction was the X-ray beam attenuation technique.   It has been suc-
cessfully used in a wide variety of flow configurations by many
investigators, among them Schrock et al. [41] and Zuber et al. [50].
In recent years, the γ-ray attenuation technique has become a competi-
tive substitute. Larger sources of radioactive material and improve-
ment in the detection system have increased their dynamic response.
Time rise of the order of 20 ms is reported by Taylor et al. [44].
Ultrasonic detectors are still in the process of being evaluated, but
the preliminary tests of Arave and Fickas [1] suggest that these may
hold some promise.

The impedance void fraction meter offers an alternative for
transient measurements because of the simplicity of its construction.
The potential for good dynamic response was first recognized by
Orbeck [38] and later by Olsen [37]. However, most investigators have
used this technique in steady two-phase flows; the exceptions,to our
knowledge,are the work of Cimorelli and Evangelisti [9], Garrard and
Ledwidge [16], and more recently of Jallouk et al. [24], who have
attempted unsteady dynamic measurements.

The potential dynamic capability of the impedance void fraction
meter has prompted us to explore the use of these devices to observe
the propagation of kinematic waves. In Chapter III we report on the

design of our own impedance void fraction meter and present the results of its steady state calibration for different water volumetric flow rates.

1.5 Dynamic Calibration of the Impedance Void Fraction Meter

The dynamic calibration of this class of void fraction meter is a topic which is not addressed in the literature. The statistical analysis of the fluctuating output voltage of the meter in a steady bubbly flow will lead us in Chapter IV to an estimation of its dynamic response. This analysis goes beyond that of Garrard and Ledwidge [16] who considered the implications of the probe "noise." However, their conclusions were too vague for any practical application. By assuming a specific stochastic process, some average physical properties of the disperse phase are correctly predicted. A better understanding of the dynamic operation of the meter finally permits us to make some suggestions for future improvement.

1.6 Measurements of Kinematic Shocks

In the first part of Chapter V the kinematic wave theory as formulated by Zuber [48] is introduced. This formulation is equivalent to Wallis's [46] drift flux model. However, Zuber's approach is more readily considered as a particular case of the general equations describing a bubbly two-phase flow. The properties of kinematic shocks are then used in a manner similar to that of Nicklin [36] to determine the relative velocity of the disperse phase for various flow conditions. Data on kinematic shock thickness are also presented.

1.7 Kinematic Waves in a Steady Bubbly Flow

In Chapter VI, cross-correlation measurements of the fluctuating voltages in a nominally steady bubbly flow are presented. The velocity deduced from these measurements is reexamined in terms of the results obtained in Chapter V. It is identified as the speed of small amplitude kinematic waves and not the velocity of the disperse phase, as postulated by Cimorelli and Evangilisti [10] and Garrard and Ledwidge [16]. It is also shown that these void fraction disturbances are structures having a short life. The kinematic waves in these disturbances are nondispersive at least for wavelengths that could be detected by the impedance void fraction meter.
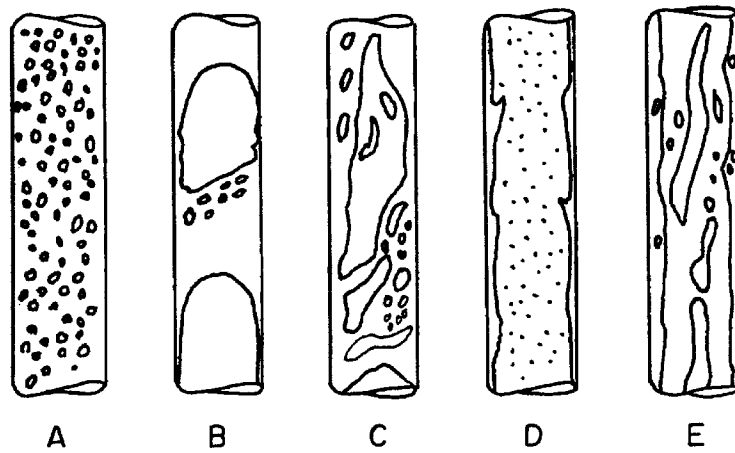
Figure 1.1a   Two-phase flow regimes; A- bubbly flow, B- slug flow,
C- churn flow, D- annular flow, E- wispy-annular flow,
(Ref.7).
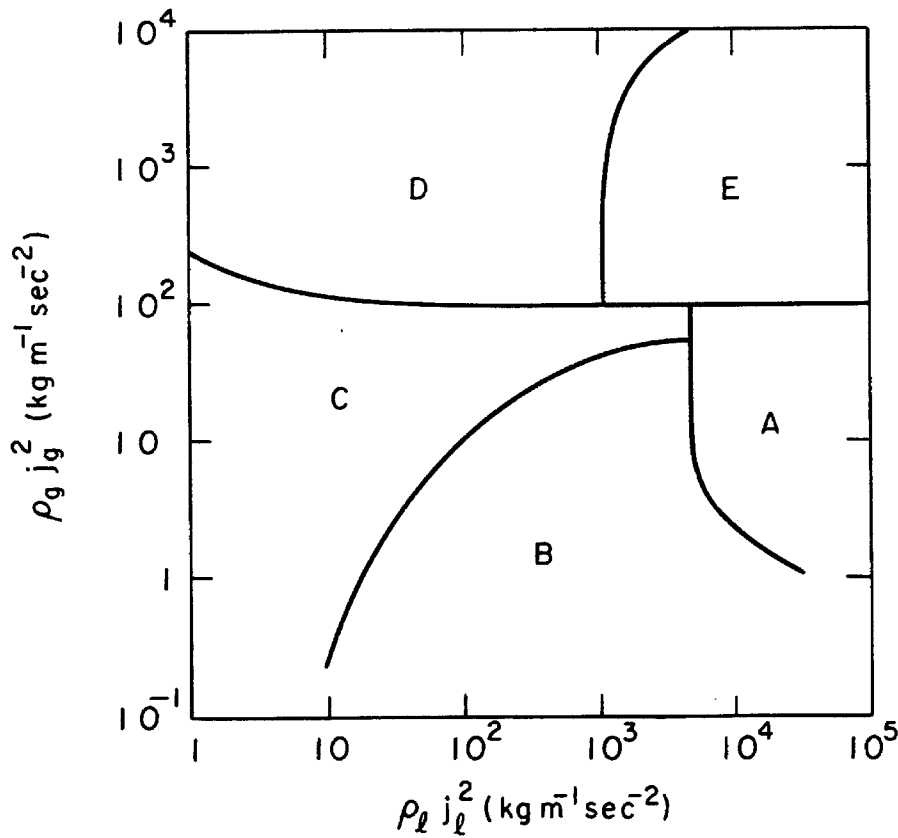
Figure 1.1b   Example of a flow regime map for air-water at atmospheric
pressure and steam-water at high pressure: $\rho_g j_g^2$ and $\rho_\ell j_\ell^2$
are the superficial momentum fluxes of the gas and liquid
phase respectively. The letters refer to the flow regimes
illustrated in Fig.1.1a (Ref.7).

II. TRANSVERSE FIELD ELECTROMAGNETIC FLOWMETER IN TWO-PHASE FLOW

2.1 Introduction

There is presently considerable activity directed toward the development of instruments to measure the mass or liquid flow rate in two-phase flows. Most of this effort is directed toward the investigation of the turbine flowmeter and the drag disk used in combination with a densitometer. However, little attention has been devoted to the use of the induction flowmeter in two-phase flows. Early experiments of Heineman et al. [18] and Hori et al. [22] were intended to promote this type of flowmeter as a void fraction meter. Their motivation was based on the assumption that even in a two-phase flow, the induction flowmeter measures the mean velocity of the conducting phase.

The intent of this chapter is to present a theoretical analysis of the transverse field electromagnetic flowmeter in a two-phase flow. The homogeneous and annular flow regimes are considered. An experimental investigation reported in Section 2.3 shows good agreement with the analysis.

2.2 Theoretical Considerations

2.2.1 Principle of Operation in Single-Phase Flows

The electromagnetic flowmeter for single phase flow applications has been extensively analyzed by Shercliff [42]. For an axisymmetric velocity profile $u(r)$ perpendicular to a uniform D.C. magnetic field of intensity B, the electric potential ϕ satisfies the following Poisson's

equation

$$\nabla^2 \phi(r,\theta) = B \sin \theta \frac{\partial}{\partial r} u(r) \cdot \qquad (2.1)$$

This equation demonstrates that the electrical potential generated by the fluid motion is independent of its electrical properties. However, for a confined flow, the formal solution of Eq. (2.1) depends on the electrical properties of the fluid and the boundary conditions at the solid containing wall of the device. Throughout this analysis, we will consider the case for which the impedance of the wall is much larger than that of the fluid in contact. Then, for insulating walls, the solution of Eq. (2.1) for the geometry illustrated in Fig. 2.1 is

$$\phi(b,\theta) = \frac{B \sin \theta}{\pi b} \int_0^b 2\pi r\, u(r)\, dr \cdot \qquad (2.2)$$

The integral in this result is precisely the volume flow rate, Q, and one of the special advantages of this instrument is that the result is insensitive to the form of $u(r)$.

The maximum voltage difference is obtained in a direction perpendicular to both the fluid motion and the magnetic field

$$\phi(b,\frac{\pi}{2}) - \phi(b,\frac{3\pi}{2}) \equiv \Delta\phi = \frac{2BQ}{\pi b} \qquad (2.3a)$$

or alternatively, if the volumetric flow rate, Q, is expressed in terms of the mean velocity $u_{m_{SP}}$ of the single phase flow,

$$\Delta\phi_{SP} = 2bB\, u_{m_{SP}} \cdot \qquad (2.3b)$$

The maximum output voltage measured at the wall is therefore pro-
portional to the average velocity of the fluid, and is independent of
the electrical properties of the fluid. Similar conclusions apply when
the fluid and the wall have the same conductivity. However, when both
are good insulators, the detection of the voltage is limited by the rela-
tive magnitude of the fluid impedance to the indicating circuit impedance.

2.2.2 Disperse Two-Phase Flow without Relative Motion

The case of a homogeneous two-phase flow with a disperse phase
moving at the speed of the continuous phase was first considered by
Fitremann [15]. His analysis was based on a perturbation of the current
flux circulating within the fluid due to the presence of insulated
spheres which are small compared to the size of the flowmeter electrodes.
For a nonconfined flow, the interpretation of his results leads to the
conclusion that the output voltage is smaller in a homogeneous mixture
than in a single phase flow for identical velocity fields. Due to some
inconsistency in his derivation and in view of Eq. (2.1), this result is
believed to be erroneous. The case of a disperse flow in a rectangular
channel is, however, treated correctly. The output voltage of the flow-
meter is not affected by the disperse phase.

This result could be readily inferred by considering the mixture as
a fluid having some effective homogeneous properties. As long as the
pick-up circuit impedance remains large compared to the fluid effective
impedance, the voltage readout is not affected by a change in the elec-
trical properties of the mixture. The voltage output is therefore
proportional to the average velocity of the homogeneous mixture, and

consequently to the mean velocity $u_{m_{TP}}$ of the liquid phase,

$$\Delta\phi_{TP} = 2bB\, u_{m_{TP}} \, . \tag{2.4}$$

When a relative velocity exists between the two phases, the argument which led us to Eq. (2.4) becomes ambiguous. For instance, it is not clear if the contribution to the potential caused by the disperse phase is due to its mere presence or rather to the motion. This makes quite a difference in interpreting Eq. (2.3a) when the gas and liquid phases are not moving at the same speed. The annular two-phase flow model presented in Section 2.2.4 will enable us to shed some light on that question.

2.2.3 Homogeneous Two-Phase Flow in an Oscillating Magnetic Field

It was observed by Cushing [12] that when an oscillating magnetic field is used (as in most transverse field electromagnetic flowmeters) the electric potential of Eq. (2.1) is no longer independent of the electrical properties of the fluid. The question therefore arises as to whether a change in the effective electrical properties due to the presence of the disperse phase will affect significantly the potential induced by the moving mixture.

Accounting for the charge flux density in Maxwell's equations, the right-hand side of Eqs. (2.1) through (2.3) are multiplied by an attenuation factor X, taking the form

$$X = \frac{[1 + (\frac{\omega\varepsilon_0}{\sigma})^2 \varepsilon(\varepsilon-1)] + i[\frac{\omega\varepsilon_0}{\sigma}]}{1 + (\frac{\omega\varepsilon_0\varepsilon}{\sigma})^2} \tag{2.5}$$

This attenuation factor is a function of the frequency ω of the imposed magnetic field, the conductivity σ of the fluid and its dielectric constant ε, and the permittivity of the free space ε_o. Moreover, it displays a component in quadrature which is lost at the signal processing level whenever a demodulation circuit is used.

Calculations of the in-phase component of the attenuation factor were made for an air-water bubbly mixture. The effective conductivity σ_{TP} and dielectric constant ε_{TP} of the two-phase homogeneous flow were determined from Maxwell's [33] formula for composite materials:

$$\sigma_{TP} = \sigma_w \left[1 - \frac{3\alpha}{\left(\dfrac{2\sigma_w + \sigma_a}{\sigma_w - \sigma_a}\right) + \alpha} \right] , \qquad (2.6)$$

and similarly,

$$\varepsilon_{TP} = \varepsilon_w \left[1 - \frac{3\alpha}{\left(\dfrac{2\varepsilon_w + \varepsilon_a}{\varepsilon_w - \varepsilon_a}\right) + \alpha} \right] . \qquad (2.7)$$

The subscripts w and a refer to the electric properties of the water and air, respectively. Substituting these expressions in Eq. (2.5), the attenuation factor becomes a function of the void fraction α .

Although not valid for large concentrations of the disperse phase, Maxwell's formula was nevertheless used in the large void fraction region to determine the qualitative trend of the attenuation factor. Figure 2.2 shows the resulting in phase component for both pure and tap water as a function of the void fraction. The attenuation factor is normalized by the value corresponding to zero void fraction. These results are calculated for a magnetic field oscillating at 328 Hz,

which is the frequency of the flowmeter used in the experiment described at the end of this chapter. For pure water, the presence of the disperse phase has a significant effect only at large void fraction. As the conductivity is increased (as in the case of tap water), the effect does not appear until void fractions even closer to unity which could not be shown on Fig. 2.2. It should be emphasized that these results apply only when the continuous phase is water. If the continuous phase becomes the gas as it would at some high void fraction, not only would the attenuation factor tend to zero, but the high impedance of the mixture would prohibit any practical measurement. Moreover, the assumption of insulated walls used to derive Eq. (2.3) would cease to be valid.

2.2.4 Annular Two-Phase Flow

The interest in investigating the response of the transverse field electromagnetic flowmeter in an annular two-phase flow is twofold. First, such flows are frequently encountered in practice. As we shall demonstrate, the induction flowmeter turns out to be quite a useful instrument for this flow pattern. Secondly, the annular two-phase flow model will provide some insights on the way the gaseous phase contributes to the generation of the electric potential.

In an annular two-phase flow, the gas flows at the center of the pipe through an approximately circular cross section surrounded by an annulus of liquid in contact with the wall. For the purpose of this analysis, the gas phase is simulated by a cylindrical insert of radius a, moving in the axial direction at a constant speed W. The conducting liquid phase flows between the wall of the flowmeter (radius b) and the cylinder, both being insulated.

For an axisymmetric velocity profile with a uniform magnetic field perpendicular to the flow, we need to solve Eq. (2.1) for the geometry illustrated in Fig. 2.3. The boundary conditions are expressed in terms of the continuity of the current density, $\underset{\sim}{j}^{*}$, normal to the wall and the cylinder. The general expression is given by Ohm's law for a moving medium:

$$\underset{\sim}{j}^{*} \cdot \underset{\sim}{q} = \sigma(-\nabla\phi + \underset{\sim}{u}(r) \times \underset{\sim}{B}) \cdot \underset{\sim}{q} \quad , \tag{2.8}$$

where $\underset{\sim}{q}$ is the outward normal unit vector. Since the wall and the cylinder are insulated, the left-hand side of Eq. (2.8) is zero at the radii a and b. The no-slip condition of the fluid leads to

$$\left.\frac{\partial\phi}{\partial r}\right|_{r=b} = 0 \qquad \text{with} \quad u(b) = 0 \quad , \tag{2.9}$$

and

$$\left.\frac{\partial\phi}{\partial r}\right|_{r=a} = WB\sin\theta \quad \text{with} \quad u(a) = W \quad \cdot \tag{2.10}$$

A particular solution of Eq. (2.1) as mentioned in Ref. [42] is

$$\phi(r,\theta) = f(r)\sin\theta \tag{2.11}$$

which, when substituted into Eq. (2.1), yields

$$f''(r) + \frac{1}{r}f'(r) - \frac{1}{r^2}f = Bu' \tag{2.12}$$

where the prime denotes differentiation with respect to r. This differential equation can be integrated in two ways. The classical form which leads to the solution of the single phase flow problem is obtained

by multiplying each side of Eq. (2.12) by r^2 and integrating:

$$\left[r^2 f'(r) - rf(r) \right]_a^b = r^2 B\, u(r) \Big|_a^b - 2B \int_a^b r\, u(r)\, dr \quad . \tag{2.13}$$

Upon evaluation at the radii a and b, and observing from the boundary conditions (2.9) and (2.10) that

$$f'(b) = 0 \tag{2.14}$$

and

$$f'(a) = BW \quad . \tag{2.15}$$

Eq. (2.13) can be written as

$$-bf(b) + af(a) = -2B \int_a^b r\, u(r)\, dr \quad . \tag{2.16}$$

The right-hand side of this last equation is a function of the potential f(b) at the wall of the flowmeter and the potential f(a) at the liquid-cylinder interface. The second integrated form of Eq. (2.12) will provide the means to express f(a) as a function of f(b). Equation (2.12) integrated differently gives

$$\left[f'(r) + \frac{f(r)}{r} \right]_a^b = B\, u(r) \Big|_a^b \quad . \tag{2.17}$$

Again, making use of the boundary conditions of Eqs. (2.14) and (2.15), the following relation is obtained:

$$f(a) = \frac{a}{b}\, f(b) \quad . \tag{2.18}$$

Substituting for f(a) in Eq. (2.16), the potential difference existing at the wall in a direction perpendicular to both the direction of the

magnetic field and the liquid velocity is

$$\Delta\phi = \frac{2bB \int_a^b 2\pi r\ u(r)\ dr}{\pi(b^2 - a^2)} \quad . \tag{2.19a}$$

This solution of the annular two-phase flow problem exhibits some remarkable properties. As in the case of a single phase flow, the voltage difference is not sensitive to the details of the axisymmetric velocity profile. Furthermore, we notice that Eq. (2.19) can be written as

$$\Delta\phi_{TP} = 2bB\ u_{m_{TP}} \tag{2.19b}$$

since the mean velocity $u_{m_{TP}}$ of the liquid phase is simply

$$u_{m_{TP}} = \frac{\int_a^b 2\pi r\ u(r)\ dr}{\pi(b^2 - a^2)} \quad . \tag{2.20}$$

The transverse field electromagnetic flowmeter will therefore measure the average velocity of the liquid phase and is unaffected by the radius of the gas core. Consequently this type of flowmeter can be very useful in two-phase annular flows. Also, Eq. (2.19) is seen to be totally independent of the cylinder speed. This implies that the contribution of the gaseous phase velocity to the potential is due to its presence alone and not to its motion. In a disperse two-phase flow with relative velocity of the phases, the volumetric concentration of the gas phase (and possibly its spatial distribution) is expected to be the dominating effect and not the gas flow rate.

For a known liquid volumetric flow rate, the voltage ratio of the single-phase to the two-phase annular flow regime can yield the value of the void fraction α according to the following expression

$$\alpha = \frac{a^2}{b^2} \equiv [1 - \frac{\Delta\phi_{SP}}{\Delta\phi_{TP}}] \quad . \tag{2.21}$$

Such measurements are reported by Hori et al. [22] for the case of stationary and insulated cylindrical inserts of different sizes placed at the center of the flowmeter. Tests were conducted with mercury and water. The agreement between the actual void fraction and the void fraction measured by the electromagnetic flowmeter is very good.

2.2.5 Extension of the Annular Flow Model to a Matrix of Cylindrical Bubbles

The annular two-phase flow model can be pushed one step further by considering a matrix of cylinders of radii a, which is small compared to the pipe radius b. Expanding Eq. (2.19a) in terms of the cylinder-to-pipe cross-section ratio a^2/b^2, the voltage difference is

$$\Delta\phi_{TP} = \frac{2bB}{\pi b^2} Q\ell \{1 + \frac{a^2}{b^2} + \frac{a^4}{b^4} + 0(\frac{a^6}{b^6})\} \tag{2.22}$$

where $Q\ell$ is the liquid volumetric flow rate. For a small value of the ratio a^2/b^2, the first order contribution of the cylindrical bubble to the electric potential is simply

$$\Delta\phi_{TP}^* \doteq \frac{2bB}{\pi b^2} Q\ell \frac{a^2}{b^2} \quad . \tag{2.23}$$

For cylinders close to the center of the pipe, the boundary conditions will be satisfied approximately. Summing up the effects of n cylinders

and superposing the undisturbed solution, one arrives at the following expression

$$\Delta\phi_{TP} \doteq \frac{2bB}{\pi b^2} Q\ell\{1 + \alpha\} \quad , \tag{2.24}$$

with α the void fraction defined in the usual manner as

$$\alpha = \sum_{e=1}^{n} \frac{a_e^2}{b^2} \quad . \tag{2.25}$$

The continuity equation for a two-phase flow is used to define an average velocity of the liquid phase $u_{m_{TP}}$

$$u_{m_{TP}} = \frac{Q\ell}{\pi b^2 (1 - \alpha)} \tag{2.26}$$

so that to the first order in α we obtain the now familiar result,

$$\Delta\phi_{TP} \doteq 2bB \ u_{m_{TP}} \tag{2.27}$$

which again says that the output voltage of the flowmeter is proportional to the mean velocity of the liquid phase.

Hori et al. [22] have also investigated the effect of a fixed matrix of insulated cylindrical rods. In most of the cases some of the rods were close to the wall of the flowmeter. Nevertheless, their experimental results agree very well with Eq. (2.27).

2.3 Performance of the Electromagnetic Flowmeter in a Bubbly Air-Water Mixture

2.3.1 Description of the Experiment

The performance of a 10.2 cm (4") I.D. transverse field Foxboro electromagnetic flowmeter with insulated walls was investigated in an

actual air-water bubbly mixture. To accommodate a 328 Hz excitation frequency for a good dynamic response, a variable A.C. power source in line with an oscillator was used instead of the 60 Hz commercial version. A low noise signal processor consisting of a 68 dB preamplifier and a demodulator was very effective in minimizing the electronic D.C. drift.

The experiments were conducted in the two-phase flow facility described in Section 3.4.1. The flowmeter was installed in the vertical test section 1.37 m above the air injector. A second electromagnetic flowmeter was used upstream of the injector to monitor the water flow rate. The void fraction was measured by the change in hydrostatic head (the method is described in Section 3.4.2).

The output signals of the flowmeters were simultaneously recorded on a tape and processed using an 8-channel digital Fourier analyzer. The Fourier analyzer offered the advantage of a wide range of averaging times for the measurement of the D.C. values (unlike most digital voltmeters). For this experiment, a 60-second sampling period was chosen, even though a 30-second period was shown to be adequate in preliminary tests.

The entire experiment was conducted at atmospheric pressure. For a constant water flow rate, data points were taken for increments of the gas flow rate. The observed flow patterns ranged from bubbly through transition and into the churn turbulent regime. The experiment was repeated for different water flow rates.

The results are shown in Fig. 2.4. The nondimensional grouping of the variables on the vertical axis is obtained from the theoretical

considerations presented in the previous sections. The output voltage

in a two-phase flow was shown to be proportional to the mean liquid

velocity $u_{m_{TP}}$ (Eq. (2.4)):

$$\Delta\phi_{TP} = 2bB \; u_{m_{TP}}$$

while the same result is true for a single phase with a mean velocity

$u_{m_{SP}}$ (Eq.(2.3b))

$$\Delta\phi_{SP} = 2bB \; u_{m_{SP}} \quad .$$

For a constant water flow rate, the relation between $u_{m_{SP}}$ and $u_{m_{TP}}$ is

given by the continuity of the liquid mass flow rate such that

$$u_{m_{TP}} = \frac{u_{m_{SP}}}{[1-\alpha]} \quad . \tag{2.28}$$

The dimensionless group $\frac{1}{[1-\alpha]} \frac{\Delta\phi_{SP}}{\Delta\phi_{TP}}$ is then obtained from the ratio of

Eqs.(2.3b) and (2.4) after substitution for $u_{m_{TP}}$. According to our analysis,

this parameter should be equal to unity for all void fractions. In the present

experiment, $\Delta\phi_{SP}$ corresponds to the output voltage of the monitoring flowmeter

while $\Delta\phi_{TP}$ corresponds to the output voltage of the flowmeter in the two-phase

test section.

2.3.2 Results

The results in Fig. 2.4 are remarkably consistent, falling

within a narrow 3% band around the mean value. The slip ratio (defined

as the gas-to-liquid velocity ratio) in the experiments varied from 2.18

to 1.17, yet no significant effect of this parameter could be observed

for the range of water flow rates considered. Although there is evi-

dence of a weak dependency on the void fraction (which is not under-

stood at this point), Eq. (2.4) seems to describe satisfactorily the

behavior of the transverse field electromagnetic flowmeter in a two-phase flow. It should be pointed out that, except for the lowest flow rate, some of the data points at large void fraction were taken in a churn turbulent flow regime. This unstable flow regime has some of the characteristics of both a disperse and an annular flow. Since it was shown that for these regimes the flowmeter measures the mean liquid velocity, it is not surprising that these points fall on a unique curve.

The long time averaging period used throughout the experiment does not rule out the induction flowmeter as a practical device for unsteady two-phase flow. As in the case of the single-phase flow, the frequency of the magnetic field must be an order of magnitude higher than the typical frequency of the unsteady flow to allow for the demodulation process. The noise level in the signal is also important. In a two-phase flow, the electronic noise is insignificant compared to the disturbances in the signal due to the presence of the disperse phase. Because of their uncorrelated nature, these fluctuations are conveniently identified with random noise. The RMS value of the noise during these experiments was found to be practically independent of the water velocities and gas flow rates. The resulting improvement in the noise-to-signal ratio as the water flow rate is increased can be seen in Fig. 2.5. The noise-to-signal ratio levels shown are still acceptable for measurements in steady oscillatory flow of small amplitude. Due to the random nature of the noise, the recovery of the fluctuating part of the output signal can be efficiently accomplished by averaging over a sufficient number of cycles.

2.4 Conclusion

Theoretical considerations and an experimental investigation for the case of a bubbly flow air-water mixture show that the transverse field electromagnetic flowmeter is a device measuring the mean velocity of the continuous phase and not the liquid flow rate as has sometimes been assumed (for example in Ref.[19]). As inferred from the annular two-phase flow analysis, no effect of the relative velocity of the disperse phase was observed at least for the range of slip ratios investigated in this experiment. The device seems to offer good possibilities for unsteady two-phase flow measurement, even in the case of small amplitude oscillatory flows, despite the appreciable noise level.
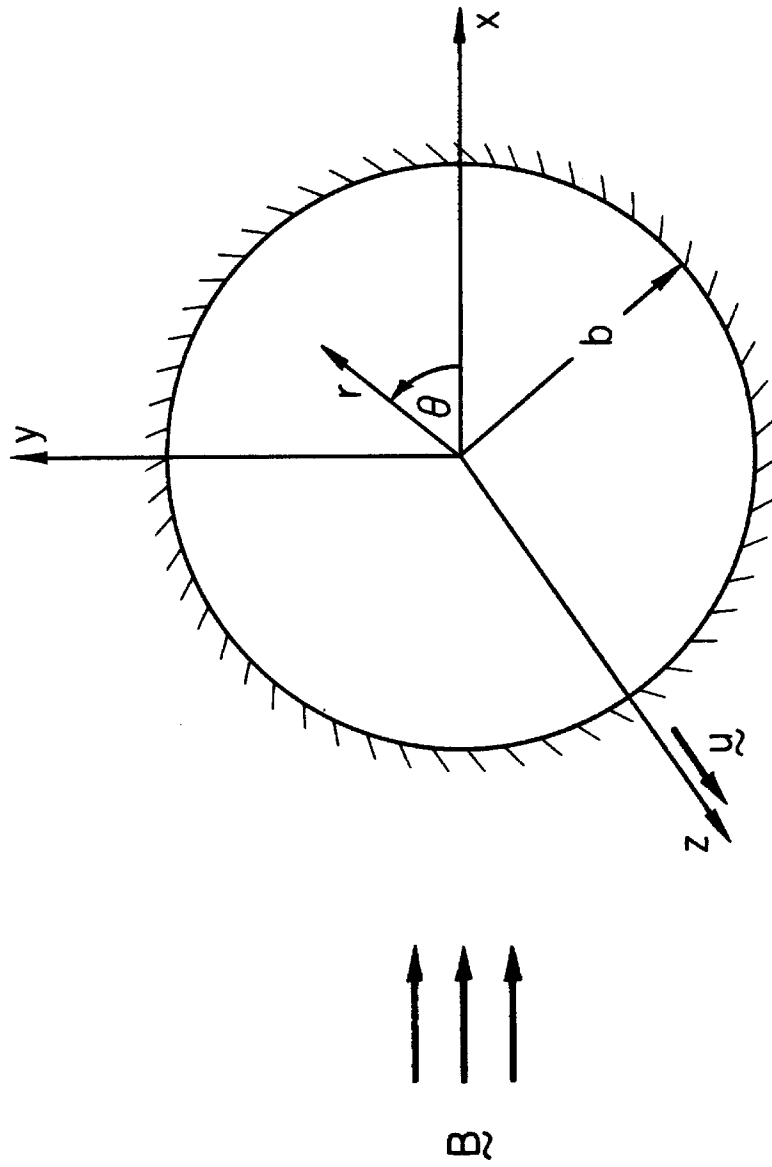
Figure 2.1 Schematic cross-sectional view of the transverse field electromagnetic flowmeter in a single-phase and/or two-phase homogeneous mixture leading to the solution of Eq.2.3 and 2.4.
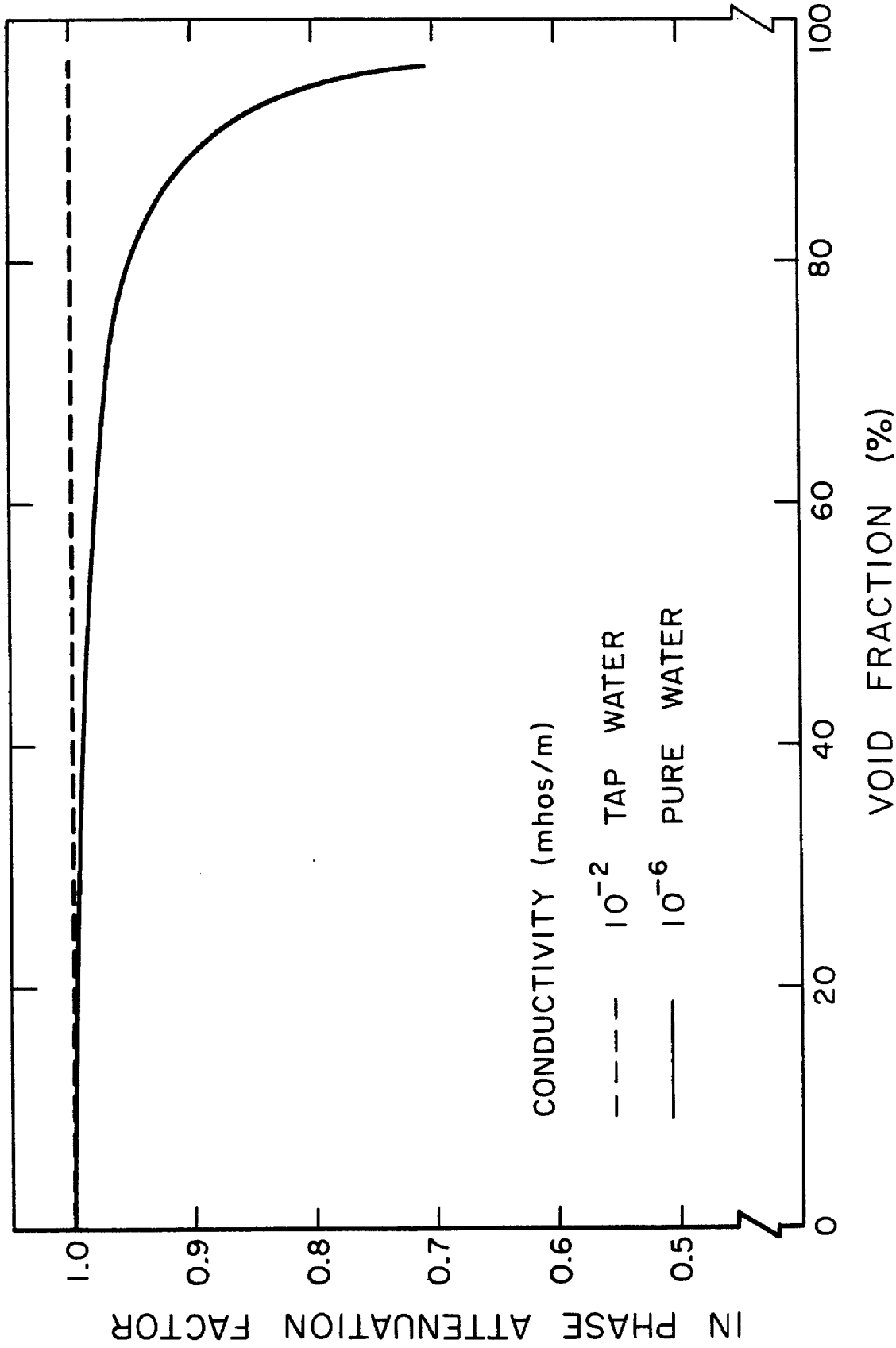
Figure 2.2 In-phase attenuation factor due to the effective electrical properties of a homogeneous two-phase flow mixture in an oscillating magnetic field. Water dielectric constant $\epsilon_w = 80$, magnetic field frequency: 328 Hz.
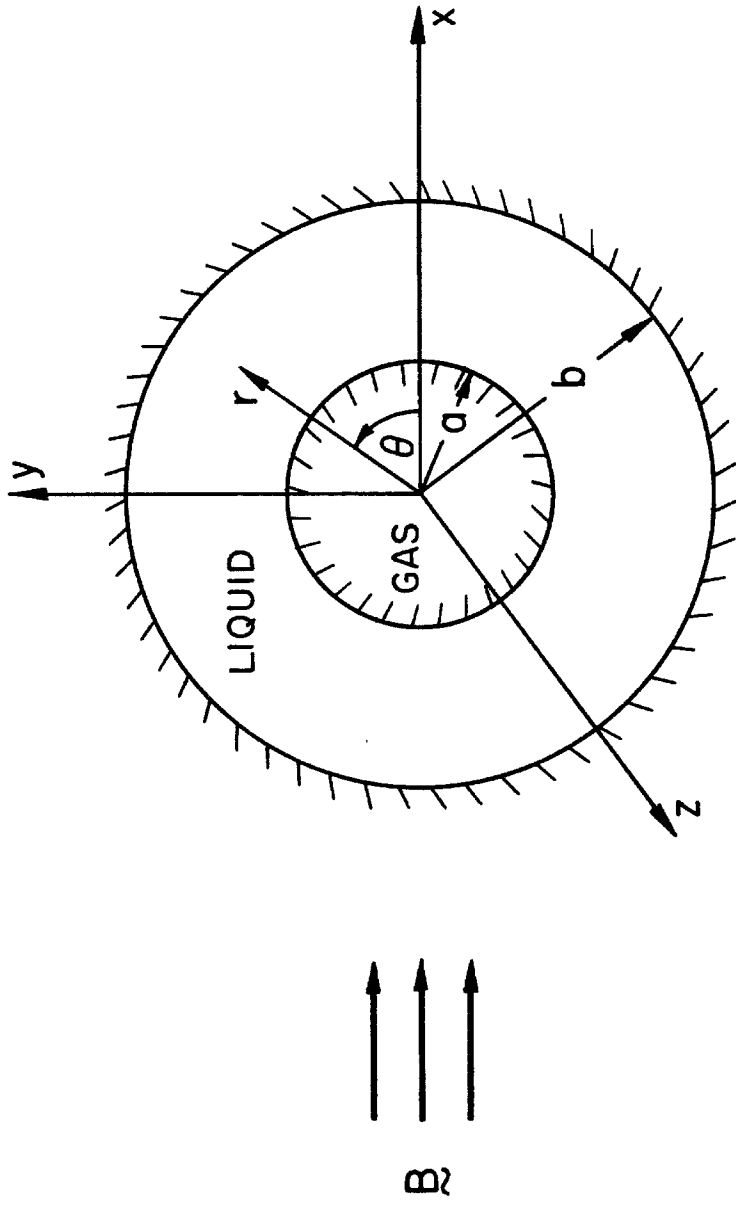
Figure 2.3   Schematic cross-sectional view of the transverse field electromagnetic flowmeter in a two-phase annular flow regime. The liquid is flowing in the positive z direction with an axisymmetric velocity profile. The velocity at the gas-liquid interface is constant.
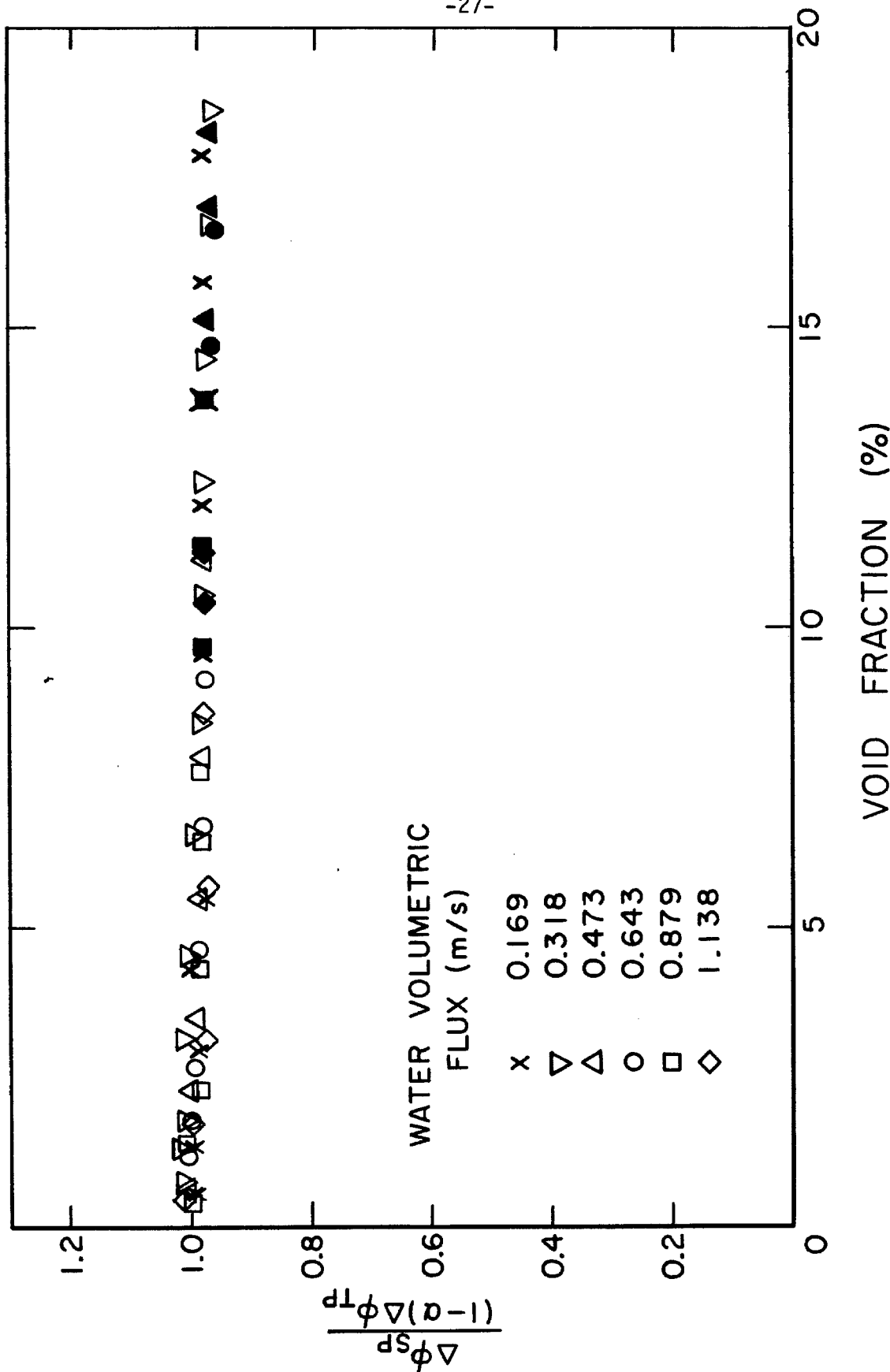
Figure 2.4 Steady-state performances of a 10.16 cm (4") I.D. Foxboro transverse field electromagnetic flowmeter in air-water bubbly and churn turbulent flow regimes. Data shown as solid points indicate the occurrence of the churn turbulent flow regime. The single and two-phase flow-meter outputs are respectively $\Delta\phi_{SP}$ and $\Delta\phi_{TP}$.
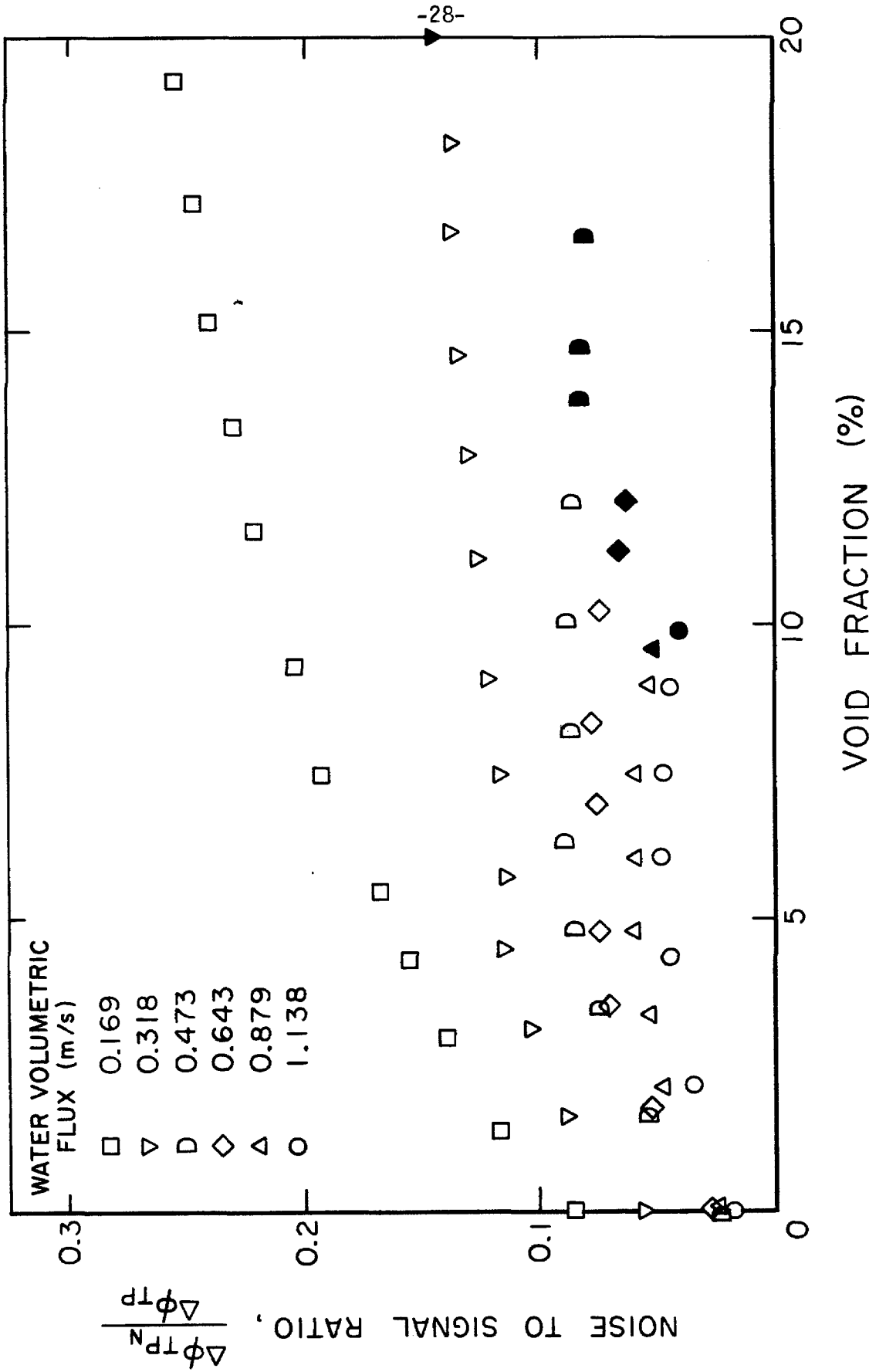
Figure 2.5 Noise-to-signal ratio measured in steady air-water bubbly and churn turbulent flow regimes. Data shown as solid points indicate the occurrence of the churn turbulent flow regime. The noise RMS value of the output voltage is $\Delta\phi_{TP_N}$, the voltage mean value is $\Delta\phi_{TP}$.

III. IMPEDANCE VOID FRACTION METER

3.1 Introduction

There seems to be general agreement among investigators that
transient void fraction measurements can be made with the electrical
impedance technique. However, there is surprisingly little discussion
of this in the literature. The lack of information on its dynamic
capability has motivated us in choosing this method over the more com-
monly used X-ray and γ-ray beam attenuation techniques for our experi-
ments on the kinematic wave propagation of the void fraction.

Believing that the impedance void meters investigated in the past
could benefit from some improvements, the technical aspect of our own
design is described in this chapter, followed by an evaluation of its
steady state performance in an air-water bubbly mixture. More will be
said in the next chapter about its dynamic response and the unique
method leading to its estimation.

3.2 General Considerations

3.2.1 Principle of Operation of the Impedance Void Fraction Meter

This type of instrument operates on the well known principle that
the bulk electrical impedance of a mixture is usually different from
the impedance of each constituent. A correlation between the void frac-
tion and the mixture impedance is possible as long as the disperse
phase and the liquid phase have dissimilar electrical properties. Gases
are generally poor conductors with a low dielectric constant, while
liquids if not good conductors will at least assume a higher value of
the dielectric constant due to a larger concentration of dipoles.

The measurement of the impedance takes place in a volume defined by the lines of an electric field associated with the electrode system. Because of the electric properties of the fluid, the impedance consists of capacitive and resistive components distributed over the volume. The simplest model would consist of a resistance and capacitance in parallel. As mentioned by Olsen [37], the polarization effect due to the ions in the liquid introduces an additional impedance localized in the vicinity of the liquid-electrode interface. Inversely proportional to the half power of the frequency, this parasitic impedance can be eliminated by a proper choice of the electric field frequency. If insulated electrodes are used, a proper model of the cell impedance should include the capacitive effect of the insulator.

3.2.2 Effective Electrical Properties of a Two-Phase Mixture

The effective electrical properties of a two-phase mixture depends greatly on the geometry of the gas-liquid interface. The case of a suspension of solid particles or bubbles has been the object of many investigations. The analytical treatment of the effect of a dilute suspension of spheres on the bulk conductivity of the mixture was first done by Maxwell [33]. Other models have subsequently followed to account either for the mutual influence of the inclusions as in the solutions of Meridith and Tobias [34] or to include the effect of a geometry departing from a spherical shape as in Weiner's formula [47].

The ideal conditions under which these models are developed rarely occur in practice and Maxwell's formula is as good as any to estimate the functional relation between the electrical properties of

the mixture and the void fraction. His solution is obtained by considering a dilute suspension of spheres having a conductivity σ_i in a continuous medium of conductivity σ_0. The spheres are contained within an imaginary larger sphere. In the far field, the disturbances on the uniform electric field are summed up and equated to the disturbance due to the imaginary sphere having an effective conductivity σ_{TP}. Solving for σ_{TP}, Maxwell arrived at the following expression

$$\frac{\sigma_{TP}}{\sigma_0} = 1 - \frac{3\alpha}{(\frac{2\sigma_0 + \sigma_i}{\sigma_0 - \sigma_i}) + \alpha} \tag{3.1}$$

where α is the volumetric concentration of disperse phase.

For the case of air bubbles in water, the water having a conductivity σ_w and a dielectric constant ε_w much larger than the air, Maxwell's formula reduces to

$$\frac{\sigma_{TP}}{\sigma_w} = 1 - \frac{3\alpha}{2 + \alpha} \tag{3.2}$$

while the effective dielectric constant becomes

$$\frac{\varepsilon_{TP}}{\varepsilon_w} = 1 - \frac{3\alpha}{2 + \alpha} \tag{3.3}$$

since the equations describing each effect are analogous.

Making use of these results in the parallel resistance capacitance model, the complex impedance Z of the fluid cell is

$$Z = \frac{R_w[1 - \frac{3\alpha}{2 + \alpha}]^{-1}}{i\omega R_w C_w + 1} \tag{3.4}$$

where R_w and C_w are the continuous phase resistance and capacitance.

The choice of the frequency ω and the value of the time constant $R_w C_w$ will determine the dominance of the resistive or capacitive part of the impedance. In either case the impedance of the fluid cell increases with the void fraction α. For reasonable values of the resistance or capacitance, changes in α of 1% are easily detectable.

3.2.3 Electrode System

Ideally, an impedance void fraction meter should have zero sensitivity to non-uniformities in the void distribution over the measuring volume. Each unit void should contribute equally to the change of the mixture impedance. For a representative average measurement of the void fraction, many authors suggest the use of a homogeneous electric field between the electrodes. A non-intrusive electrode system is also clearly preferable.

The circular pipe geometry in which most experiments are conducted can hardly satisfy these requirements simultaneously. Some compromises are necessary in working out the configuration of the electrodes. In search of the optimum shape, many electrode geometries have been investigated by Orbeck [38], Olsen [37], and others. Four general types of electrode systems have been used; within each type there are only minor differences related to the specific environment of the probe or the number of electrodes. These four types are:

    i)   Coaxial
   ii)   Parallel flat plates
  iii)   Wire grid
   iv)   Wall flush mounted circular arc.

Selecting the optimum type is a somewhat elusive task. The most popular design is the coaxial system because of the quasi-uniform electric field it generates when the inner-to-outer diameter ratio of the concentric electrodes is near unity. However, Olsen reports that this type of electrode is still sensitive to the void distribution and flow regimes. Some progress in improving this problem has been achieved by Merilo et al. [35]. They used three pairs of narrow electrodes equally spaced around the circumference of the pipe and a rotating electric field. By sampling sequentially the impedance of the mixture, they claim to have obtained a better cross-sectional average measurement with little influence of the flow regime and the pipe vertical or horizontal orientation.

3.2.4 Signal Processor

The diversity of the signal processor designs to measure the impedance of the mixture is comparable to that of the electrode systems. These methods are conveniently summarized in four general categories as

      i)   Comparator circuits

     ii)   Resonant circuits

    iii)   Bridge

    iv)   Voltage drop of a resistor in series with the fluid
         cell impedance.

In all these methods, the fluid impedance is an integral part of the signal processor. The range of the electric field frequency varies widely from a few kilohertz to a few megahertz. Apart from the elimination of electrochemical reactions, the choice of the frequency reflects the intent of the investigator to measure either the resistive or the

capacitive component of the impedance. The measurement of one or the other serves only an academic purpose which is to verify the validity of the analytical solutions. Generally, the agreement is good, but these formulae cannot be used as a means of calibration.

3.3 Design of the Impedance Void Fraction Meter

3.3.1 Electrodes

Except for the intrusive electrode systems of Garrard et al. [16] consisting of parallel wires running across the flow, most of the previous instruments have dimensions which are too large (compared to the pipe diameter) for dynamic measurements. For instance, one cannot expect a response time of the meter faster than the time needed for a transient to travel the length of the electrodes.

A prime concern in the design of our void fraction meter was to shorten the electrodes axial length. Since the minimum wavelength which can be encountered in the void fraction is of the order of a bubble diameter, a height of 6.35 mm was chosen. The non-intrusive electrode system is shown in Fig. 3.1 and consists of two 90° circular arcs made of stainless steel and flush mounted in a piece of lucite with an internal diameter identical to the 10.16 cm diameter of the test section. This configuration is not a priori the best to produce a homogeneous field in the fluid cell. However, because of the small electrode height to pipe diameter ratio, any configuration will produce some distortion of the electric field due to end effects. Moreover, even a homogeneous electric field would be significantly altered by nonuniformities in the void fraction distribution.

3.3.2 Signal Processor

In most previous signal processors (an exception being that of Cimorelli and Evangelisti [9]) one of the electrodes is grounded. Such a configuration does not, however, necessarily minimize the spreading of the electric field in the axial direction. A conducting liquid, because of its inevitable contact with metal parts in the experimental loop, can be also considered as grounded. Not having a preferential direction, the field lines issuing from the electrodes at higher potential will tend to diverge in the whole fluid creating a volume of influence larger than is necessary. The present choice of a double bridge is believed to have improved greatly the directionality of the electric field. In this approach both electrodes are active. The sinusoidal potential at one electrode lags the other by a 180° phase shift such that at any time, the electrodes assume a voltage of identical amplitude but of opposite sign. Each electrode is part of a bridge of its own. This is easily visualized by looking at a schematic representation of the processor electric diagram in Fig. 3.2. From a custom built frequency and amplitude variable oscillator, the excitation voltage is distributed to each bridge by means of inverting and non-inverting amplifiers. Following a change in the fluid cell impedance, the unbalanced voltage of each bridge is picked up by an instrument differential amplifier with a high common mode rejection ratio. The negative polarity of one of the bridges is then inverted before the signals of each bridge are added together. The output of the adder is made available on an oscilloscope screen and is needed to zero the bridge. This is done when the cell contains only the liquid phase. The signal is further processed by a demodulator circuit.

The demodulation is accomplished by multiplying the adder output with one of the bridge voltage excitation signals (carrier). This operation yields a signal double the original frequency with a D.C. offset proportional to the amplitude of both signals. Since the amplitude of the carrier signal is fixed, the D.C. voltage varies linearly with the unbalanced voltage of the double bridge. The high frequency part of the signal is filtered through a double pole Butterworth low-pass filter. After this operation, the D.C. signal is available for the evaluation of the void fraction.

A more detailed description with circuit diagrams is presented in Appendix A.

3.3.3 Frequency of Excitation

Because of the large conductivity of the water, frequencies of the order of 10 MHz would have been necessary to isolate the capacitive part of the fluid impedance. At these high frequencies, permanent dipoles of the water molecules become ineffective and the advantages of a large capacitance is lost. Moreover, since both the resistance and capacitance are temperature dependent, no real benefit is gained by doing so.

Preliminary tests showed that the electrode polarization effect was negligible above 10 KHz. From that frequency down an increasingly large capacitance was needed to null the bridge. This frequency is of the order of the one reported in Ref. [37], even though the water used in the present tests had a fair amount of chromate sodium in solution to prevent corrosion. In the 10-200 KHz range, the overall capacitance of the fluid cell including the BNC cables and other parasitic capacitances was

200 pf and the resistance 250Ω.

For the purpose of our experiments, a 50 KHz frequency was chosen. At this value, the 500 Hz Butterworth filter cut-off frequency provides a more than adequate 77 dB attenuation of the high frequency content of the multiplier output. It was also verified that the amplitude of the bridge voltage excitations had no measurable effect on the instrument performance. A $0.3V_{RMS}$ excitation was therefore arbitrarily chosen.

3.3.4 Improvements Subsequent to Preliminary Tests

The nature of the impedance within the cell at 50 KHz is almost purely resistive. However, a variable capacitor was added to the existing variable resistor intended to null the bridge. With this modification, the adder output displayed on the oscilloscope has ripples less than 5mV p. to p. for a bridge null condition. Considering the fact that the full scale available is 10 V p. to p., the null obtained is excellent.

The sensitivity of our processor to the passage of a single bubble permitted us to introduce one more improvement. It is well known that the maximum sensitivity of a bridge is obtained when the impedance to be measured is equal to the other impedances. However, for this configuration, the unbalanced voltage of the bridge becomes a nonlinear function of the impedance variation. Choosing resistances 5 times lower than the cell resistance, it was possible to linearize the bridge output. The 10 V p. to p. full scale was restored by converting the adder in a variable gain amplifier. Even with this modification, our processor could still detect the presence of a single bubble in the flow.

3.4 Steady State Calibration

3.4.1 Two-Phase Flow Test Facility

The test loop used for the calibration of the impedance void fraction meter and the experiments on the void fraction kinematic wave propagation is shown schematically in Fig. 3.3. The 2.17 m vertical test section is made of PVC piping 10.16 cm in diameter with lucite sections for visual observation of flow regimes. The air injector located at the bottom consists of an array of brass tubes 3.18 mm in diameter spanning the pipe cross section in all directions. The air is injected through holes .40 mm in diameter drilled in the brass tubes producing ellipsoid bubbles of uniform size with a mean diameter of approximately 5 mm. A custom built orifice meter previously calibrated by a displacement technique, was available for the measurement of the gas volumetric flow rate.

The maximum water speed in the test section is 2 m/s. Upstream of the air injector, a Foxboro transverse field electromagnetic flow-meter is used to monitor the water flow rate during the experiments. The bubbly mixture leaves the test section at atmospheric pressure. The air is separated from the water in the discharge tank situated at the top. The return of the water to the 600-liters reservoir is achieved by gravity.

3.4.2 Method of Calibration

The steady state calibration of the void fraction meter is based on the measurement of the mean density of the bubbly mixture. Two static pressure taps 1.3 m apart and equally spaced above and below the

electrode module situated in the middle of the test section were con-
nected to an inverted manometer through pressure lines filled with water.
From an equilibrium of the forces between the free surfaces of the
manometer, the ratio of the manometer displacement d to the distance ℓ
between the taps is equal to

$$\frac{d}{\ell} = 1 - \frac{\rho_{TP}}{\rho_W} \qquad . \qquad (3.5)$$

The mean density of the two-phase mixture is a function of the
volumetric concentration or void fraction α, according to

$$\rho_{TP} = \alpha\rho_a + (1-\alpha)\,\rho_W \qquad (3.6)$$

with ρ_a the density of the gas and ρ_W the density of water. Substitut-
ing Eq. (3.6) in (3.5) for small ratios of ρ_a/ρ_W the void fraction is
determined by

$$\alpha = \frac{d}{\ell} \qquad . \qquad (3.7)$$

Strictly speaking, this method is not suitable when large flow
rates are involved. In addition to the pressure difference due to the
change in the mixture density, the manometer reading also includes a
frictional pressure drop. Unfortunately, as shown by the experiments
of Lockhart and Martinelli [32] and many other investigators, this
frictional pressure drop is also a function of the void fraction.
Under certain flow conditions the error incurred in determining the
mixture average density becomes significant. The two effects are not
easily separable because of the poor accuracy of the empirical correla-
tions available to predict the frictional pressure drop. They can

nevertheless provide some information about its order of magnitude. An estimation of the additional frictional pressure drop due to the presence of the disperse phase for the water fluxes and void fractions considered during these calibrations, showed that this contribution was negligible. The error in the measurement of the void fraction turned out to be of the order of a few percent of the actual value.

Prior to a calibration run, the double bridge void meter was nulled and care was taken to insure that the pressure lines were free of air bubbles. For a fixed water volumetric flow rate, the gas flow rate was increased by steps. For each increment, readings of the manometer and the instrument D.C. voltage averaged over 30 seconds were taken. The procedure was carried out for different water fluxes ranging from zero to .88 m/s until a departure from the bubbly regime could be observed.

3.4.3 Calibration Results

A typical calibration curve of the output voltage as a function of the void fraction is shown in Fig. 3.4 for the case of a bubbly flow in still water. It can be seen that the response of the void fraction meter is very sensitive to the presence of bubbles giving a slope of .335 V per percentage void fraction. The linearity of the meter response indicates that the effective resistance of the mixture is proportional to the void fraction.

It is of interest to compare the measured impedance of the bubbly mixture with the value predicted by Maxwell's formula. This was accomplished by replacing the zero void fraction resistance of the fluid cell by a resistor of identical value. The resistance of the mixture

at non-zero void fraction was then simulated by increasing the resistance of the potentiometer intended for zeroing the bridge. From the resistance-voltage curve obtained, the calibration of Fig. 3.4 was used to calculate the void fraction-resistance relation. Assuming that the volume swept by the electric field between the electrodes is independent of the volumetric concentration of bubbles (which is not precisely the case as it will be shown in the next chapter) Maxwell's formula yields the following relation between the non-zero void fraction resistance R_{TP} and the zero void fraction resistance R_W

$$\frac{R_{TP} - R_W}{R_W} = \frac{3\alpha}{2(1 - \alpha)} \quad .$$

Figure 3.5 shows the comparison of our results with Maxwell's formula. Although the agreement is only fair, it nevertheless indicates that this analytical solution is very useful in predicting the order of magnitude of the disperse phase effect. Better agreement is reported by Cimorelli for the effective capacitance and by Merilo for the effective resistance even for large void fractions. It should be emphasized that the conditions prevailing in our fluid cell departed significantly from Maxwell's assumptions and the linear relation obtained in our case is as good as one could expect.

Figure 3.6 is a summary of the results obtained at non-zero water flow rate; these are presented in a form allowing a direct comparison with the calibration in still water. The manometer void fraction measurements are reported on the vertical axis, while the void fractions as determined from the meter voltage output and Fig. 3.4 are shown on the

horizontal axis. The solid line with a 45° slope corresponds to the zero water flux.

The curves of water fluxes below 31.8 cm/s compare well with the one done in still water. For higher water fluxes, the comparison is poorer. In all our experiments, as will become evident in the next chapters, the 31.8 cm/s flux seems to indicate a transition point for the void fraction distribution. This particular behavior will be further discussed in Chapter 5.

From these calibration curves, it is clear that the void fraction meter depends on the void fraction distribution which, in turn, is affected by the water velocity. However, it is of interest to point out that all the points lying above the 45° line (shown by solid points in Fig. 3.6) were visually observed to be in a churn turbulent rather than in a bubbly flow regime.

3.5 Discussion

In steady state two-phase flow, the impedance void fraction meter offers a low cost alternative to the beam attenuation techniques. Although it is shown that this type of instrument is somewhat sensitive to the void distribution, it should be recalled that to some extent all techniques are troubled by such sensitivity. The all-purpose void fraction meter has yet to be found.

We have not explored at this point the dynamic capability of our instrument, and from the steady-state results it is not possible to assess the effect of the short axial length of the electrodes. The dynamic calibration presented in the next chapter will demonstrate the advantages of the present design.

① Lucite
② Stainless Steel Electrodes
③ O'Rings
④ BNC Connector
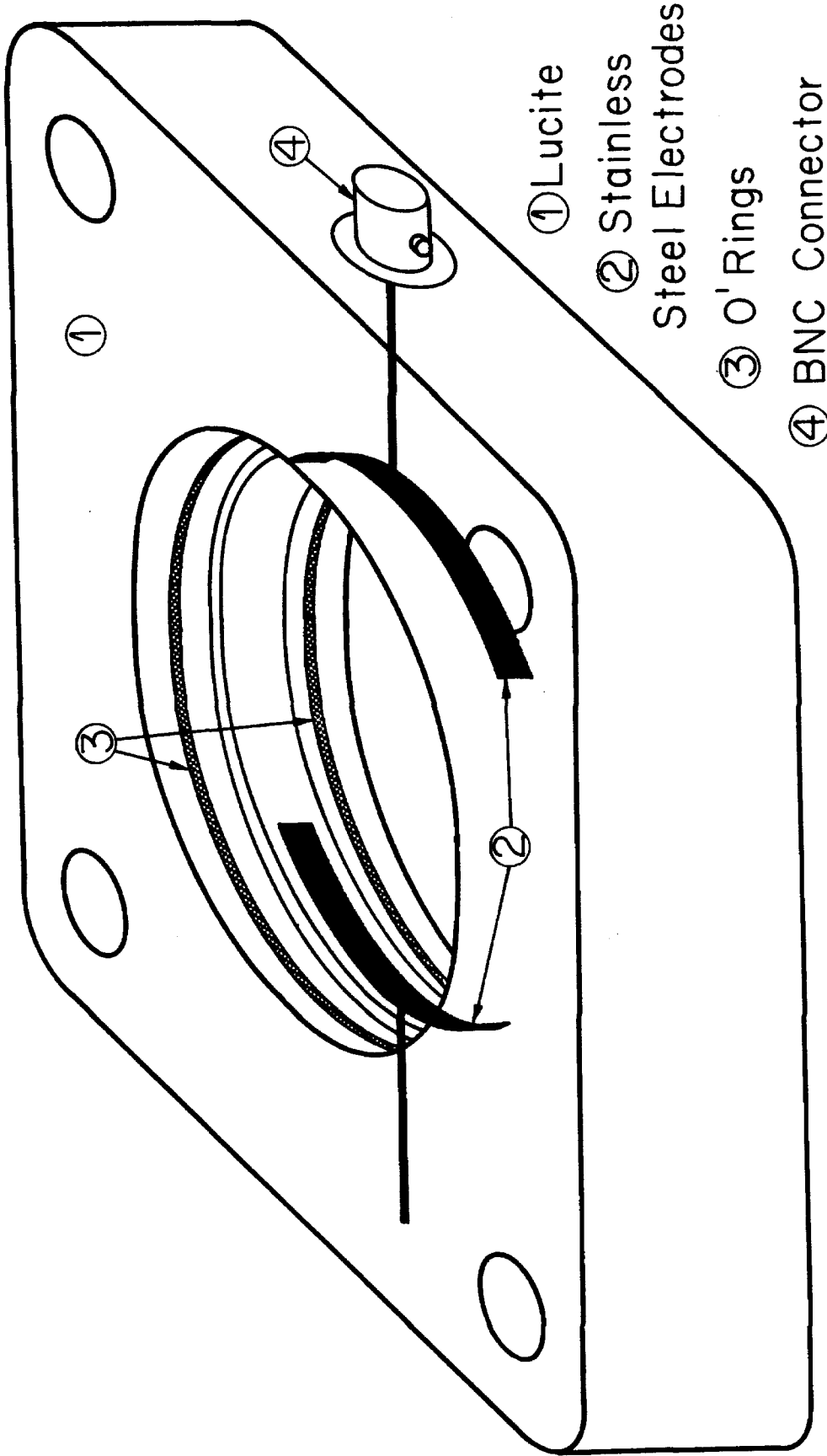
Figure 3.1   Isometric view of the electrode system showing the stainless steel circular arc electrodes mounted in a piece of lucite.

-44-
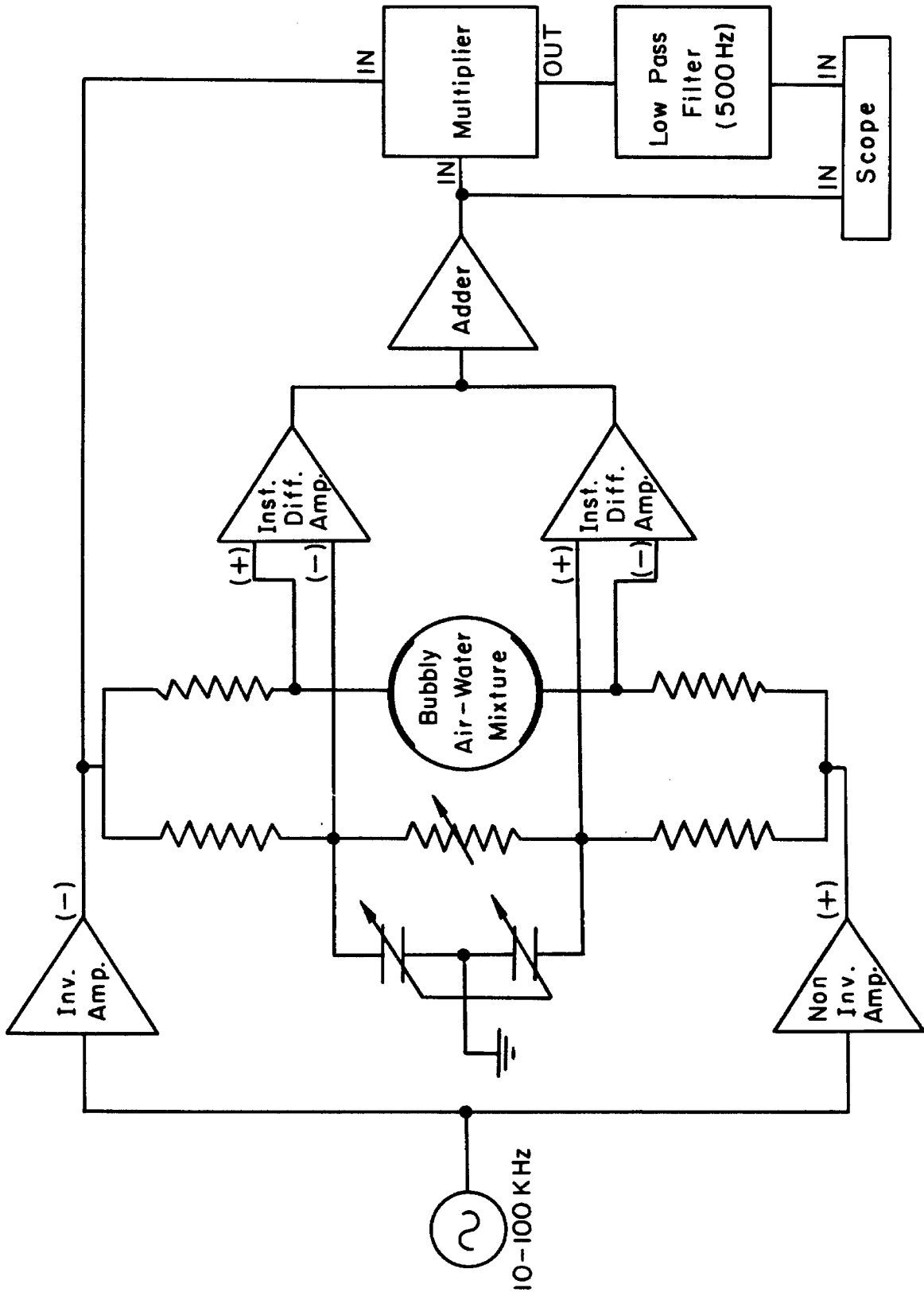
Figure 3.2 Schematic diagram of the impedance void fraction meter signal processor.

1. Water Reservoir
2. Pump
3. Water Flow Rate Adjustment
4. Electromagnetic Flow Meter
5. Pressure Regulator
6. Air Orifice Meter
7. Air Flow Rate Adjustment
8. Quick Closing Valve
9. Air Injector
10. Test Section
11. Discharge Reservoir
12. Inverted Manometer
13. Impedance Void Fraction Meter

Figure 3.3 Air-water experimental loop.
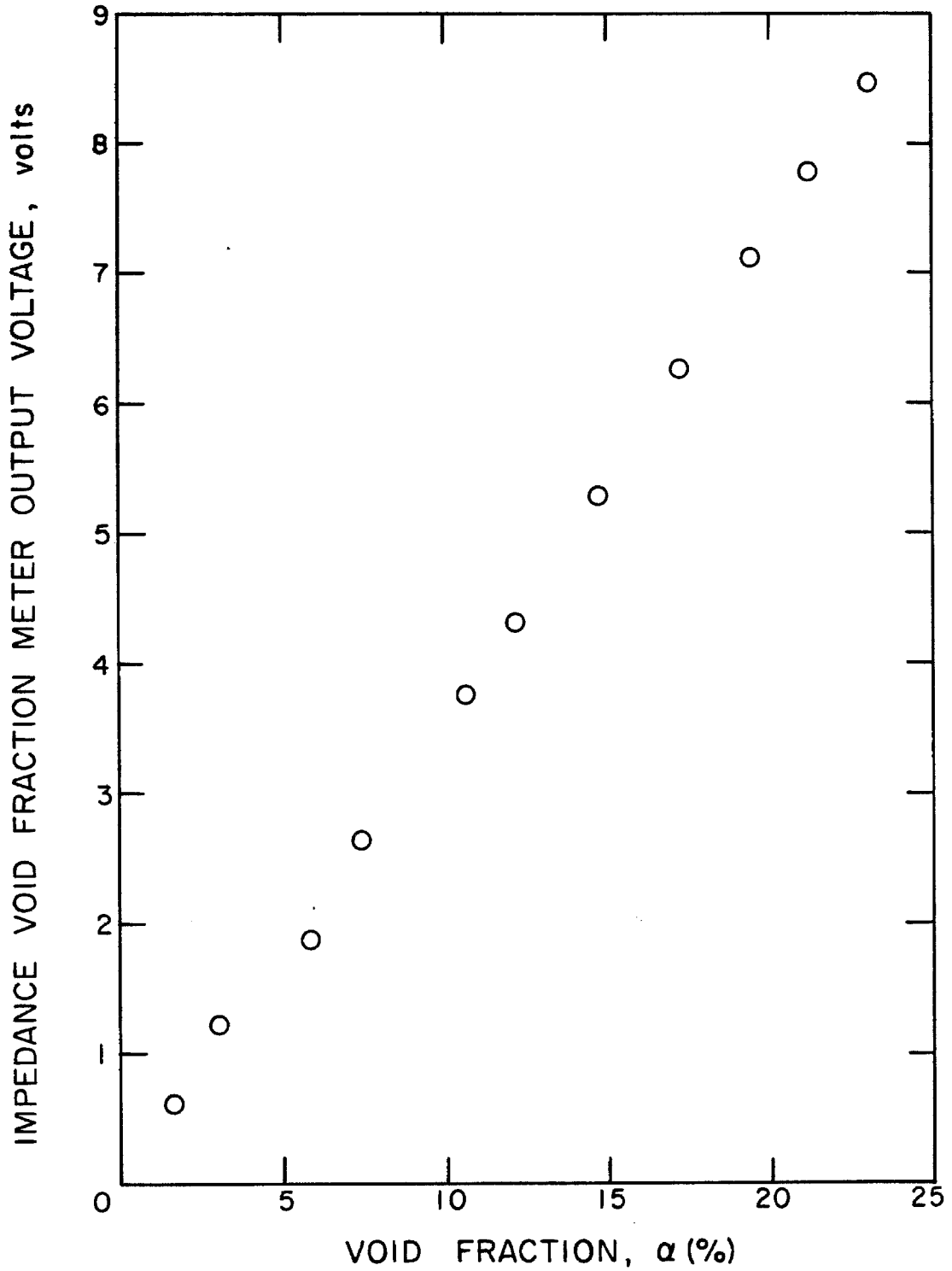
Figure 3.4   Calibration curve of the impedance void fraction meter for a steady air-water bubbly flow regime in stagnant water.
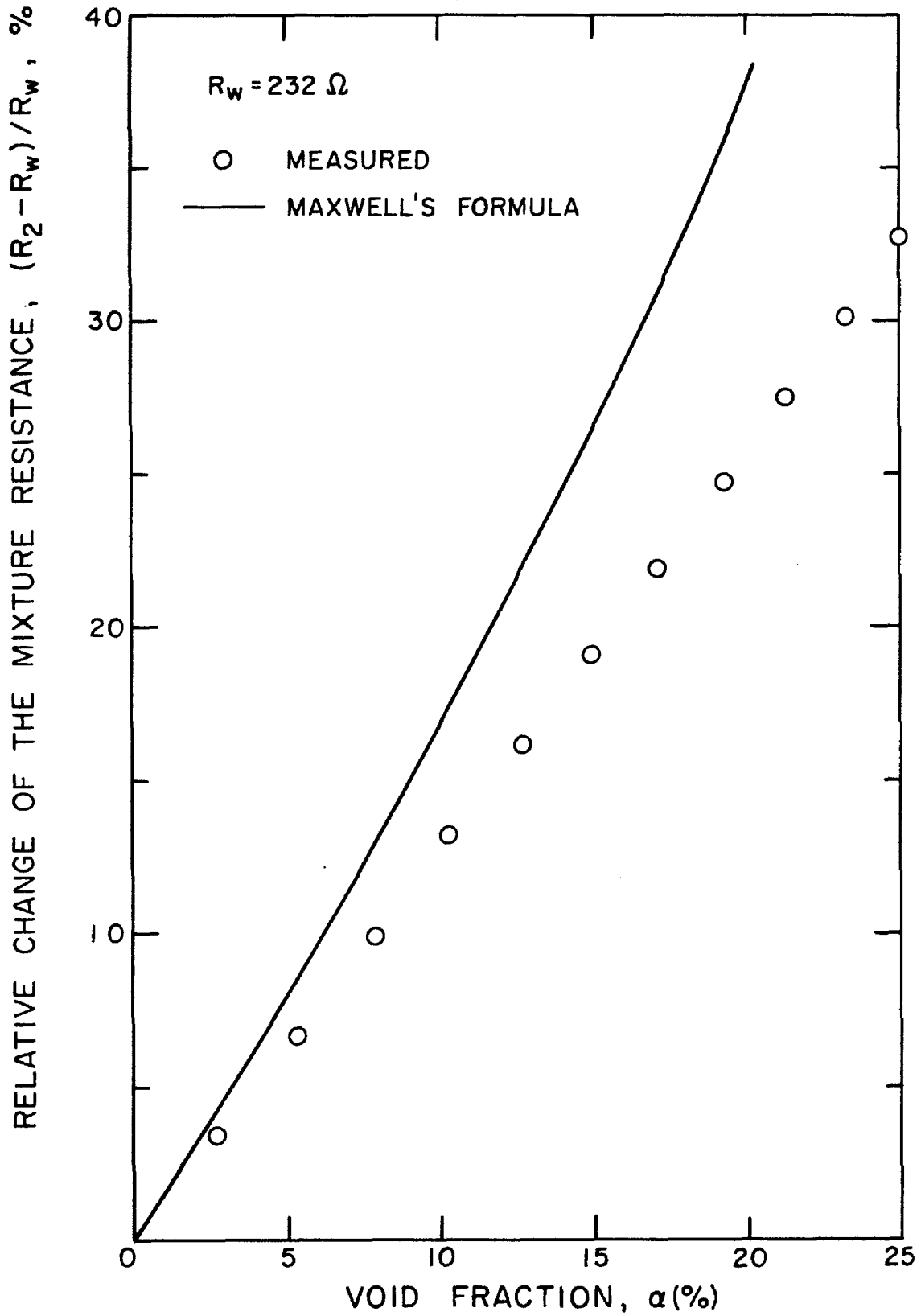
Figure 3.5   Relative change of the resistance measured in an air-water bubbly flow regime. Maxwell's formula is shown as a solid line.
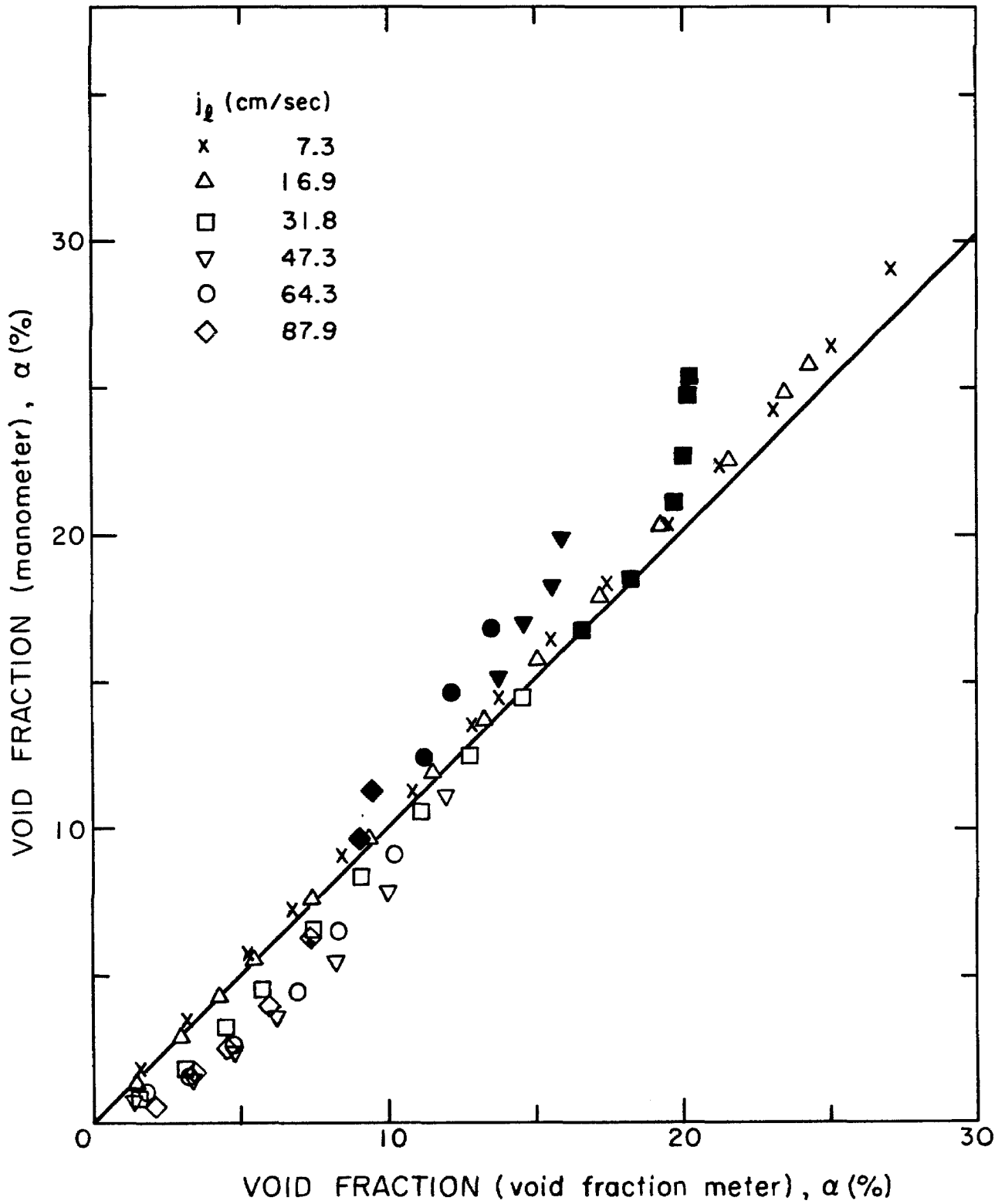
Figure 3.6   Steady state calibration of the void fraction meter for non-
zero water volumetric fluxes; readings from the manometer are
on the vertical axis, readings of the meter using the zero
flux calibration are on the horizontal axis.   The solid line
indicates the zero flux calibration.

IV. DYNAMIC CALIBRATION OF THE IMPEDANCE VOID FRACTION METER

4.1 Introduction

Like most physical processes, the measurement of the steady state void fraction exhibits small fluctuations about a mean value as illustrated by the impedance meter recordings of Fig. 4.1. We shall demonstrate that the statistical analysis of this "noise" can yield valuable information on the dynamic response of the meter and on some physical properties of the disperse phase.

The possibilities of statistical analysis for the two-phase flow system have not yet been fully explored for this type of instrument. Apparently the only noise study reported in the literature is that of Garrard and Ledwidge [16]. Their identification of the stochastic nature of the disperse phase as a general Markov process led them to vague conclusions.

4.2 Experiment

4.2.1 Procedure

The experimental set-up for noise analysis was similar to that for the steady state calibration of the void fraction meter. The demodulated output signal from the void fraction meter was recorded for a wide range of nominally steady flows. For a given water volumetric flow rate, a 60 second real time recording was performed for each increment in the void fraction until a transition between the bubbly and churn turbulent regimes could be observed through the lucite section. The experiment was repeated for different water volumetric fluxes.

The statistical analysis of the recorded signal and the determination of its frequency content was performed on a Spectral Dynamics Company Digital Signal Processor, Model 360. The built-in high pass filter of the DSP was used to strip out the D.C. component before the signal was averaged over a 40 second period for statistical analysis.

4.2.2 Noise RMS Value

Under the assumption of ergodicity, the RMS value of the noise was calculated from the autocorrelation function evaluated at time zero on the DSP. The results are presented in Fig. 4.2, where the signal-to-noise ratio is plotted against the mean or D.C. output voltage of the void fraction meter.

For low water flow rates, it was not possible to observe a flow regime transition prior to saturation of the signal conditioning amplifiers. The slowly increasing signal-to-noise ratio seen in this figure for large D.C. output level is believed to be a trend artificially created by this saturation effect. However, the data for larger volumetric water fluxes exhibit a real and interesting behavior at high void fractions. The sharp deterioration of the signal-to-noise ratio is due to the transition of the bubbly regime into a regime having large unstable structures. Although the D.C. voltage only changed marginally with an increase of the gas flow rate, larger fluctuating voltages were noticed for this flow regime. In fact, the change in flow regime was detected sooner by the void fraction meter than by visual observation; those points at which the churn turbulent flow was observed are indicated by solid points.

As in the case of the steady state calibration curves, water fluxes larger than 31.8 cm/s depart significantly from the zero water flux SNR curve. For these fluxes a substantial increase in the RMS noise was noticed, contributing to the downward shift of the corresponding curves.

4.2.3 Probability Density Distribution

In a bubbly flow, it is clear that the output voltage of the void fraction meter is the result of a collection of discrete events related to the passage of bubbles through the volume of influence of the electrodes. The one-half power slope observed in Fig. 4.2 is typical of physical processes involving a discrete random variable. Such processes are characterized by the proportionality existing between the variance and the expected value of the random variable.

The statistical process of the random variable associated with the void fraction measurement must now be investigated. The probability distributions shown in Fig. 4.3 offer some guidance in this respect. These distributions obtained by signal processing through the DSP correspond to four different void fractions for the case of zero water flow rate and are typical of distributions for other water flow rates. The positive skewness observed in the first figure suggests a Poisson distribution. As the void fraction increases, the Poisson distribution shifts towards a Gaussian distribution according to the law of large numbers. For the purpose of comparison, a Gaussian distribution with a standard deviation measured from the autocorrelogram is superimposed on the experimental distributions. The agreement for large void fraction is excellent, as expected.

Similar probability distributions were observed by Garrard and Ledwidge using their void fraction meter. However, to retrieve practical information from the statistical analysis of such data, we need to digress from the path they followed and propose a particular statistical process. The task involved a certain degree of uncertainty which can be removed in part by comparison of the actual statistics of the measured variable with those of the proposed model.

4.3 Stochastic Process for a Bubbly Mixture

4.3.1 Poisson Impulse Process

We shall choose to examine a model based on the Poisson impulse process. The motivation behind this choice can be drawn from the analogy existing between the current fluctuations in a conductor due to the discrete nature of the electric charge, and the gas flow rate in a pipe propagating in the form of bubbles. The analogy would hold quite closely for a uniform distribution of the disperse phase throughout the cross section of the pipe and for bubbles of the same size. Furthermore, it will be assumed that the electric field between the electrodes of the void fraction meter is uniform, such that each bubble over the cross section of the pipe contributes equally to the output voltage. Each assumption is not formally met in a real situation. Nevertheless, the straight line steady state calibration curve of our meter for low water volumetric fluxes suggests that they are satisfied in an average sense.

The Poisson impulse process is a well known stochastic process, and only the results need be quoted for the purpose of this analysis.

More details on the process can be found in Ref. [39]. The process is defined as the time derivative of a random variable $y(t)$ for which the probability of being equal to n events in the time interval $[o,t]$ is given by the Poisson distribution

$$P\{y(t)=n\} = e^{-\mu t}\frac{(\mu t)^n}{n!} \quad . \tag{4.1}$$

Because $y(t)$ is a staircase function, its derivative leads to a sequence of impulses randomly distributed in time described by the process $x(t)$:

$$x(t) = \sum_e \delta(t-t_e) \tag{4.2}$$

where δ is the delta function and t_e are the points in time at which the events occur. It can be shown that for this process, the expected value is

$$E\{x(t)\} = \mu \quad , \tag{4.3}$$

while the auto-correlation has the form

$$R_{xx}(\tau) = \mu^2 + \mu\delta(\tau) \quad . \tag{4.4}$$

Defining the power spectrum as

$$S_{xx}(\omega) = \int_{-\infty}^{+\infty} R_{xx}(\tau)e^{-i\omega\tau}d\tau \quad , \tag{4.5}$$

the Poisson impulse process power spectrum is readily evaluated as

$$S_{xx}(\omega) = 2\pi\mu^2\delta(\omega) + \mu \quad . \tag{4.6}$$

A more interesting quantity to consider is the fluctuating part of $x(t)$ denoted by $\tilde{x}(t)$. The expected value of $\tilde{x}(t)$ is therefore simply

$$E\{x(t) - \mu\} = E\{\tilde{x}(t)\} \equiv 0 \tag{4.7}$$

and the autocorrelation and power spectrum for the fluctuating part are, respectively

and

$$R_{\tilde{x}\tilde{x}}(\tau) = \mu \delta(\tau) \tag{4.8}$$

$$S_{\tilde{x}\tilde{x}}(\omega) = \mu \quad \bullet \tag{4.9}$$

The Poisson impulse process is not a realistic one for a physical system, since the mean square value of the noise given by the integral over the axis of the frequency of the power spectrum yields an infinite value. The problem is easily taken care of by the introduction of a low pass filtering function which is most likely to be encountered in a physical system. The filtered Poisson impulse process is known as the "Shot-Noise" process.

4.3.2 Poisson Impulse Process for a Uniform Two-Component Bubbly Mixture

The gas phase is considered incompressible without heat and mass transfer. In terms of a Poisson impulse process, the gas flow rate Q_g of the disperse phase can be expressed as

$$Q_g(t) = \tau_b \sum_e \delta(t - t_e) \tag{4.10}$$

where τ_b by extension is some representative averaged volume of the bubbles. The expected value or mean gas flow rate is related to the bubble volume by

$$E\{Q_g(t)\} \equiv \overline{Q}_g = \eta \tau_b \tag{4.11}$$

where η is understood as being the Poisson distribution parameter.
From a practical point of view, η represents the mean value of the number of bubbles per unit time passing through a cross section of the pipe.

However, the output signal of the void fraction meter yields a measure of the bubble volumetric concentration or void fraction. The relation between the average gas volumetric flow rate and the average void fraction $\bar{\alpha}$ is provided by the steady state equation of continuity which gives

$$\bar{Q}_g = A\bar{\alpha}\bar{v} \tag{4.12}$$

where A is the cross section of the pipe and $\bar{v}$ is the average velocity of the disperse phase. Equation (4.12), together with Eq. (4.11), is used to rewrite the stationary process given by (4.10) in terms of the void fraction, leading to

$$\alpha(t) = \frac{\tau_b}{A\bar{v}} \sum_e \delta(t - t_e) \tag{4.13}$$

with an expected value $\bar{\alpha}$,

$$\bar{\alpha} = \frac{\eta\tau_b}{A\bar{v}} \tag{4.14}$$

an autocorrelation

$$R_{\alpha\alpha}(\tau) = [\frac{\tau_b}{A v}]^2 [\eta^2 + \eta\,\delta(\tau)] \tag{4.15}$$

and a power spectrum

$$S_{\alpha\alpha}(\omega) = [\frac{\tau_b}{A v}]^2 [2\pi\eta^2\,\delta(\omega) + \eta] \quad . \tag{4.16}$$

4.3.3 Shot-Noise Process for a Bubbly Mixture

The existence of the filter function needed for the shot-noise process is evident in a typical Fourier spectrum as shown in Fig. 4.4. As the frequency increases, not only does the amplitude of the fluctuating voltage tapers off, but it also displays the decaying feature of a first order filter.

The dynamic response of the transducer electronics is fixed by the two-pole low pass Butterworth filter having a 3 dB frequency cut-off at 500 Hz. The filtering effect observed in the frequency spectrum occurs approximately at two orders of magnitude lower in frequency, and is therefore not inherent to the meter signal processor. The physical cause of this can readily be explained. The finite thickness of the electric field between the electrodes and its diffusion in the axial direction creates a volume of influence. The diffusion of the field, although minimized by the use of a double bridge, is responsible for the gradual rise and fall of the voltage as the bubble enters and leaves this volume of influence. The peak value is obtained when the bubble is aligned with the center of the electrodes. Although we do not know explicitly this filter function, we can nevertheless suggest that it will be of the approximate form

$$h(t) = \begin{cases} k\ e^{\kappa t} & t \leq 0 \\ k\ e^{-\kappa t} & t \geq 0 \end{cases} \tag{4.17}$$

which satisfies the requirement of a first order filter sensitive to an incoming event. The values of k and κ will now be determined in terms of the statistical properties of the shot-noise process.

4.3.4 Mean and Autocorrelation of the Shot-Noise Process

The convolution integral of the stationary process $\alpha(t)$ with the filter function $h(t)$ provides the necessary relation for the output voltage $V(t)$ of the void fraction meter:

$$V(t) = \int_{-\infty}^{+\infty} \alpha(t) \, h(t - \tau) \, d\tau \quad \bullet \tag{4.18}$$

After substitution of the $\alpha(t)$ from Eq. (4.13), this yields

$$V(t) = \frac{\tau_b}{A\bar{v}} \sum_e h(t - t_e) \quad \bullet \tag{4.19}$$

The value of k can be readily evaluated by taking the mean value of Eq. (4.18) and expressing both $V(t)$ and $\alpha(t)$ in terms of their mean and fluctuating parts:

$$E[\bar{V} + \tilde{V}(t)] = \int_{-\infty}^{+\infty} E[\bar{\alpha} + \tilde{\alpha}(t)] \, h(t - \tau) \, d\tau \tag{4.20}$$

where E is the mean value operator. The fluctuating parts having a zero mean, we finally get:

$$\bar{V} = \int_{\infty}^{\infty} \bar{\alpha} \, h(t-\tau) \, d\tau \quad \bullet \tag{4.21}$$

If m denotes the slope of the steady state calibration of the void fraction meter, the value of k is obtained by solving the integral and substituting $m\bar{\alpha}$ for $\bar{V}$, which yields

$$k = \frac{m}{2} \kappa \quad \bullet \tag{4.22}$$

The knowledge of the filter function permits the evaluation of the explicit form of the autocorrelation function of the process $\tilde{V}(t)$ given by

$$R_{\tilde{V}\tilde{V}}(\tau) = \frac{1}{2\pi} \int_{-\infty}^{+\infty} |H(i\omega)|^2 \, S_{\tilde{\alpha}\tilde{\alpha}} \, e^{i\omega\tau} \, d\omega \qquad (4.23)$$

where $H(i\omega)$, the Fourier transform of the filter function $h(t)$, assumes the value

$$H(i\omega) = \frac{m\kappa^2}{[\kappa^2 + \omega^2]} \qquad (4.24)$$

and $S_{\tilde{\alpha}\tilde{\alpha}}(\omega)$, the power spectrum of the fluctuating part $\tilde{\alpha}(t)$ of the Poisson impulse process $\alpha(t)$ is

$$S_{\tilde{\alpha}\tilde{\alpha}}(\omega) = n\left[\frac{\tau_b}{A\bar{v}}\right]^2 \qquad . \qquad (4.25)$$

Substitution of (4.24) and (4.25) in Eq. (4.23) leads to the following closed form solution of the autocorrelation function:

$$R_{\tilde{V}\tilde{V}}(\tau) = m^2 \, \frac{\kappa}{4} \, n\left[\frac{\tau_b}{A\bar{v}}\right]^2 \, e^{-\kappa|\tau|} \, [1 + \kappa|\tau|] \qquad . \qquad (4.26)$$

This last expression obtained for the autocorrelation of the output voltage fluctuation provides a powerful tool with which to characterize the dynamic behavior of the void fraction meter. Noting that at time $\tau = 0$ the autocorrelation assumes the value

$$R_{\tilde{V}\tilde{V}}(0) = m^2 \, \frac{\kappa}{4} \, n\left[\frac{\tau_b}{A\bar{v}}\right]^2 \qquad , \qquad (4.27)$$

one can rewrite $R_{\tilde{V}\tilde{V}}(\tau)$ in a form more suitable for experimental measurements as

$$R_{\tilde{V}\tilde{V}}(\tau) = R_{\tilde{V}\tilde{V}}(0) \, e^{-\kappa|\tau|}(1+\kappa|\tau|) \quad . \tag{4.28}$$

The mean square value of the noise $R_{\tilde{V}\tilde{V}}(0)$ depends on physical quantities related to the disperse phase, namely the number of events per unit time, the bubble volume and its velocity. It is also a function of the filter constant κ , the inverse of which has the dimension of time. Equation (4.28) provides us with a means to evaluate κ directly from the autocorrelograms of the actual signal without prior knowledge of the physical properties of the disperse phase. The determination of κ from a correlogram can be performed either by a one-point fit or by integration over a time interval $[0,\infty]$. In practice, the unbounded domain of integration does not pose a serious problem for an experimental autocorrelation function because of the exponential decay of the integrand.

Then, with the known value of κ, the mean square value of the noise $R_{\tilde{V}\tilde{V}}(0)$ yields information about the disperse phase properties. Substituting for $\eta = \bar{\alpha}\,\dfrac{A\bar{v}}{\tau_b}$, $R_{\tilde{V}\tilde{V}}(0)$ becomes

$$R_{\tilde{V}\tilde{V}}(0) = m^2\,\frac{\kappa}{4}\,\bar{\alpha}\,\frac{\tau_b}{A\bar{v}} \quad . \tag{4.29}$$

Since κ, the filter constant, m, the steady state calibration slope, $\bar{\alpha}$ the mean void fraction, A the pipe cross-section, and $R_{\tilde{V}\tilde{V}}(0)$ are known quantities, this yields a relation between the value of the individual bubble volume τ_b and its average velocity. For a known volumetric

flow rate of the gas, the bubble volume can therefore be evaluated.

4.4 Experimental Evidence of the Shot-Noise Process

Some degree of confidence in the shot-noise model and the filter function can be achieved by comparison of the autocorrelograms obtained experimentally with the autocorrelation function of the statistical model.

The recorded output voltage of the impedance void fraction meter for a steady bubbly mixture was processed through the Digital Signal Processor for the computation of the autocorrelograms. For a given void fraction and water volumetric flow rate, the autocorrelation function calculated by the DSP was the result of an average performed over a set of 32 ensembles, each with a time duration of 2.5 seconds. A typical set of autocorrelograms is shown in Fig. 4.5 for different void fractions. Although the water volumetric flux is zero in this case, these are representative of autocorrelograms found for other values of the water flow rate. It can be observed that they display an exponential-like decay near the origin of the time axis. Following this decay, the autocorrelograms converge to zero as time increases with increasing small and random oscillations about the axis. Only the first under-shooting of the axis is visible in this figure. This oscillating behavior is a consequence of the indented profile of the frequency spectrum previously shown in Fig. 4.4. The smoothness of the decay is compatible with the statistical model.

To compare the autocorrelogram with the predicted autocorrelation function, the one-point fit is more easily done than the integration

method to determine κ . The substitution of κ into the theoretical expression gives a curve that should match the autocorrelogram, provided that the general form of the filter function proposed is adequate and that the shot-noise process is pertinent. Because the autocorrelogram is an experimental measurement, some uncertainties are associated with its true shape. Instead of attempting a one-point fit, we elected to calculate many values of κ and work out a weighted average $\bar{\kappa}$.

This was done for void fractions in the linear portion of the curves of Fig. 4.2. Within this region, the signal output of the void fraction meter is truly associated to an uncorrelated discrete process and as such satisfies a necessary condition for the existence of a shot-noise process. Also, water volumetric fluxes higher than 31.8 cm/s were not considered because of their pronounced departure from the straight line steady state calibrations obtained for lower water fluxes.

To gain confidence in the validity of our choice of the filter function, an autocorrelation function was also calculated for the typical RC low pass filter, which is

$$h^*(t) = \begin{cases} 0 & , \ t \le 0 \\ k^* e^{-\kappa^* t} & , \ t \ge 0 \end{cases} \tag{4.30}$$

giving

$$R^*_{\tilde{V}\tilde{V}}(\tau) = R^*_{\tilde{V}\tilde{V}}(0) \ e^{-\kappa^* \tau} \tag{4.31}$$

where $R^*_{\tilde{V}\tilde{V}}(0)$ takes the value

$$R^*_{\tilde{V}\tilde{V}}(0) = m \ \frac{\kappa^*}{2} \ n[\frac{\tau_b}{Av}]^2 \ . \tag{4.32}$$

Following an identical procedure, the weighted average value $\overline{\kappa}^*$ was found from the autocorrelograms.

A selection of autocorrelograms is presented in Fig. 4.6 to 4.9. Also shown, are points calculated from the value of $\overline{\kappa}$ and $\overline{\kappa}^*$. It can be seen from these figures that the primary choice of the filter function is superior and matches closely the measured autocorrelograms. Similar conclusions can be drawn from the majority of the autocorrelograms considered.

4.5 Determination of the Physical Properties of the Disperse Phase

The shot-noise model and the filter function proposed seeming to be acceptable, it is possible to go one step further. Since $\overline{\kappa}$ is known and the gas velocity $\overline{v}$ could be determined by a technique described in Chapter V, the average bubble diameter for a given steady-state bubbly regime is simply

$$D = [\frac{24}{\pi} \frac{R_{\widetilde{vv}}(0)}{\overline{v}^2} \cdot \frac{\overline{\alpha} \ A\overline{v}}{\overline{\kappa}}]^{1/3} .$$

(4.33)

The calculated bubble diameters are given in Table 4.1 along with the measured quantities entering in formula (4.33). The results are very consistent, although the values obtained for a 31.8 cm/s water flow rate are consistently 1 mm higher. They are in close agreement with 5 mm bubble mean diameter observed.

4.6 Dynamic Response of the Impedance Void Fraction Meter

The greatest advantage of our model is the determination of the filter function which dominates the dynamic response of the void fraction

meter. The filter time constant is evaluated directly from the auto-correlograms by taking the inverse of $\bar{\kappa}$.

As probably noted already from Table 4.1, $\bar{\kappa}$ is a strong function of the velocity of the disperse phase. It will be shown in the next chapter that this velocity is also a function of the void fraction. To account for both variables, the values of $\bar{\kappa}$ are first plotted as a function of the void fraction and fitted with a straight line as illustrated in Fig. 4.10. Then, using the data of Chapter V on the relative velocity of the disperse phase and the known water volumetric flux, a cross plot of $\bar{\kappa}$ versus the gas absolute velocity was obtained for constant void fraction. These results are shown in Fig. 4.11.

According to our previous discussion on the filtering process due to the electric field volume of influence, the dependence of $\bar{\kappa}$ on the velocity of the disperse phase is not surprising. The slower the bubble, the longer is its residence time in the volume, resulting in a longer rise time of the signal output. This is strongly emphasized by the trend of $\bar{\kappa}$ as the velocity decreases. The extrapolated value of $\bar{\kappa}$ at the origin is zero, meaning an infinite rise time of the meter signal.

It is immediately realized from these data that the dynamic response of the void meter is not best characterized by its time rise, or equivalently by its cut-off frequency. A more meaningful characterization is done in terms of the void fraction wavelength for which the voltage output is attenuated by a 3 dB factor. This wavelength is closely related to the axial penetration of the electric field. The Fourier transform of the filter function being given by Eq. (4.24), the 3 dB wavelength is calculated as

$$\lambda_{3\,dB} = \frac{2\pi\bar{V}}{\kappa(\sqrt{2}-1)^{1/2}}$$ (4.34)

which yields the results shown in Fig.4.9. This figure gives a better overall picture of the dynamic capability of the void fraction meter. For a wide range of void fractions and velocities, all 3 dB wavelengths are comprised between 4.5 and 7.0 cm.

4.7 Particularity of the Filter Function of the Electrode System

In steady oscillatory two-phase flows, the phase shift between the measured quantities is important. To obtain the actual phase shift, the transfer function of the instruments must be known. As a direct consequence of the symmetry of the filter function h(t), the transfer function $H(i\omega;\kappa)$ of Eq.(4.24) has no component in quadrature. The output voltage of the void fraction meter is therefore in phase with the oscillating void fraction for all frequencies.

4.8 Considerations on the Impedance Void Fraction Design

The width of the electrodes was chosen to be of the order of a bubble diameter. The fact that measurable wavelengths are larger by an order of 10, points out a fundamental problem plaguing this type of void fraction meter. This problem is related to the axial penetration of the electric field.

A reduction of this penetration can be achieved by decreasing the distance separating the electrodes. In doing so, however, intrusion into the two-phase flow is unavoidable, and a too large number of electrodes may affect the flow itself. On the other hand, intrusive electrodes are likely to give a better average cross-sectional reading

of the void fraction and be less sensitive to void fraction profiles.
A compromise on the number of electrodes intruding into the flow is
therefore necessary. A smaller distance between the electrodes also
permits the use of wire type electrodes as done by Garrard and Ledwidge
[16] which further reduces the overall axial influence of the electric
field.

Another suitable requirement concerns the electronics of the void
fraction meter if a dynamic calibration by noise analysis is sought.
This requirement consists in having a much higher low-pass filter
cut-off frequency than that of the filter associated with the electrodes
volume of influence. When this requirement is satisfied, the two filters
are practically uncoupled which greatly simplifies the expression of the
shot noise autocorrelation function. Hence, the estimation of the
electrodes cut-off frequency should be used to fix the minimum electronic
filter cut-off frequency, which in turn determines the frequency at which
the bridge must be excited. As mentioned in the previous chapter, a broad
range of excitation frequencies is available.

4.9 Conclusion

The statistical properties of the shot-noise process compare well
with those of the fluctuating output voltage of the void fraction meter.
This enabled us to gain confidence about the proposed general form of
the filter associated with the volume of influence of the electric
field. The steady state calibration, along with the measured auto-
correlograms were sufficient to determine explicitly this filter func-
tion whose time constant is $1/\bar{\kappa}$. Moreover, because the autocorrelation
at time zero contains information about the physical properties of the

disperse phase, it was possible to determine an average bubble diameter which agrees well with our observations.

The dynamic response of the void fraction meter is entirely dominated by the axial penetration of the electric field. the void fraction wavelength for which the output voltage is attenuated by a 3 dB factor is therefore a more meaningful characterization of this type of instrument than the usual filter cut-off frequency.

In light of this study, it becomes clear that a reduction of the axial penetration of the electric field is necessary to increase the dynamic response of this type of instrument.
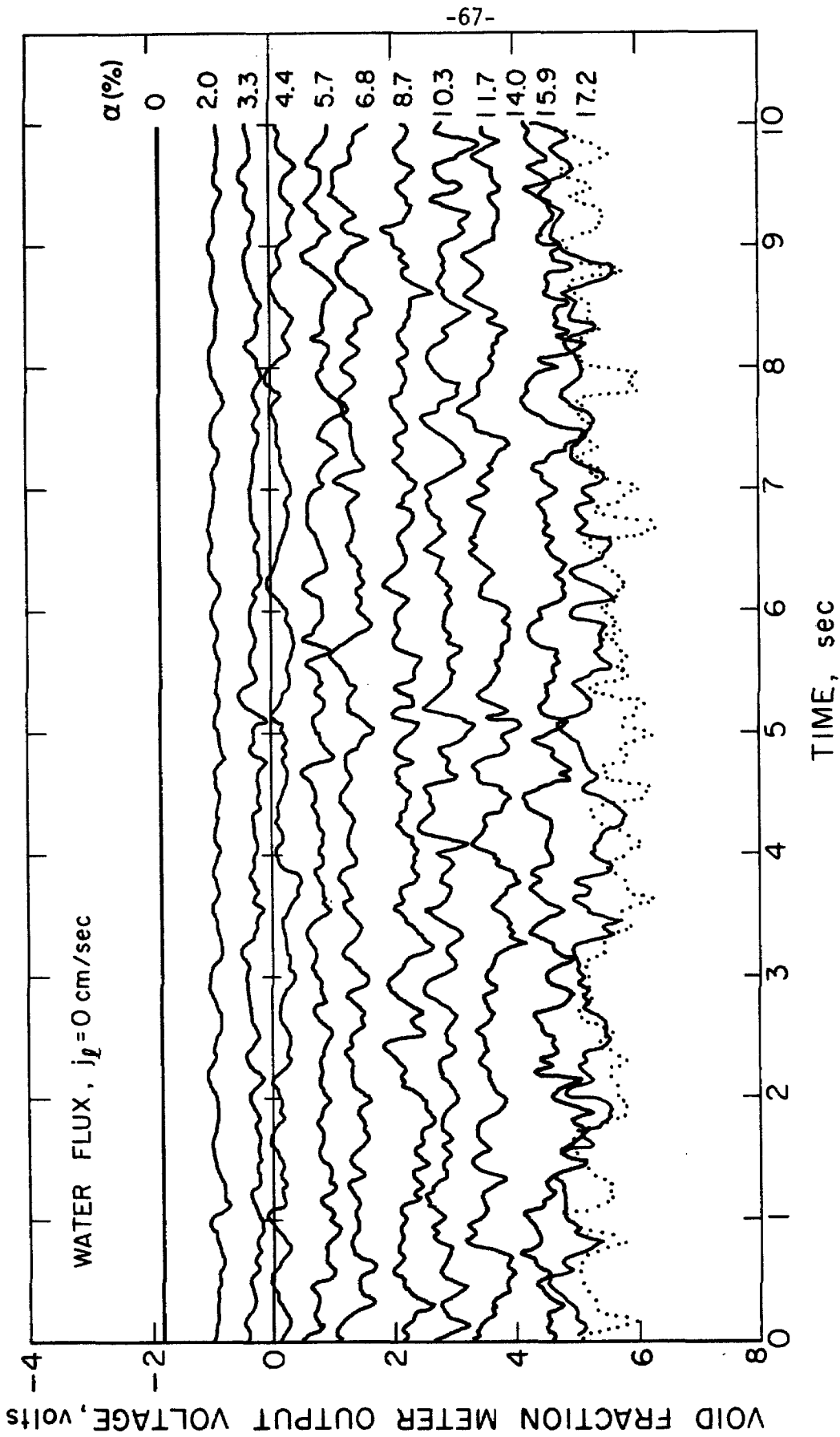
Figure 4.1 Typical outputs of the impedance void fraction meter in a steady air-water bubbly flow regime showing qualitatively the relative magnitude of the voltage mean and fluctuating parts.
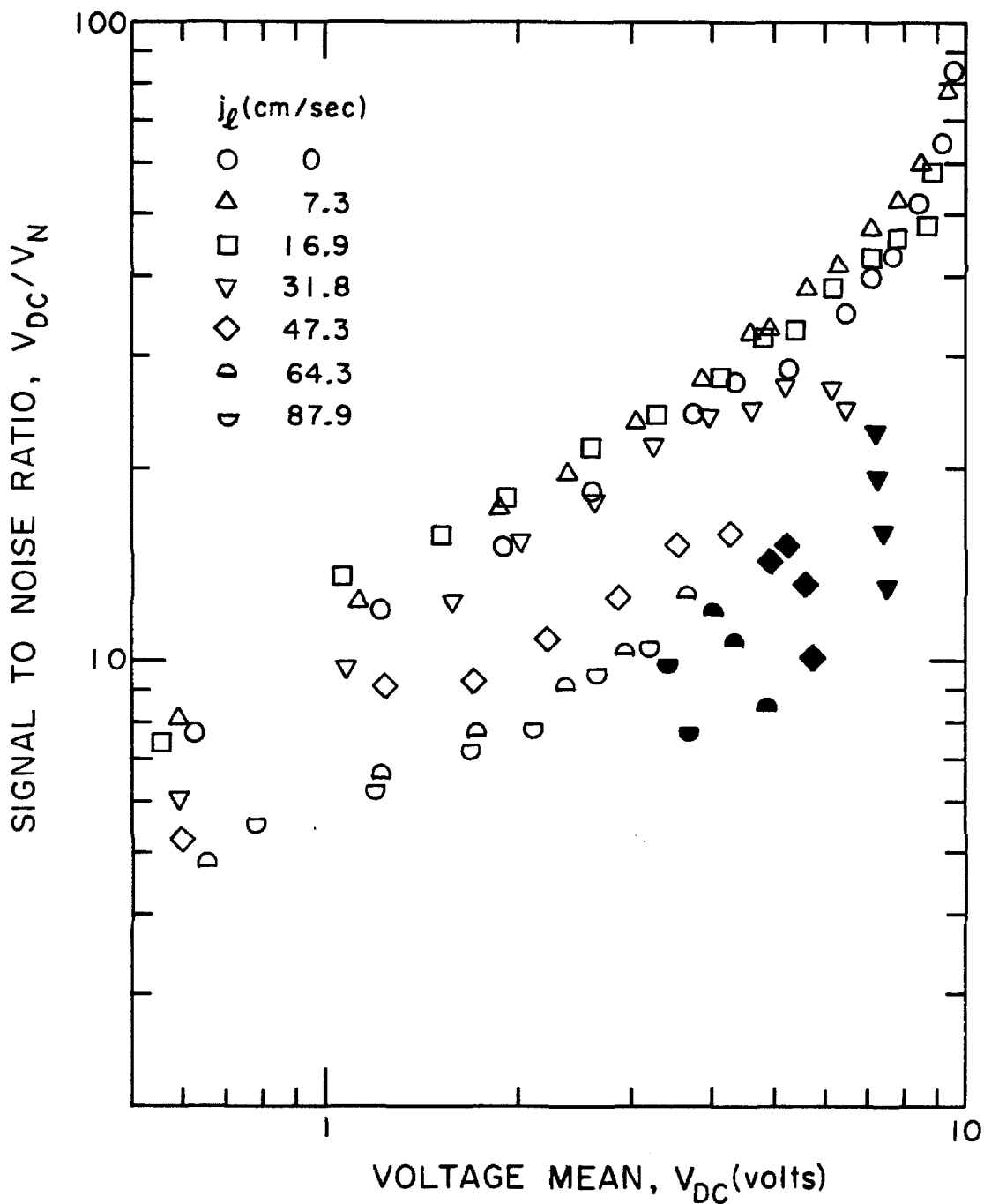
Figure 4.2   Signal-to-noise ratio of the void fraction meter in a steady air-water mixture. Solid data points indicate that a transition from bubbly to churn turbulent flow regime was observed. V_{DC} is the voltage mean value; V_N is the RMS value of the fluctuating voltage.
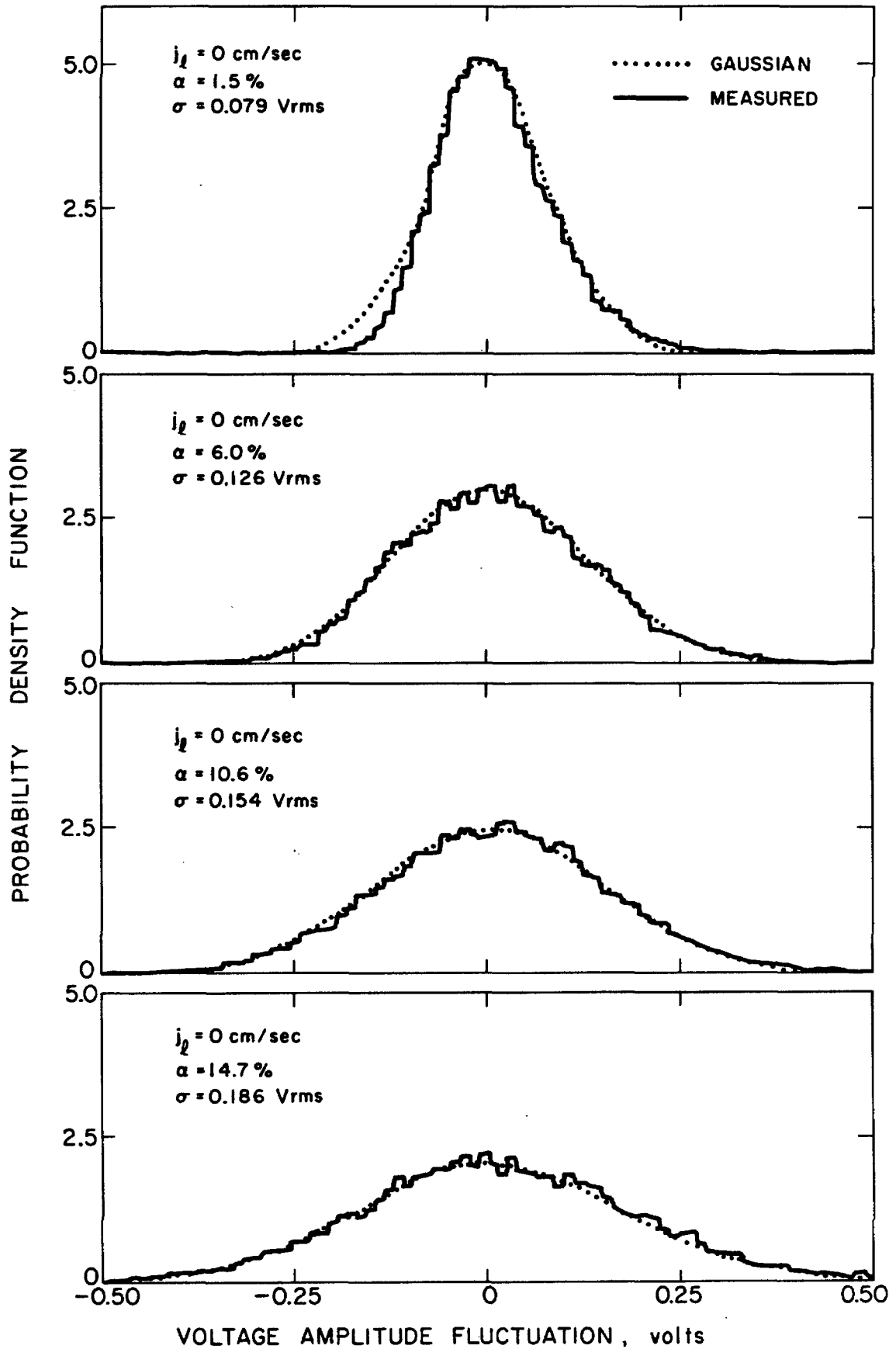
Figure 4.3   Probability density distribution of the voltage fluctuations in a steady bubbly flow regime: $j_\ell = 0$.
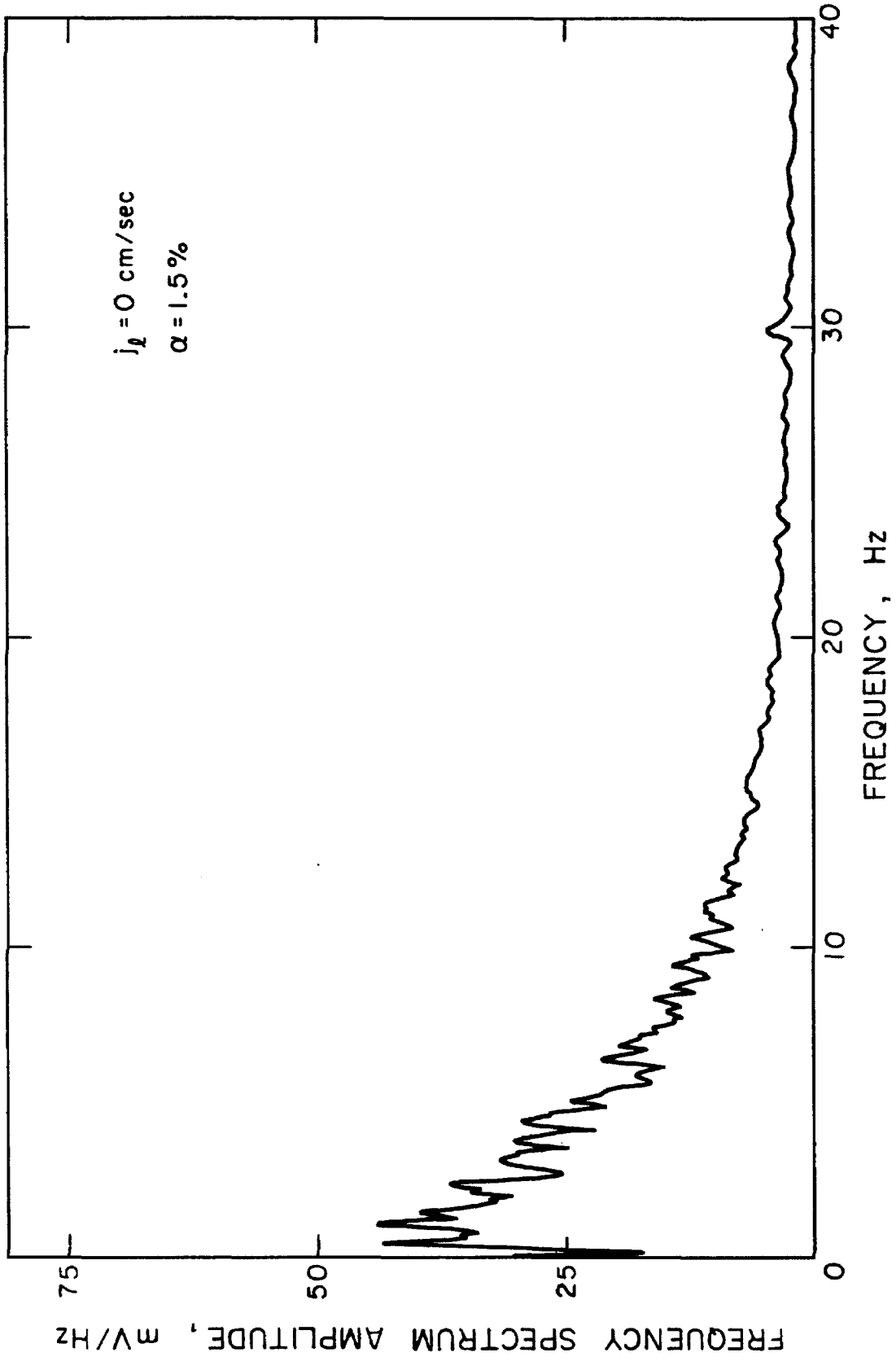
Figure 4.4 Typical frequency spectrum of the voltage fluctuations in a steady bubbly flow regime.
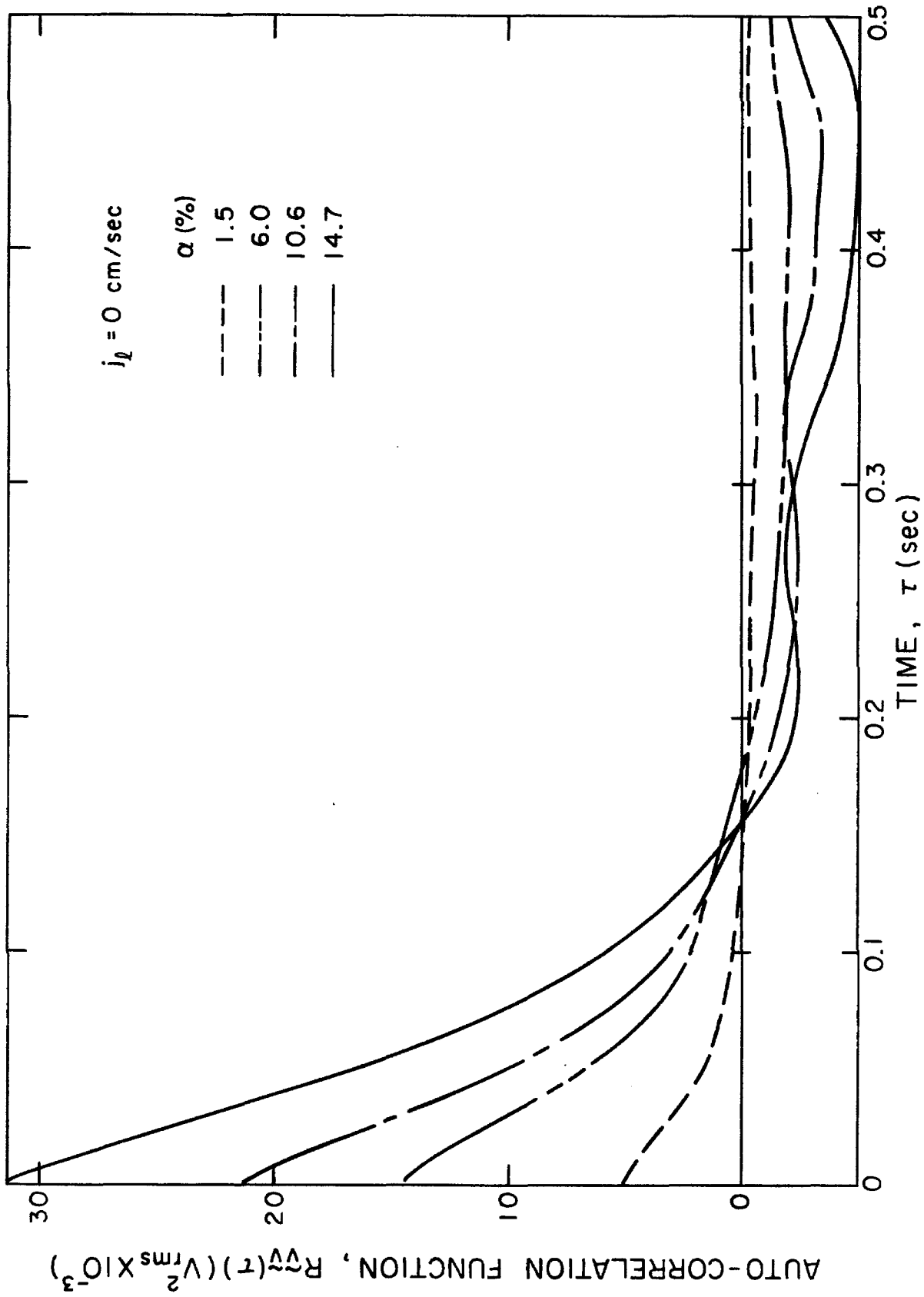
Figure 4.5 Typical auto-correlograms of the voltage fluctuations in a steady bubbly flow regime obtained from the Digital Signal Processor for a 40 sec. recording.
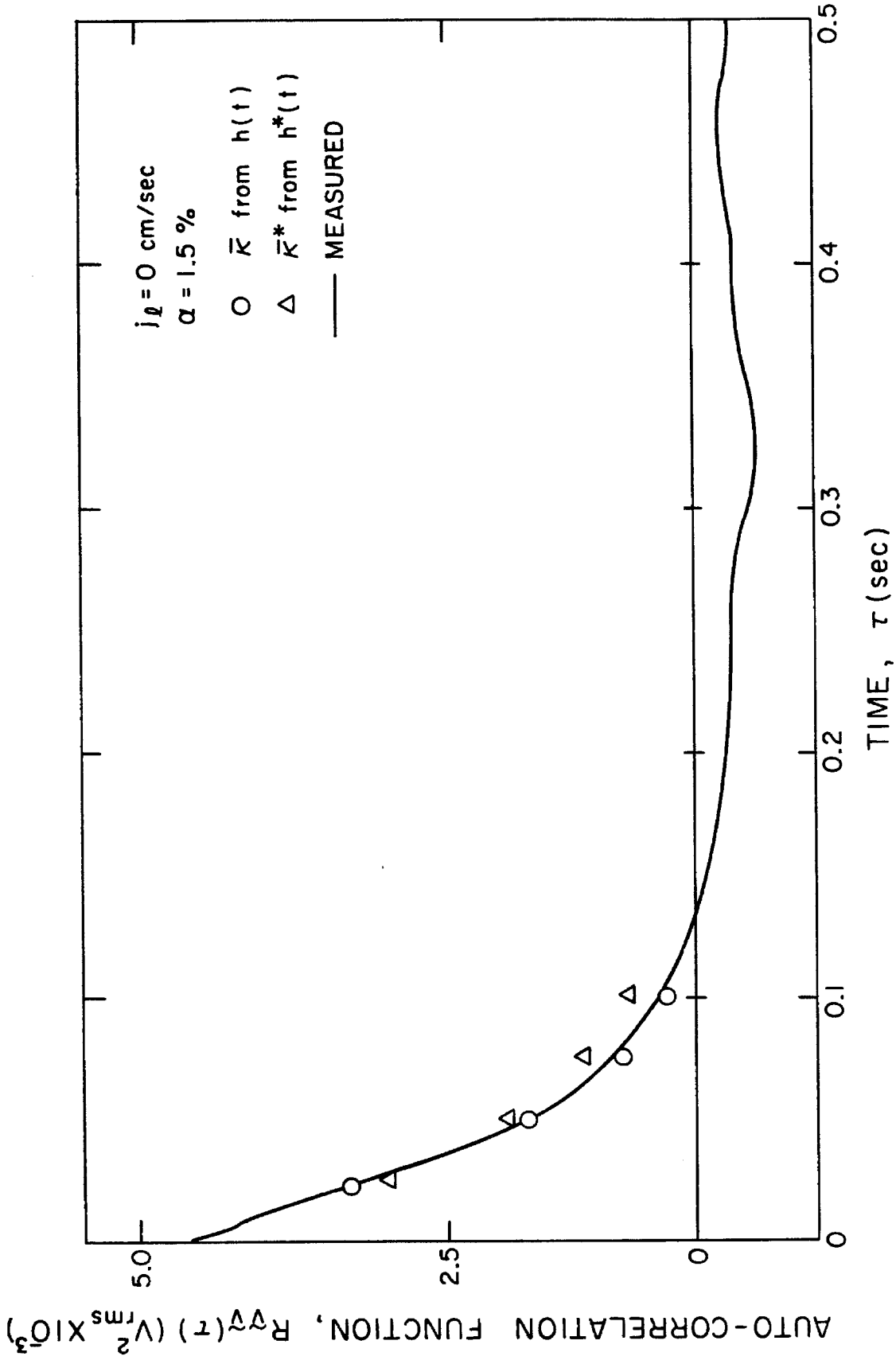
Figure 4.6 Auto-correlation function of the void fraction meter fluctuating voltage in a steady bubbly flow regime. The solid line is obtained from the DSP for a 40 sec. recording. The shot-noise auto-correlation function is indicated by circles for the filter described by Eq.4.17 and by triangles for the RC filter.
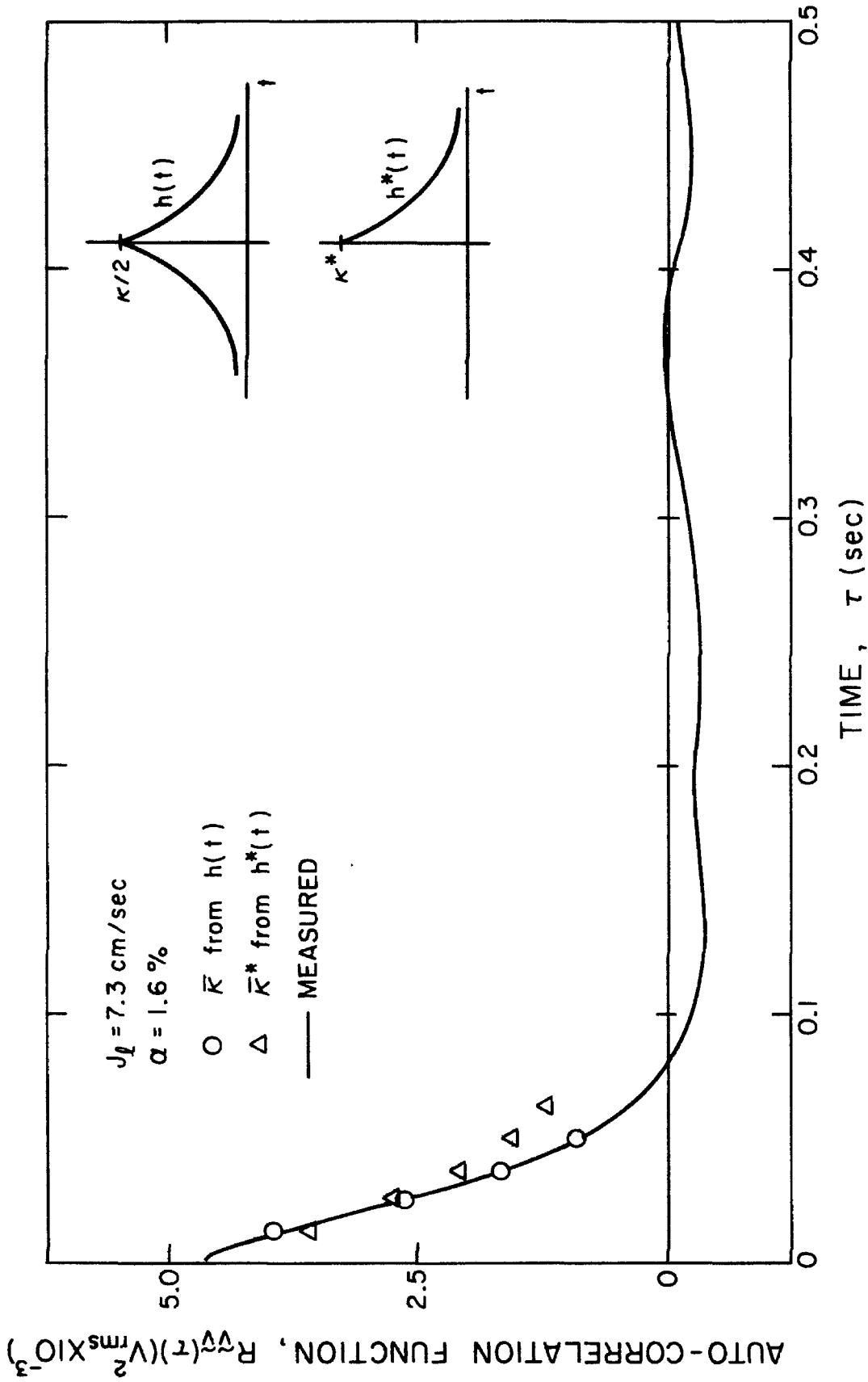
Figure 4.7 Auto-correlation function of the void fraction meter fluctuating voltage in a steady bubbly flow regime. The solid line is obtained from the DSP for a 40 sec. recording. The shot-noise auto-correlation function is indicated by circles for the filter described by Eq.4.17 and by triangles for the RC filter.
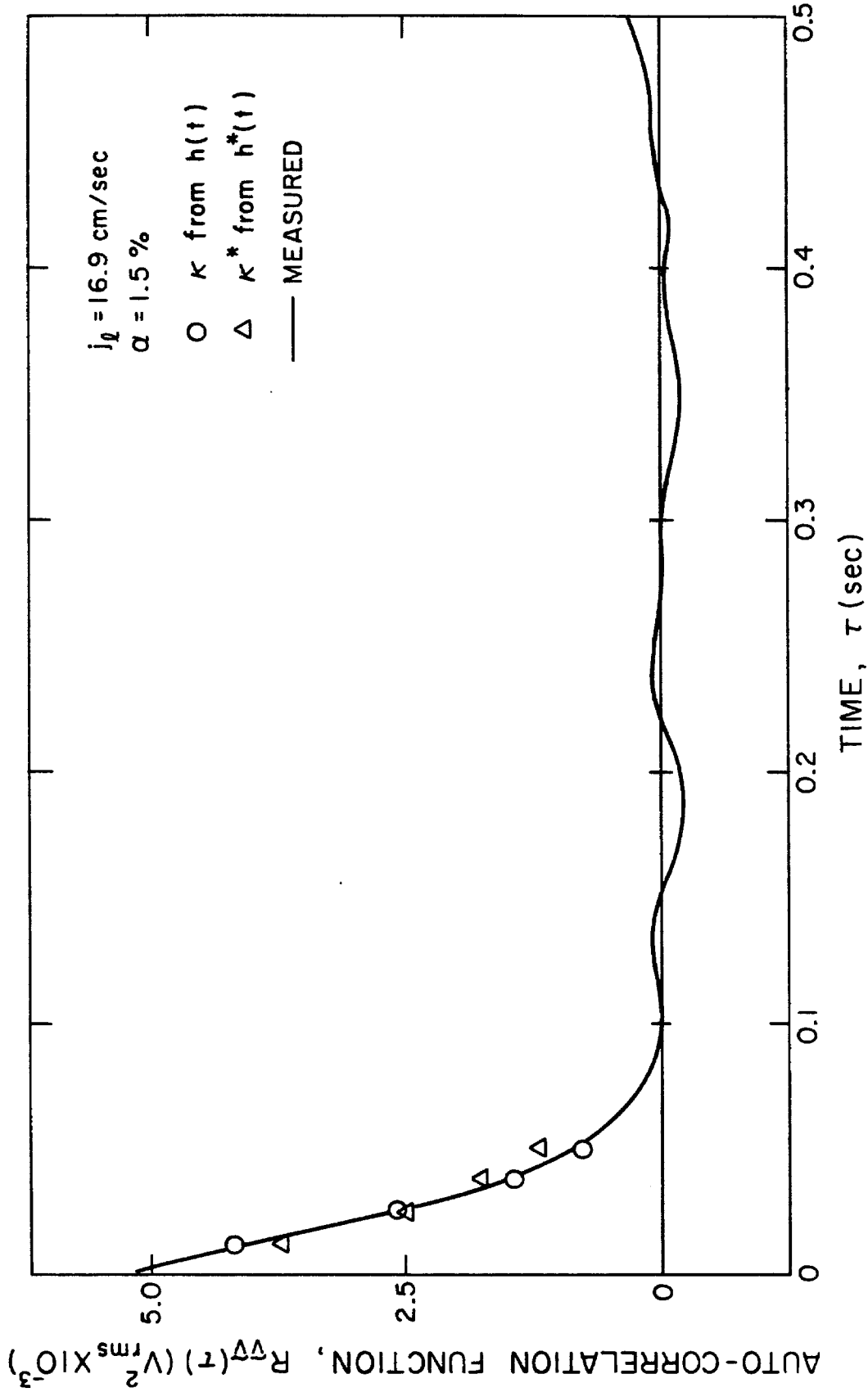
Figure 4.8 Auto-correlation function of the void fraction meter fluctuating voltage in a steady bubbly flow regime. The solid line is obtained from the DSP for a 40 sec. recording. The shot-noise auto-correlation function is indicated by circles for the filter described by Eq.4.17 and by triangles for the RC filter.
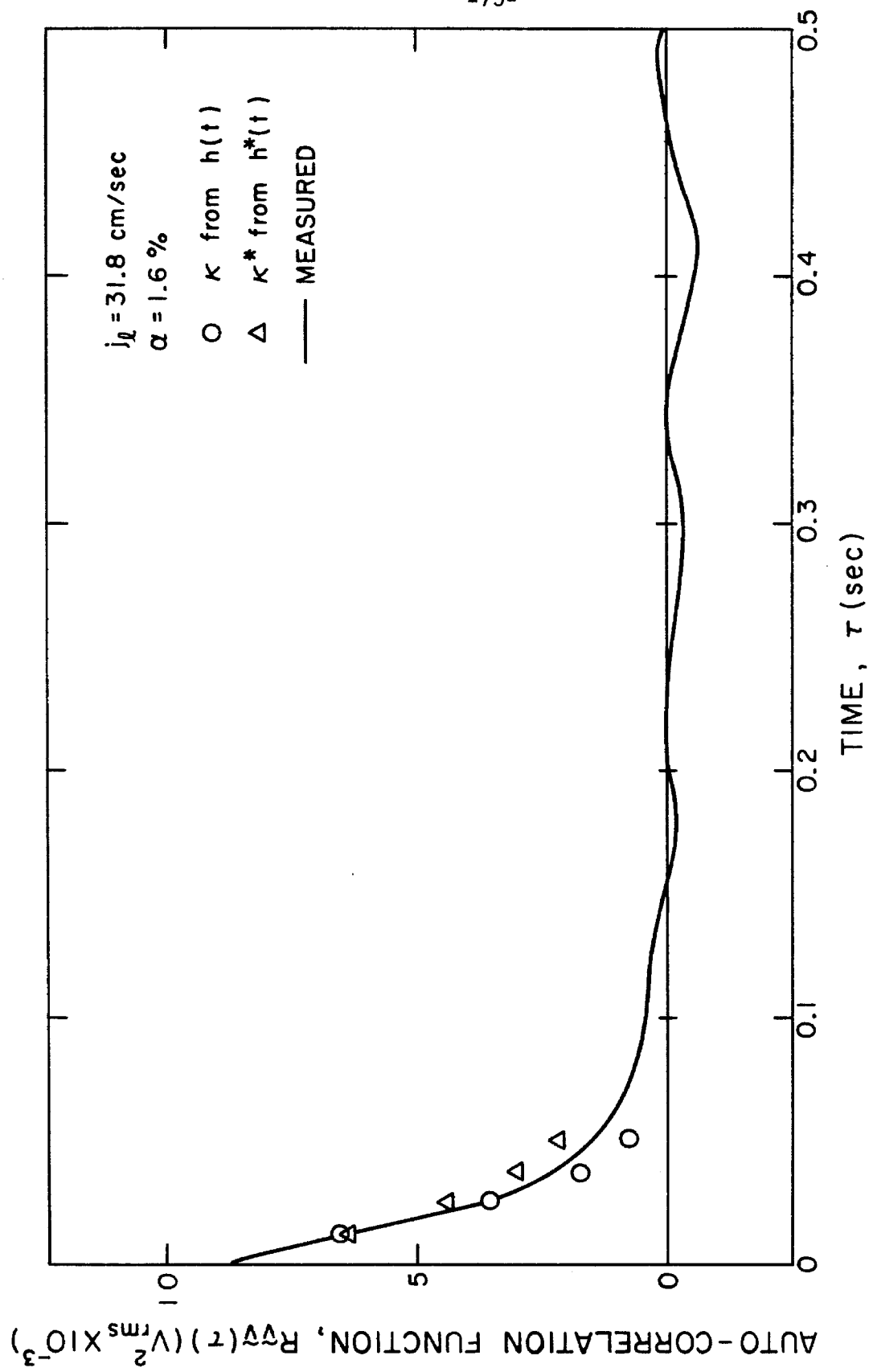
Figure 4.9 Auto-correlation function of the void fraction meter fluctuating voltage in a steady bubbly flow regime. The solid line is obtained from the DSP for a 40 sec. recording. The shot-noise auto-correlation function is indicated by circles for the filter described by Eq.4.17 and by triangles for the RC filter.

Table 4.1

j_ℓ cm/s	$\bar{\alpha}$ %	$\bar{\kappa}$ s^{-1}	$\bar{V}$ cm/s	$R_{\widetilde{VV}}(0) / \bar{V}^2$	D mm
0	1.46	46.49	21.21	1.66×10^{-2}	4.08
	5.96	37.22	20.21	4.456×10^{-3}	4.48
	10.61	37.54	19.33	1.662×10^{-3}	3.83
	14.69	32.69	18.48	1.233×10^{-3}	3.99
7.3	1.58	59.21	28.45	1.539×10^{-2}	4.15
	5.25	49.56	28.17	3.257×10^{-3}	3.94
	8.53	46.95	27.90	1.753×10^{-3}	3.80
	12.91	43.14	27.51	9.358×10^{-4}	3.71
16.8	1.46	68.52	38.12	1.821×10^{-2}	4.53
	4.28	59.78	38.46	4.087×10^{-3}	4.10
	7.38	65.61	38.86	2.145×10^{-3}	3.89
	11.56	60.2	39.44	1.257×10^{-3}	3.90
	15.11	53.31	39.98	9.199×10^{-4}	4.02
	19.30	50.85	40.68	5.439×10^{-4}	3.73
31.8	1.60	82.01	54.2	2.769×10^{-2}	5.70
	4.47	99.51	55.13	6.577×10^{-3}	4.65
	7.42	75.91	56.13	3.273×10^{-3}	4.82
	11.07	66.29	57.46	1.736×10^{-3}	4.69
	14.57	57.02	58.82	1.401×10^{-3}	5.08

Table 4.1   Value of the parameters entering in the calculation of the bubble diameter; j_ℓ is the water volumetric flux; $\bar{\alpha}$ is the average void fraction, $\bar{\kappa}$ is the weighted average constant of the filter function h(t), $\bar{V}$ is the absolute velocity of the disperse phase, $R_{\widetilde{VV}}(0)/\bar{V}^2$ is the square of the noise-to-signal ratio, D is the bubble diameter.
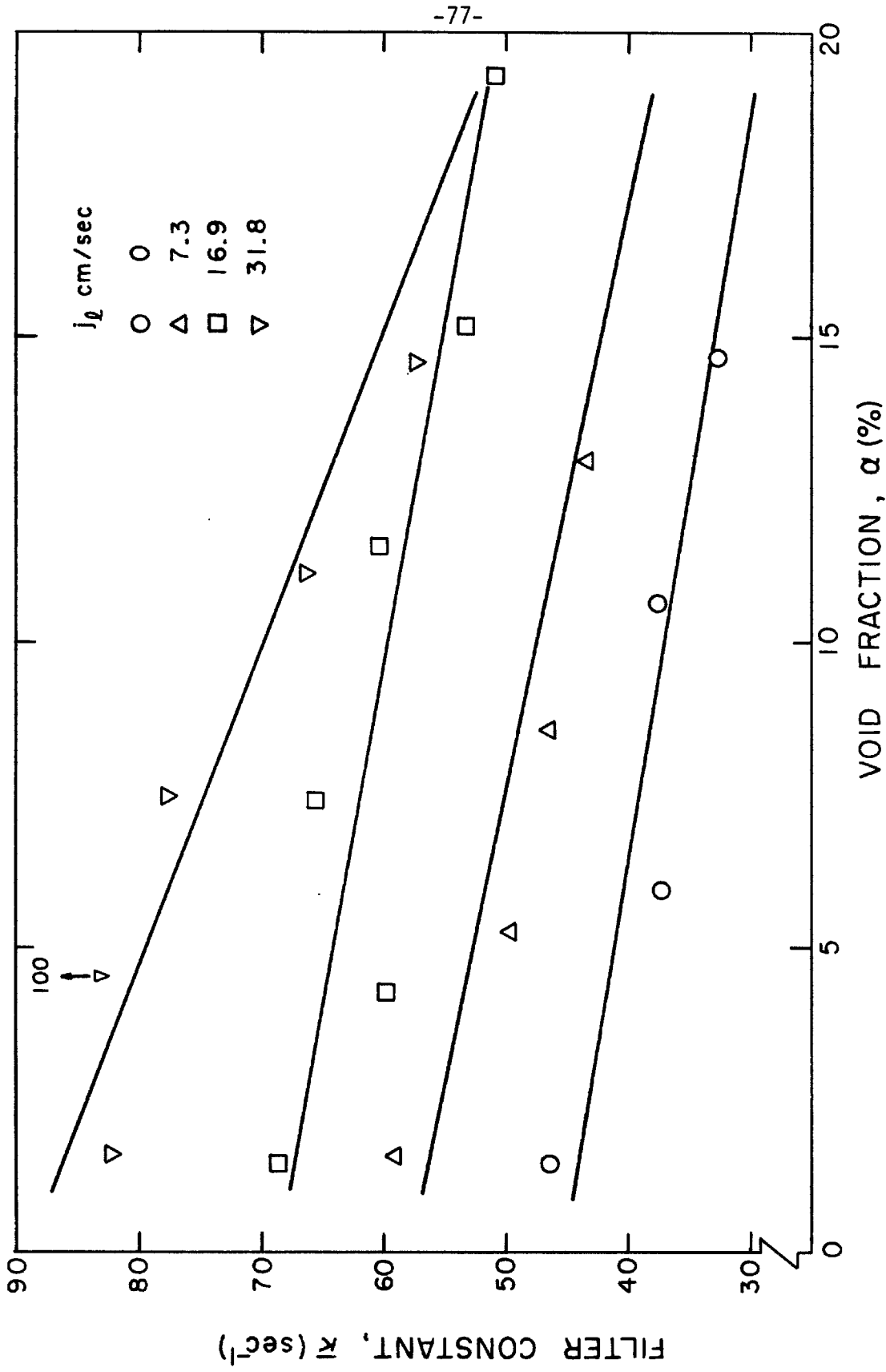
Figure 4.10 Effect of the void fraction on the constant associated with the electrode system filter h(t) defined by Eq.4.17. Solid lines are to emphasize the trend for a constant volumetric water flux.
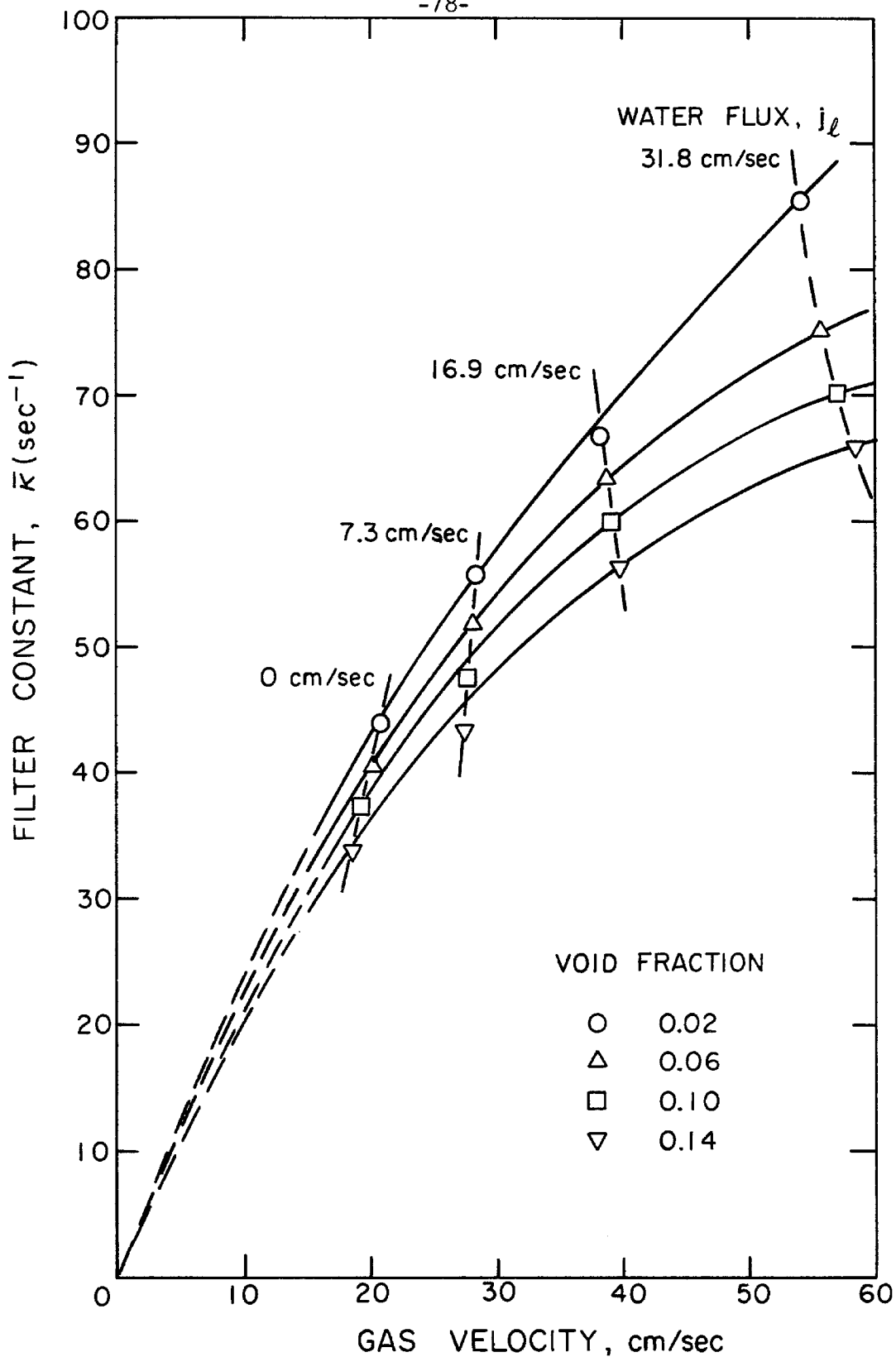
Figure 4.11   Cross plot of Fig.4.10 and Fig.5.6 showing the dependency
of the filter constant on the disperse phase absolute ve-
locity and the void fraction.
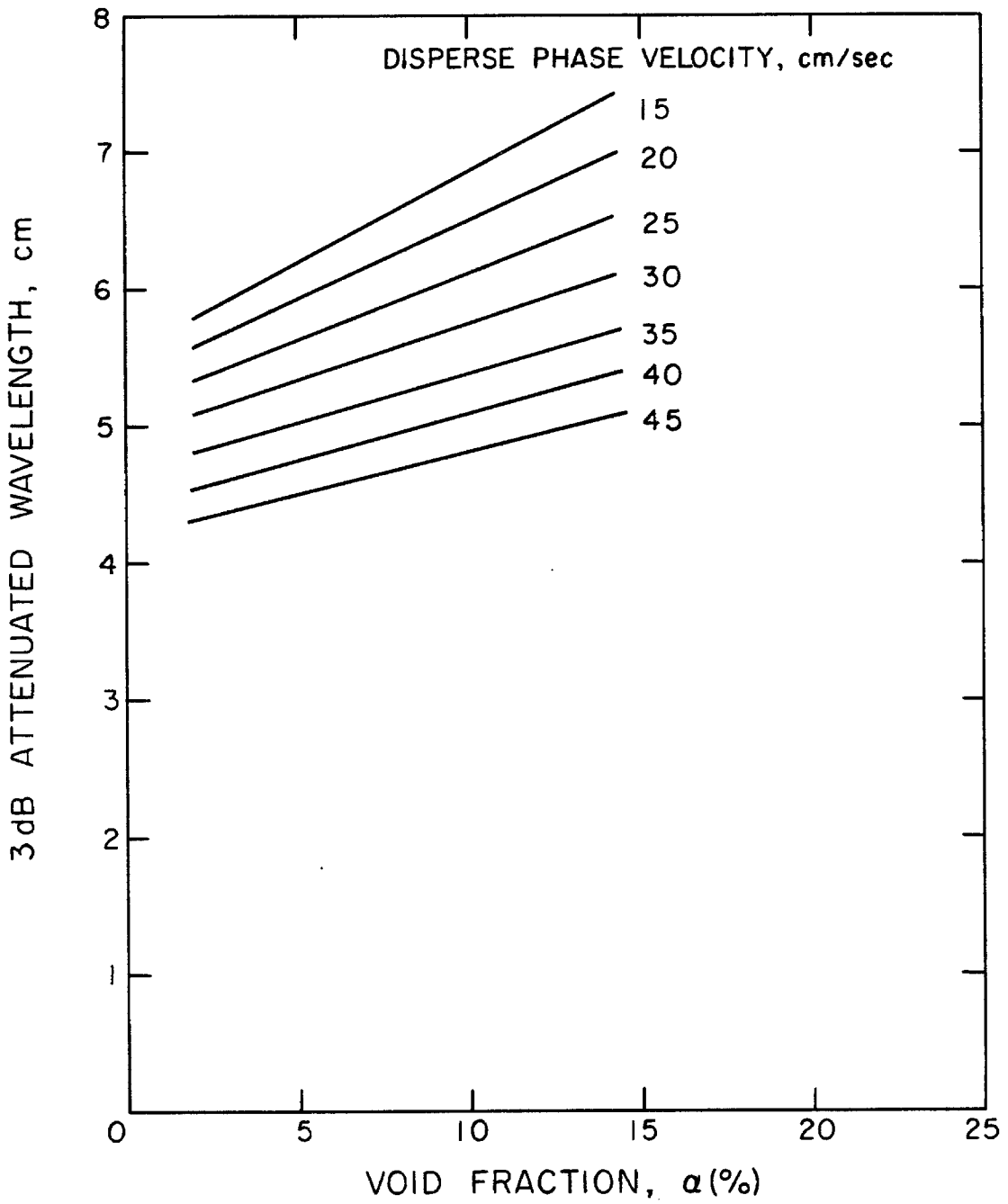
Figure 4.12   Effect of the void fraction and disperse phase absolute velocity on the void fraction wavelength attenuated by a 3dB factor at the output.

V. KINEMATIC WAVES: THEORY AND EXPERIMENTS

5.1 Introduction

In this chapter Zuber's formulation of the kinematic wave theory is derived as a particular case of the general equations for an incompressible bubbly mixture without heat and mass transfer. The purpose is to emphasize the slow transient approximation for which the model is valid. Also, it will be shown that the wave equation of the void fraction propagation can lead to the formation of shocks characterized by a macroscopic discontinuity in the disperse phase. The measurement of the propagation speed of shocks between regions of constant void fraction are then used to determine the relative velocity of the disperse phase. The good dynamic response of the void fraction meters which were used to track the shock propagation enabled us to look at the structure of such shocks. The substantial thickness in these shocks suggests that a diffusion mechanism is responsible for arresting the steepening of the wave.

5.2 Kinematic Wave Theory

5.2.1 Conservation Laws

The general description of a two-phase flow by continuum equations is obtained by time-averaging the governing equations of each phase as indicated by Ishii [23]. The mass conservation, momentum, and energy equations of each phase include interfacial transfer terms which need to be specified. These equations can be used directly as in the

two-fluid model or combined to form mixture equations as in the diffusion model. Symington [43] obtained a similar formulation in the case of a bubbly flow by applying the conservation laws to a volume element. For an incompressible gas without heat and mass transfer, the two continuity equations are

$$\frac{\partial}{\partial t} \alpha + \nabla \cdot \alpha \underset{\sim}{v} = 0 \tag{5.1}$$

for the gas (or disperse phase) and

$$\frac{\partial}{\partial t} [1 - \alpha] + \nabla \cdot [1 - \alpha] \underset{\sim}{u} = 0 \tag{5.2}$$

for the liquid (or continuous phase) where $\underset{\sim}{u}$ and $\underset{\sim}{v}$ are the gas and liquid velocities averaged over the volume element. The variable α is the void fraction defined as the volumetric concentration of the disperse phase. Neglecting the viscous stresses, the equation of motion for the mixture is written as

$$\rho_g \alpha \frac{D}{Dt} \underset{\sim}{v} + \rho_\ell [1 - \alpha] \frac{d}{dt} \underset{\sim}{u} = - \nabla p + \{ [1 - \alpha] \rho_\ell + \alpha \rho_g] \} \underset{\sim}{g} \tag{5.3}$$

where the material derivatives of each phase are

$$\frac{D}{Dt} = \frac{\partial}{\partial t} + \underset{\sim}{v} \cdot \nabla \tag{5.4}$$

and

$$\frac{d}{dt} = \frac{\partial}{\partial t} + \underset{\sim}{u} \cdot \nabla \cdot \tag{5.5}$$

In the mixture momentum equation, it is assumed that the square of the local (inside the volume element) velocity of each phase can be approximated by the square of their average velocity. This

approximation implies that terms similar to Reynolds stresses were neglected.

To complete the description of the bubbly flow model, the conservation laws need to be supplemented by an equation governing the relative motion of the bubbles in the liquid.

5.2.2 Bubble Equation of Motion

The equation of the relative motion of bubbles is obtained by considering the different forces acting on it. Many formulations have been proposed in the past, resulting in significant differences for the expressions of the four characteristic wave speeds present in a bubbly flow. For instance, Prosperetti and Van Wijngaarden's [40] equation leads to four real characteristic wave speeds, while Chernyy's [8] and later Symington's [43] formulation yield two imaginary characteristics associated with the transport speeds of the mixture and two real characteristics corresponding to the acoustic speeds.

By examining the relative magnitude of the forces acting on the bubble, we shall arrive at the expression of the relative motion of the bubble as used in Zuber's kinematic wave equation. For this purpose we will consider Symington's equation for incompressible bubbles which is

$$(\frac{1}{2}\rho_{\ell} + \rho_g) \frac{D}{Dt} \underset{\sim}{v} - \frac{3}{2} \rho_{\ell} \frac{d}{dt} \underset{\sim}{u} + \frac{\rho_{\ell}}{2\chi} (\underset{\sim}{v} - \underset{\sim}{u}) + (\rho_{\ell} - \rho_g)\underset{\sim}{g} = 0 \quad . \quad (5.6)$$

The first term is due to the bubble inertia and its added mass, while the second term accounts for the momentum given up by the liquid to accelerate the bubble. The third and fourth terms represent the viscous and buoyancy forces, respectively. The parameter χ in the drag

force is the viscous relaxation time; this is the time taken for a bubble to reach .63 of its terminal velocity when released from rest in a stagnant fluid. For a bubble of diameter D, Stokes' drag yields

$$\chi = \frac{D^2}{36\nu} \qquad (5.7)$$

where ν is the kinematic viscosity of the liquid. For Reynolds numbers based on the bubble diameter of 30-200, Batchelor's [3] formula for the drag can be used, giving a viscous relaxation time

$$\chi = \frac{D^2}{72\nu} \quad . \qquad (5.8)$$

The relative importance of each force can be assessed by expressing the bubble equation of motion in a dimensionless form. If U_0 and L_0 are the characteristic speed and dimension of the flow, and $t_0 = L_0/U_0$ is the characteristic time, the dimensionless form of Eq. (5.6) becomes

$$\left(\frac{\rho_g}{\rho_\ell} + \frac{1}{2}\right) \frac{D^*}{Dt^*} \underset{\sim}{v}^* - \frac{3}{2} \frac{d^*}{dt^*} \underset{\sim}{u}^* + \frac{L_0}{2U_0\chi} (\underset{\sim}{v}^* - \underset{\sim}{u}^*) + \left(1 - \frac{\rho_g}{\rho_\ell}\right) \underset{\sim}{g} \frac{L_0}{U_0^2} = 0 \quad . \qquad (5.9)$$

In many cases ρ_g/ρ_ℓ is small and the relative magnitude of the forces acting on the bubble is governed by two dimensionless groups: the Froude number $U_0/(gL_0)^{1/2}$ and the reduced frequency $\chi U_0/L_0$. For small values of $\chi U_0/L_0$, the inertial forces have little effect on the bubble motion and the bubble will react quasistatically, reaching its terminal velocity instantaneously. Slow transients refer to this particular situation where the relative motion of the bubble is governed by the drag and the buoyancy forces. Then, the relative velocity of the bubble depends only on the properties of the two fluids.

5.2.3 Effect of the Disperse Phase Concentration

In practice, the relative velocity of the disperse phase is generally a function of the disperse phase volumetric concentration. An increase in the drag with the concentration has been attributed to a change in the bulk properties of the mixture. Even though a single bubble is surrounded by the continuous phase, the presence of other bubbles alters the effective viscosity and density seen by this bubble. Theoretical analysis by Einstein [13], Batchelor [4] and many others on the rheology of suspensions has shown that the bulk viscosity is indeed a function of the concentration. The effect of the bulk density has been the object of controversy in the past. It was challenged on the basis that a particle or bubble still displaces its own volume of liquid. However, the experiments of Filderis and Whitmore [14] clearly show that a particle terminal velocity is related to the bulk density of the mixture.

In spite of the analytical work done on the rheology of suspensions, it is not possible to predict accurately the effect of the disperse phase concentration. The relative velocity of the disperse phase must therefore be determined experimentally.

5.2.4 One-Dimensional Wave Propagation of the Void Fraction

In this section we shall derive the void fraction wave equation for an incompressible bubbly mixture in which the relative motion depends on the properties of the fluids and the volumetric concentration of the disperse phase. Because the inertia of the bubble is neglected, the equation we shall arrive at is valid for slow transients

-85-

only.

For a one-dimensional uniform bubbly flow, the two equations of
continuity given by (5.1) and (5.2) become

$$\frac{\partial \alpha}{\partial t} + \frac{\partial}{\partial z} [\alpha v] = 0 \qquad (5.10)$$

and

$$\frac{\partial}{\partial t} [1 - \alpha] + \frac{\partial}{\partial z} [1 - \alpha]u = 0 \qquad (5.11)$$

where z is positive in the vertical upward direction. We first define
j, the average volumetric flux, as

$$j = \alpha v + [1 - \alpha] u \qquad (5.12)$$

where αv is the gas volumetric flux, j_g, and $(1 - \alpha)u$ is the water
volumetric flux j_ℓ. The addition of Eqs. (5.10) and (5.11) leads to

$$\frac{\partial}{\partial z} j = 0 \cdot \qquad (5.13)$$

Thus, the average volumetric flux j is a function of time only; j(t).
Another useful quantity is the gas drift flux, j_{gj}, which is the volu-
metric flux of the gas relative to the average volumetric flux given by

$$j_{gj} = \alpha[v - j] \qquad (5.14a)$$

or equivalently, if the definition of j is used,

$$j_{gj} = \alpha [1 - \alpha] v_{g\ell} \qquad (5.14b)$$

where $v_{g\ell}$ is the relative velocity of the disperse phase and, as pointed
out earlier, is a function of the void fraction only. Solving for v in

(5.14a) and substituting in Eq. (5.10) one gets

$$\frac{\partial}{\partial t} + \frac{\partial}{\partial z} [\alpha j + j_{gj}] = 0 \quad , \qquad (5.15a)$$

or more simply,

$$\frac{\partial \alpha}{\partial t} + [j + \frac{\partial}{\partial \alpha} j_{gj}] \frac{\partial \alpha}{\partial z} = 0 \quad . \qquad (5.15b)$$

If we define a velocity C_i as

$$C_i = j + \frac{\partial}{\partial \alpha} j_{gj} \quad , \qquad (5.16)$$

Eq. (5.15b) is finally written as

$$\frac{\partial \alpha}{\partial t} + C_i \frac{\partial \alpha}{\partial z} = 0 \quad . \qquad (5.17)$$

Equation (5.17) is illustrative of the wave-like propagation of the void fraction. The convective speed C_i can be looked upon as the speed at which a small disturbance in the void fraction would travel in a uniform steady bubbly flow in a vertical pipe.

5.2.5 Kinematic Shocks

Because C_i is a function of α, Eq. (5.17) is a nonlinear homogeneous partial differential equation. Solutions to initial value problems for this type of equation are best handled by the method of characteristics. Moreover, such equations are known to produce steepening or amplitude dispersion (as opposed to frequency dispersion) of the wave depending on the initial conditions and the explicit expression of the infinitesimal wave speed C_i. Steepening of the waves can lead to the formation of kinematic shocks characterized by a sharp discontinuity.

The phenomenon is similar to the formation of shocks in gas dynamics.

For an initial value problem, the method of characteristics yields the following solution for the void fraction propagation:

$$\alpha = \alpha(\xi) \tag{5.18}$$

where the variable ξ is given by

$$\xi = z - C_i \, \alpha_0(\xi) \, t \tag{5.19}$$

and α_0 is the initial condition on the void fraction at time zero.

$$\alpha_0 = \alpha(z,0) \, . \tag{5.20}$$

A kinematic shock occurs when two characteristics intersect in the z-t plane. This condition is expressed as

$$\frac{z - \xi_1}{C_i(\alpha_0(\xi_1))} = \frac{z - \xi_2}{C_i(\alpha_0(\xi_2))} \tag{5.21}$$

which implies that if $\xi_1 < \xi_2$ then $C_i[\alpha_0(\xi_1)] > C_i[\alpha_0(\xi_2)]$. Thus the void fraction $\alpha_0(\xi_1)$ moves faster than $\alpha_0(\xi_2)$ and eventually catches up with $\alpha_0(\xi_2)$. When a shock is formed, it then satisfies the following jump condition:

$$[\alpha_2 - \alpha_1] + \frac{1}{C_s} \{[\alpha_2 j_2 + j_{gj_2}] - [\alpha_1 j_1 + j_{gj_1}]\} = 0 \tag{5.22}$$

which is obtained from the continuity of the partial derivative of equation (5.15a) in a direction parallel to the shock. The subscripts 2 and 1 refer to conditions above and below the discontinuity. C_s is the speed at which the shock propagates and its inverse is the slope of

the characteristic line in the z-t plane supporting the discontinuity. Because j is a function of time only, it assumes the same value above and below the shock. The speed of the shock is then given by

$$C_s = j + \frac{[j_{gj_2} - j_{gj_1}]}{[\alpha_2 - \alpha_1]} \quad . \tag{5.23}$$

From an experimental standpoint, Eq. (5.23) is most valuable. For instance, if j is constant and the void fraction is zero below the shock (or above, depending on the expression of C_i) and constant above with a value α, the shock speed becomes

$$C_s = u_s + [1 - \alpha] \, v \tag{5.24}$$

where j has been evaluated in the region of zero void fraction, and j_{gj} has been substituted by Eq. (5.14b). Defining C_s^* as the speed of the shock relative to the liquid velocity u_s behind the shock, the relative velocity of the disperse phase is simply

$$v_{g\ell} = \frac{C_s^*}{[1 - \alpha]} \quad . \tag{5.25}$$

Furthermore, by substituting (5.25) in (5.14b) and also in (5.12), the infinitesimal wave speed C_i is then

$$C_i = u + \frac{C_s^*}{1-\alpha} + \alpha \, \frac{\partial C_s^*}{\partial \alpha} \tag{5.26}$$

and in a frame relative to the liquid velocity u in the bubbly mixture, this speed becomes

$$C_i^* = \frac{C_s^*}{(1-\alpha)} + \alpha \, \frac{\partial C_s^*}{\partial \alpha} \quad . \tag{5.27}$$

It is readily observed from Eqs. (5.25) to (5.27) that the measurement of this particular shock for different void fraction would enable us to obtain a correlation for the disperse phase relative velocity as a function of α. This correlation determines entirely the motion of the disperse phase propagating in the form of concentration waves relative to the liquid velocity.

5.3 Experiment on Kinematic Shocks

5.3.1 Experimental Procedure

The purpose of this set of experiments is to measure the propagation speed of kinematic shocks in an air-water bubbly mixture flowing in a vertical pipe. The experiment was conducted in the test loop already described in Section 3.4.1. Two void fraction meters placed 83.8 cm apart were used to detect the passage of the void fraction discontinuity. The first was installed in the middle of the test section to allow enough time for the shock formation. The distance of the second from the exit was approximately 43 cm. Figure 5.1 illustrates the experimental set-up.

The output voltages of the void fraction meters were recorded on a HP model 7418A multichannel strip chart recorder and by an Ampex model SP300 magnetic tape recorder. The air supply line leading to the air injector was fitted with a manually actuated on-off valve.

Following the establishment of a steady bubbly flow in the pipe, the void fraction meter situated at the test section mid-point was used to measure the void fraction. The D.C. signal was averaged over a period of 60 seconds at a sampling rate of 32 points per second, using a

Motorola M6800 digital microprocessor. The data file accumulated by the microprocessor was subsequently transmitted to the VAX central computer for data reduction. The actual value of the void fraction was then evaluated from the calibration curve of Fig. 3.4.

To produce a step change in the void fraction, the air supply valve was quickly shut off. Typical recordings of the passage of a kinematic shock are shown in Fig. 5.2 for different values of the void fraction and various water velocities behind the shock. The passage of the shock at the metering station is indicated by a relatively sharp drop in the D.C. level of the signal. The upward propagation of the shock is first detected by the midpoint meter corresponding to the bottom signal. The time progression is from left to right indicated by the arrow. These recordings are for shocks where the void fraction below the discontinuity is zero.

Both the strip chart and the magnetic tape recordings were used to measure the shock transit time between the void fraction meters. The strip chart recordings were manually fitted with straight lines matching the dominant slope of the voltage drop and the steady state signal on each side of the wave. As indicated in Fig. 5.2a the times t_2, t_1 and t_2', t_1' denote the intervals between the beginning and the end of the passage of a wave at each measuring station. The transit time was taken as the difference between the mean of the intervals t_2, t_1 and t_2', t_1'. Cross-correlation of the magnetic tape readings using a digital signal processor was also attempted. Both signals were first stripped from their D.C. components by the built-in high pass filters with a

0.47 second time constant. The measurement of the transit time was done by cross-correlation of the filter responses which reacted to the drop in the D.C. signals. This method turned out to give less consistent results than the strip chart recording approach. This was particularly noticeable when the void fractions above the discontinuity were small. For these cases, the maximum similarity criterion sought by the cross-correlation function was biased by the relatively high amplitude of the voltage fluctuations compared to the amplitude of the voltage drop.

The results presented hereafter were evaluated from the strip chart recordings only. The shock speeds are the mean of 3 repeated measurements for a given initial steady state condition.

5.3.2   Kinematic Shocks in Stagnant Water

For different constant void fractions above the shock and a zero void fraction below, the measurements of the kinematic shock speed in an air-water bubbly mixture are shown in Fig. 5.3. The velocity behind the shock is zero. Also shown is the relative velocity $v_{g\ell}$ of the disperse phase calculated from Eq. (5.25). In this particular case, the relative speed of the shock C_s^* is evidently the absolute speed C_s. This is the speed at which the disperse phase is moving upward following the establishment of the shock. As indicated by Eq. (5.25), the relative speed $v_{g\ell}$ is greater by a factor $1/1-\alpha$. This factor accounts for the counterflow the bubbles experience as the liquid is drained from the two-phase region.

In Fig. 5.3 the effect of the concentration on the relative velocity is clearly seen. The decreasing value of $v_{g\ell}$ as a function of the void fraction is consistent with the results obtained by Nicklin [36] for an air-water system.

5.3.3 Shocks of Decreasing Strength in Stagnant Water

The purpose of this experiment is to verify if the information obtained from the measurements of shock speed can be used to predict other situations involving the propagation of kinematic waves or shocks.

The experiment consisted of producing shocks of decreasing strength between two regions of constant void fraction. The water in the test section is at rest before the shock is created. The value of the void fraction above the shock was kept constant for each increment in the value of the void fraction below the shock. The measurements of the shock speed C_s^{**} are shown in Fig. 5.4 as data points for void fractions of 16.6% and 22.0% above the shock.

In terms of the measurements presented in the previous section, the shock speed C_s^{**} can be predicted according to the following equation

$$C_s^{**} = j + \frac{[\alpha_2 C_s^*(\alpha_2) - \alpha_1 C_s^*(\alpha_1)]}{[\alpha_2 - \alpha_1]} . \qquad (5.28)$$

This equation is obtained from Eq. (5.23) where the definition of j_{gj} given by Eq. (5.14b) and Eq. (5.25) have been used. The subscripts 2 and 1 refer to conditions above and below the shock, as before. An expression involving only C_s^* can be obtained by noting that below the shock the velocity of the water is zero. The volumetric flux j_1 below

the shock is therefore

$$j_1 = \alpha_1 v_1 \qquad (5.29)$$

where v_1, the speed of the disperse phase, is also its relative speed $v_{g\ell}(\alpha_1)$. Once more, making use of Eq. (5.25) to substitute for v_1, the shock speed C_s^{**} becomes

$$C_s^{**} = \alpha_1 \frac{C^*(\alpha_1)}{[1 - \alpha_1]} + \frac{[\alpha_2 C_s^*(\alpha_2) - \alpha_1 C_s^*(\alpha_1)]}{[\alpha_2 - \alpha_1]} \qquad . \qquad (5.30)$$

The solid lines superimposed on Fig. 5.4 are calculated from the data of Fig. 5.3 using Eq. (5.30). The agreement between the predicted and measured values of C_s^{**} is excellent. As the ratio α_1/α_2 approaches unity, the experimental data converge towards the infinitesimal wave speed which is obtained by expressing the second term on the RHS of Eq. (5.30) as a differential. This wave speed corresponds to the velocity at which a small perturbation in the void fraction propagates in steady bubbly flow.

5.3.4 Kinematic Shocks in Non-Zero Water Volumetric Fluxes

In view of the experiment reported in the last section, the method of characterizing a two-phase gravity dominated flow by measurement of shock speeds gives excellent results. However, before drawing general conclusions on the method, we need to investigate the effect of a non-zero liquid volumetric flux.

For different constant water volumetric fluxes, j_ℓ, the speeds of kinematic shocks having a zero void fraction behind the shock were

measured. The water volumetric flow rate was monitored by an electro-magnetic flow meter before the air injection point. For a constant water flux, shocks were produced over a range of discrete values of the void fraction. All the runs were done with the discharge at atmospheric pressure and upward cocurrent gas/liquid flows.

Figure 5.5 is a summary of the shock speeds C_s^* relative to the water velocity behind the shock for water constant fluxes of 7.3 cm/s, 16.9 cm/s, and 31.8 cm/s. The case j_ℓ equal to zero is also included for comparison. Using Eq. (5.25), the relative velocity of the disperse phase was calculated. These results are shown in Fig. 5.6.

A striking feature of both figures is the change in the slope of $C_s^*(\alpha)$ and $v_{g\ell}(\alpha)$ as the water flux increases. The relative velocity of the disperse phase becomes less dependent on the volumetric concentration α and for j_ℓ equal to 31.8 cm/s, $v_{g\ell}$ is completely independent of the void fraction. Further verification of this behavior was obtained for a 47.3 cm/s water flux, but only at large void fraction as seen in Fig. 5.7. This figure also illustrates the limitations of the shock technique. More will be said on this in the next section.

The reason why the influence of the void fraction is less impor-tant as the water flux increases is not totally understood. Zuber et al. [50] speculate that in a turbulent bubbly flow regime the effect of the concentration is negligible compared to the effects of the liquid eddies. However, it was not possible in the present experiment to verify whether the gradual uncoupling between concentration and dis-perse phase relative velocity was due to a change in the turbulence level.

5.3.5 Limitation of the Method of Shocks

It was observed that for water fluxes greater than 31.8 cm/s, the method of shocks began to yield inaccurate data on the gas relative velocity. The explanation for this came from a simple but instructive experiment. For different constant water volumetric fluxes, triangular pulses of bubbles with a peak value less than 2% were injected in the test section and tracked by the two void fraction meters. The response of the meters to the passage of these pulses could be visualized on the strip chart recorder.

Because the pulses consisted of a very low void fraction, negligible deformation of the pulse should have been observed since the infinitesimal wave speed relative to the liquid velocity is close to the relative velocity of the gas. This indeed was the case at low water velocities; the pulse retained its shape from one measuring station to the other as seen in Fig. 5.8a. The lower trace belongs to the void fraction meter in the mid-test section, while the upper trace is that of the meter situated downstream. However, at large water velocities, a steepening front in the wave was observed as typified by Fig. 5.8b.

The change in shape of the void fraction wave occurred within a a small range of water velocities. This is emphasized by Fig. 5.9 where the speed of the pulses plotted as a function of the liquid velocity has been evaluated in two different ways. The pulses were first fitted with straight lines. In one case, as indicated by circles, the pulse transit time was measured by considering the interval between the trailing edges while in the other case the measurement was carried using the peak values. Below a water velocity of approximately 35 cm/s, the two methods yield

an identical speed for the pulse which corresponds to the water velocity plus an offset due to the relative velocity of the bubbles. However, above 35 cm/s, the trailing edge method departs from the 45° slope shown as a solid line. This critical velocity corresponds to the point beyond which the shock technique yielded incoherent results. Above that speed, it would appear that the gas phase is not convected uniformly across the pipe. When this happens the shock structure is believed to become two-dimensional leading to the ambiguous interpretation of the voltage drop recordings. Because the transit time of the shock is small for higher water fluxes, the error in determining the actual mean of the intervals $t_1 t_2$ and $t_1' t_2'$ becomes significant.

5.4 Shock Thickness

5.4.1 Measurement of the Slope in the Transition Region

The good dynamic response of the void fraction meter enabled us to look at the structure of the shocks between regions of constant void fraction. Typical strip chart recordings of the void fraction meter response following the passage of shocks were presented in Fig. 5.2. Shown in Figs. 5.10 and 5.11 are photographs of shocks.

Referring to Fig. 5.2a, the slope G of the transition region was evaluated as

$$G = -\frac{\alpha_2 - \alpha_1}{t_2 - t_1} \qquad (5.31)$$

where the subscripts 2 and 1 refer to conditions above and below the shock. Figure 5.12 is a summary of the slopes measured in the case

where α_1 is zero for water volumetric fluxes of 0, 7.3, 16.9, and 31.8 cm/s. The measurements were evaluated from the recordings of the meter installed in the middle of the test section. Similar measurements of the slope were obtained for the downstream void fraction meter.

5.4.2 Determination of the Shock Thickness

The evaluation of the thickness of the shock available from the strip chart recordings is not very meaningful unless a permanent waveform has developed. Comparison of the slopes obtained from the two void fraction meters showed that the shock structure could be considered as such. The existence of a permanent wave solution allows us to find a relation between the local rate of change of the void fraction (which is obtained from the strip chart recordings) and the gradient of the void fraction within the permanent wave. This relation is

$$\frac{\partial \alpha}{\partial t} = - U \frac{\partial \alpha}{\partial z} \qquad (5.32)$$

where U is the speed of the wave. Substituting the partial derivatives by finite differences, and approximating U by C_s, the speed of the shock, the shock thickness Δz is given by

$$\Delta z = \frac{1}{C_s \Delta t} \qquad (5.33)$$

where C_s is known from the previous experiments and Δt is available from the slope measurements.

5.4.3 Correction Due to the Void Fraction Meter Time Response

The measured slopes could be corrected for the time response of the void fraction meter according to the following procedure. Using

the general expression of the filter function h(t) defined by Eq. (4.17), the response of the meter was calculated for a transition of finite slope $[\alpha_2 - \alpha_1] / \tau$ as illustrated in Fig. 5.13abc. The maximum slope of the output signal occurs at the origin of the time axis leading to

$$G = -\frac{\alpha_2 - \alpha_1}{\tau} [1 - e^{-\frac{\kappa|\tau|}{2}}] .$$
(5.34)

For a given speed of the shock, the filter constant, κ, was approximated from Fig. 4.11 and the actual slope $(\alpha_2 - \alpha_1) / \tau$ was evaluated. The corrections turned out to be negligible at small void fractions. At larger void fractions for which the slopes are steeper, the corrections were of the order of 10%.

5.4.4 Shock Thickness Measurements

The actual shock thickness is plotted as a function of the shock strength $(\alpha_2 - \alpha_1)$ in Figs. 5.14 to 5.17 for different water fluxes. The thicknesses measured at the upstream void fraction meter (circles) are generally smaller than those measured downstream (triangles). However, the change in thickness is quite small in comparison to the 83.8 cm travelled by the shock. The approximation of the shock by a permanent wave is therefore justified.

As the difference $(\alpha_2 - \alpha_1)$ becomes larger, the thickness of the shock becomes smaller. For the zero water flux, this thickness is of the order of 5 bubble diameters at large void fractions. Reported on Fig. 5.14 are the thicknesses obtained from the experiment on shocks of decreasing strength (Section 5.3.3). In these experiments α_1 is not zero but assumes different values, while α_2, the void fraction above

the shock, is constant. These results show a remarkable agreement with the measurements for which α_1 is zero. This would indicate that the shock thickness is controlled primarily by the difference in the void fraction on each side of the shock.

It can be seen that for a given void fraction the shock thickness increases with the water volumetric flux. This particular trend is not readily accounted for. From the photographs, it was observed that some shocks were oblique but their limited occurrence was not greater than in the case of still water. The existence of a two-dimensional shock profile created by the slower motion of bubbles near the wall of the pipe would also result in the measurement of larger thicknesses, but such profiles were not seen. In the next section, we speculate on the existence of a diffusion term in the void fraction wave equation which would be responsible for the arrest of the shock steepening. It might well be that this term is dependent on the water volumetric flux.

5.4.5 Modified Wave Equation

The kinematic wave equation given by Eq. (5.17) does not rule out the existence of a permanent wave if C_i is independent of the void fraction α . However, from the data collected on $v_{g\ell}$, C_i is a mono-tonically decreasing function of α, which leads to the formation of a shock if the void fraction is increasingly larger in the direction of the wave propagation. Within the shock, the effects of diffusion would appear important in arresting the steepening of the wave profile. Mathematically, the diffusion of the kinematic wave corresponds to the inclusion of an additional term proportional to the second derivative

in α. If such a term is included, then the kinematic wave equation would be

$$\frac{\partial \alpha}{\partial t} + C_i(\alpha)\frac{\partial \alpha}{\partial z} = \beta \frac{\partial^2 \alpha}{\partial z^2} \quad . \tag{5.35}$$

Interestingly, the equation has a permanent wave solution, $\xi = z - Ut$, when the void fractions α_2 and α_1 on each side are constant. It can be shown that the speed U of the permanent wave is identical to the speed of the shock given by Eq. (5.23). Moreover, the permanent wave has a thickness δ^* defined as

$$\delta^* = \frac{\alpha_2 - \alpha_1}{\left.\dfrac{\partial \alpha}{\partial \eta}\right|_{max}} \tag{5.36}$$

which assumes the value

$$\delta^* = \frac{4\beta}{(\alpha_2 - \alpha_1)v_{g\ell}} \tag{5.37}$$

when the diffusivity coefficient, β, and the relative velocity of the disperse phase, $v_{g\ell}$, are independent of α. The dependence of δ^* on the strength of the wave $(\alpha_2 - \alpha_1)$ is qualitatively the one observed in our experiments. The measurements indicate that the diffusion coefficient would be comprised between 1.5 and 6 cm^2/sec.

How the diffusion term can be justified from first principles is not clear at this point. Symington arrived at a similar expression for waves of small strength by considering the inertia of the bubbles. However, his permanent wave solution is valid only for the case when the larger void fraction is below the wave. Also, the thickness he obtained is smaller than those measured by an order of magnitude. The definition of the gas drift flux by Ishii [23] as

$$j_{gj} = \alpha(1-\alpha)v_{g\ell} - \beta \frac{\partial \alpha}{\partial z} \qquad (5.38)$$

is compatible with the form of Eq. (5.33) but unfortunately little is said to explain the dependence of j_{gj} on the void fraction gradient.

In the mixture equation of motion, stress terms due to the local fluctuation of the phase velocities may have a significant effect. These terms are similar to Reynolds stresses in turbulent flow. For instance, the thickness of a gas dynamic shock is due to the irreversible dissipation of the kinetic energy caused by the compressive stress term (see Ref. [29]). A similar process may be causing the finite thickness of shocks observed in the present experiments.

5.5 Conclusions

The kinematic wave theory is a simple formulation which retains the essential features of an incompressible one-dimensional two-phase flow. As shown by Zuber et al. [50], the model can accommodate other flow regimes with or without mass transfer. In the case of an air-water bubbly mixture, the properties of the kinematic shocks were used to determine the relative velocity of the disperse phase. This velocity is a decreasing function of the void fraction, but its dependence seems greatly affected by the turbulence of the flow. The shock technique has limitations when the flow can no longer be considered one dimensional.

The measurement of the shock thickness suggests a diffusion mechanism responsible for the arrest of the wave steepening. As will be shown in the next chapter, diffusion is also observed in small

amplitude waves at low frequency.   However, the diffusion mechanism cannot be identified at this point.
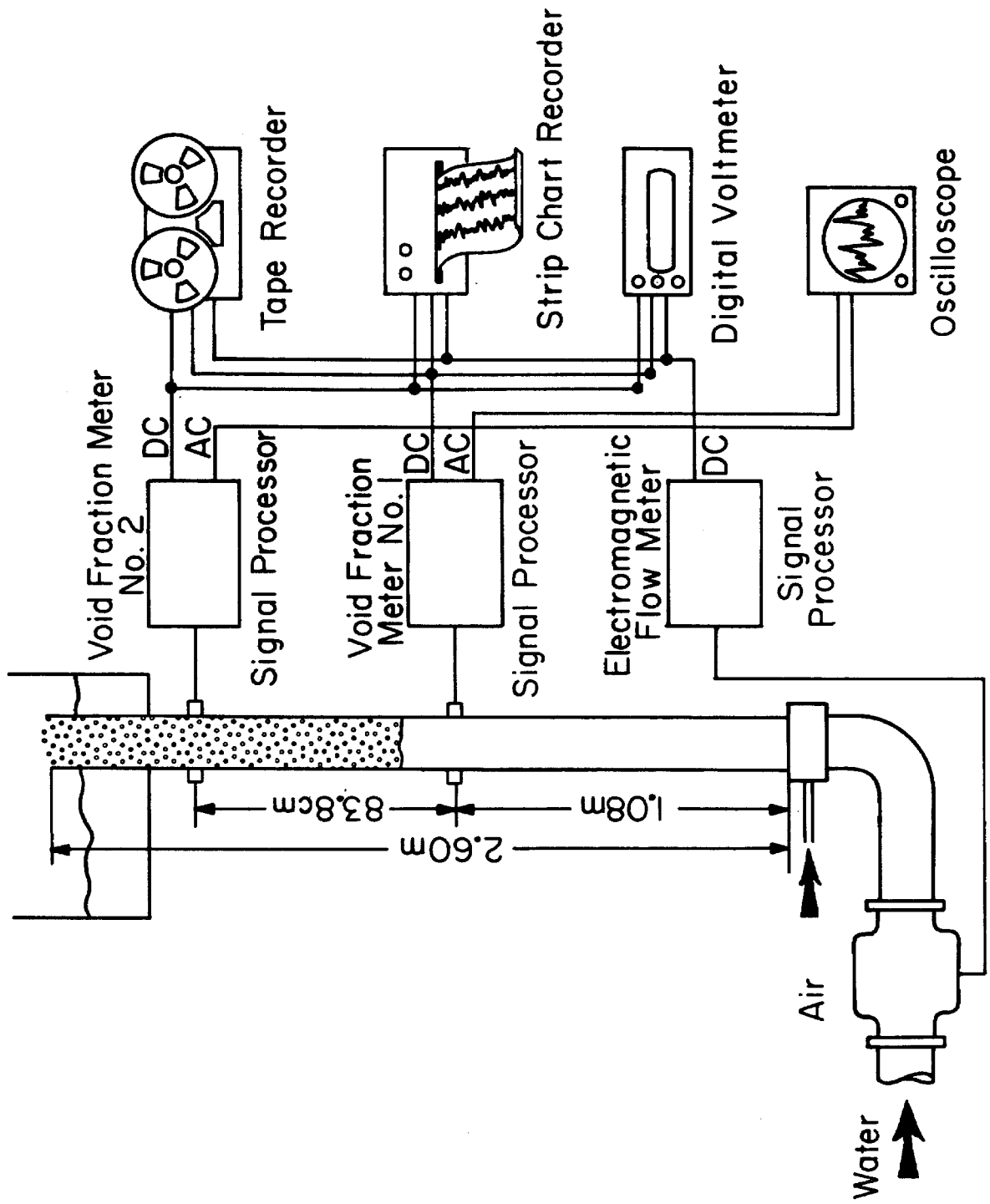
Figure 5.1 Schematic view of the experimental set-up for the measurement of kinematic shock propaga- tion speeds in an air-water bubbly flow regime.
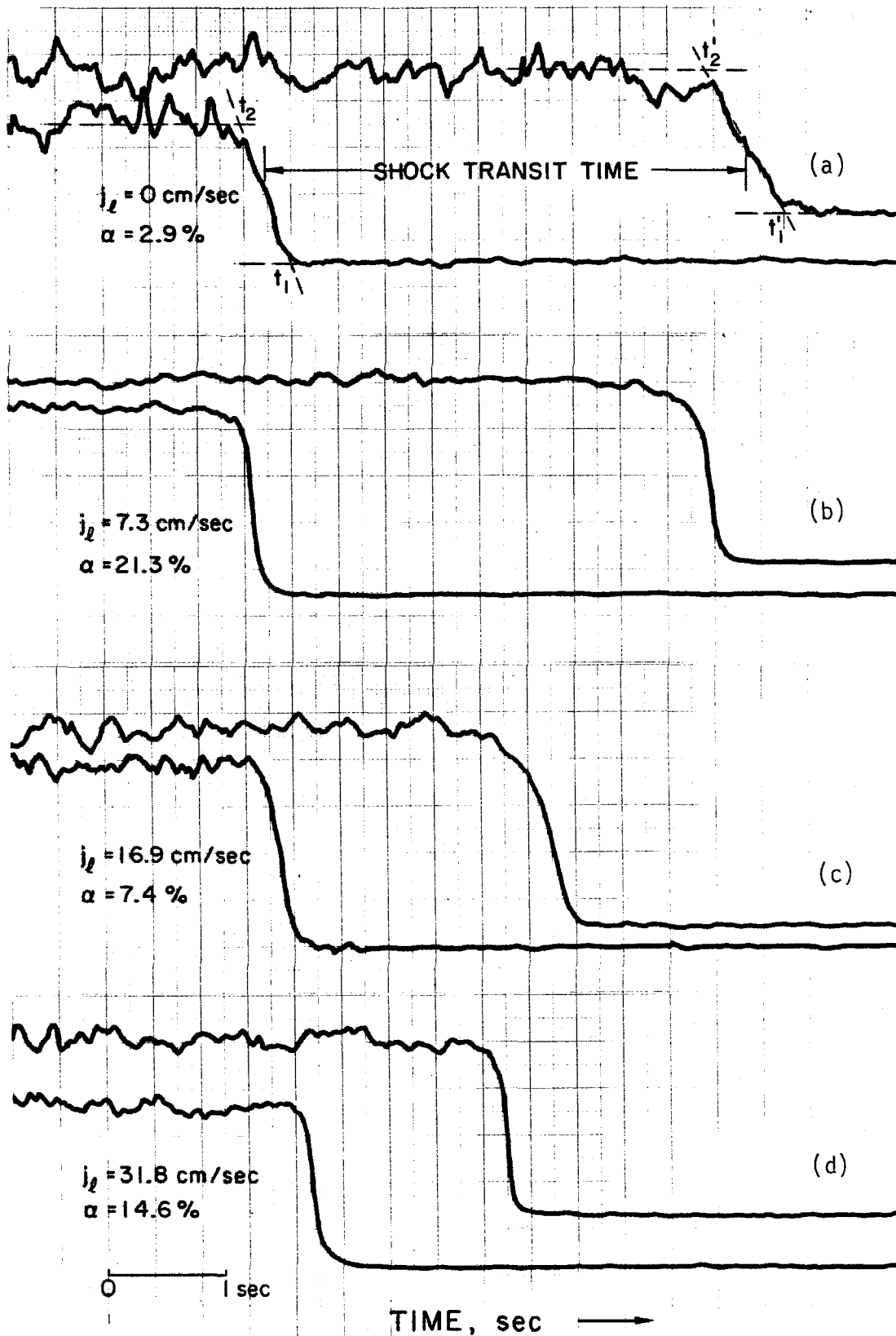
Figure 5.2   Recordings of the void fraction meter outputs showing the
a,b,c,d   voltage drop due to the passage of the kinematic shock. The
              shock is first detected by the upstream meter which corresponds
              to the lower trace. The void fraction below the shock is zero.
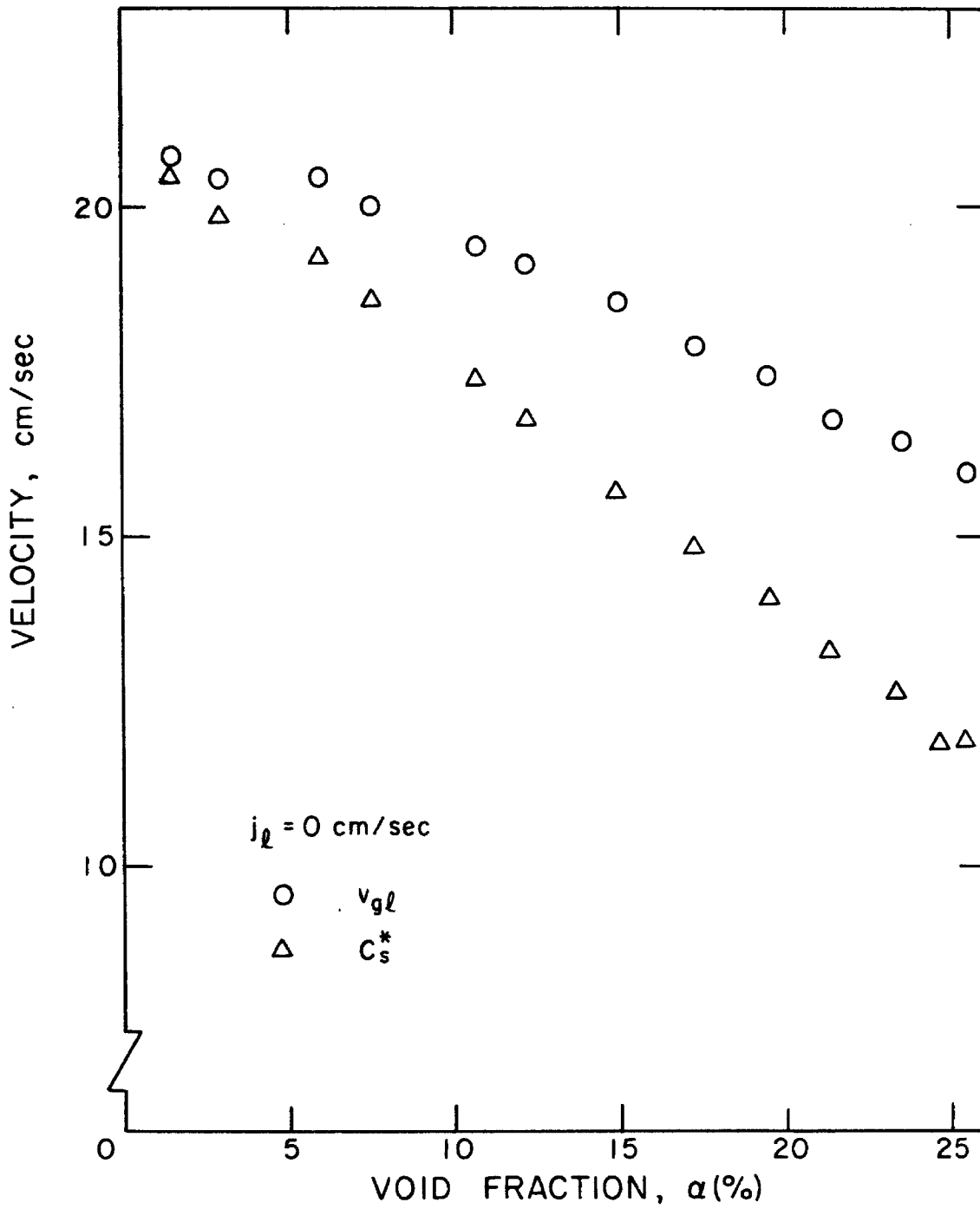
Figure 5.3   Kinematic shocks propagation speed, C*s, and relative velocity of the disperse phase, $V_{g\ell}$ in stagnant water. The void fraction below the shock is zero.
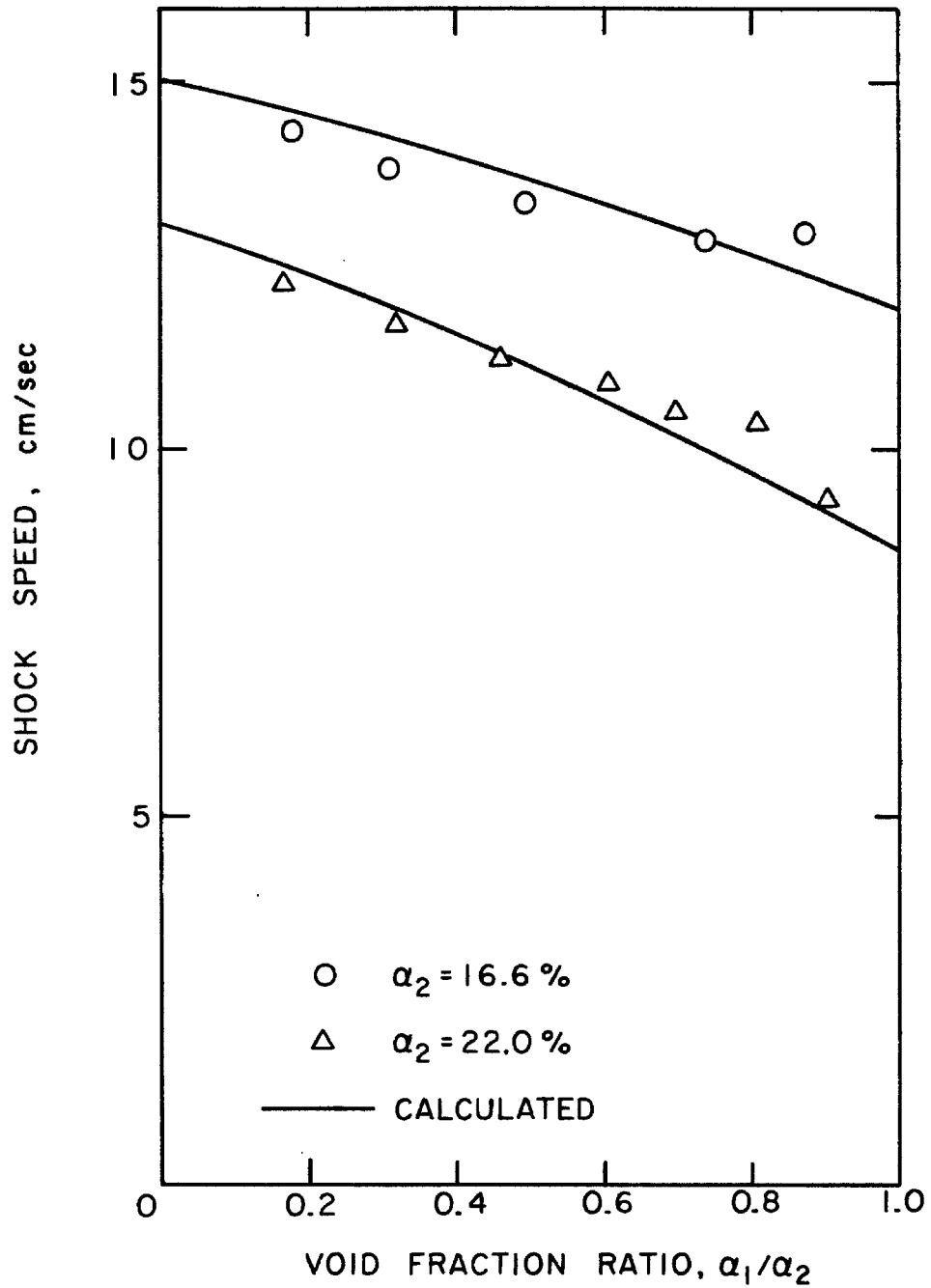
Figure 5.4   Propagation speed $C**s$ of kinematic shocks of decreasing
              strength in stagnant water. The void fractions above and
              below the discontinuity are respectively α_2 and α_1.
              Shown as solid lines are the speeds calculated using Eq.5.30
              and the kinematic shock speed data shown in Fig.5.3.
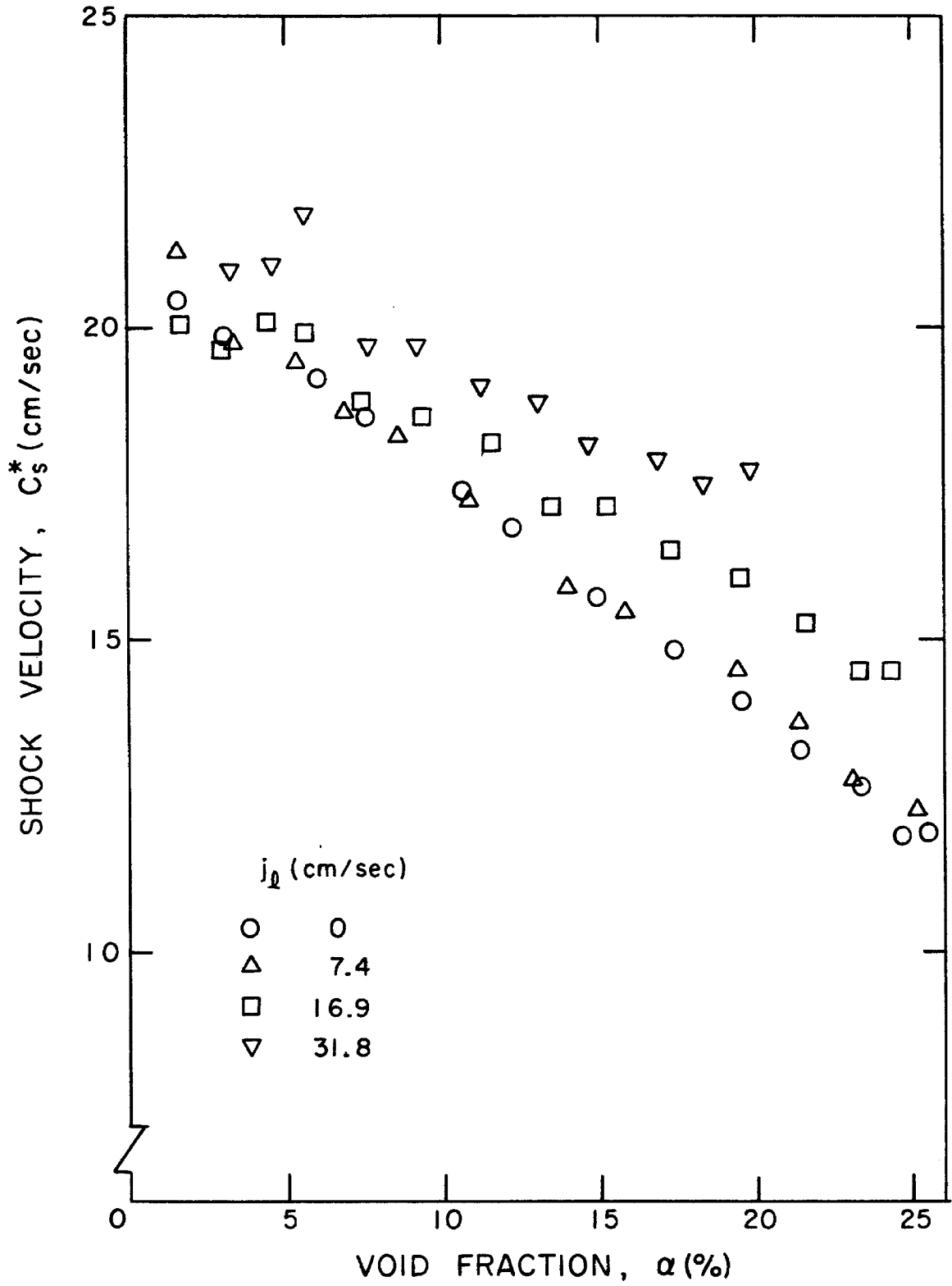
Figure 5.5   Kinematic shock propagation speed, C*s, relative to the liquid
velocity below the shock for various water volumetric fluxes.
The void fraction below the shock is zero.
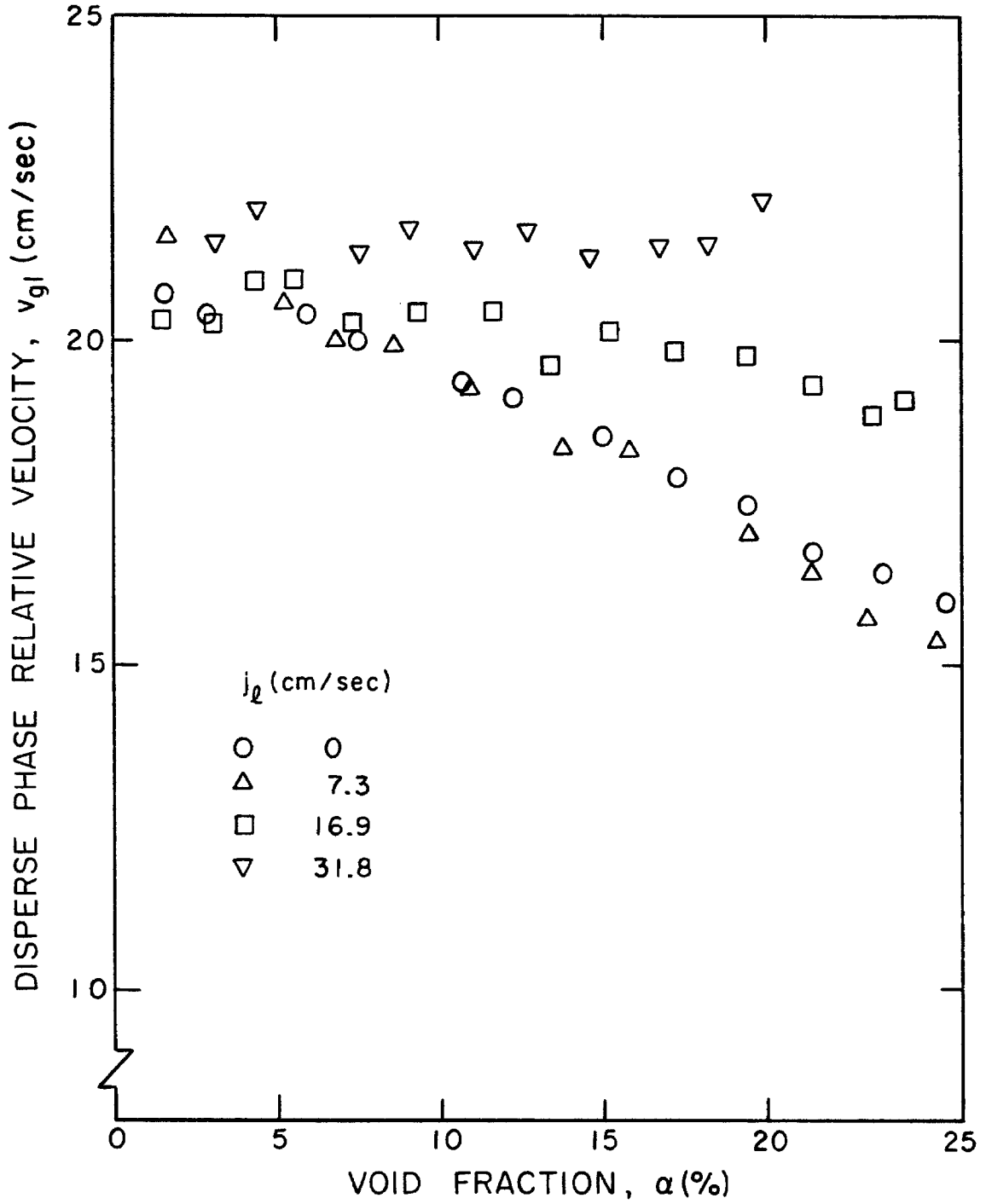
Figure 5.6   Relative velocity of the disperse phase, $v_{g\ell}$, obtained from measurements of the kinematic shock propagation speed.
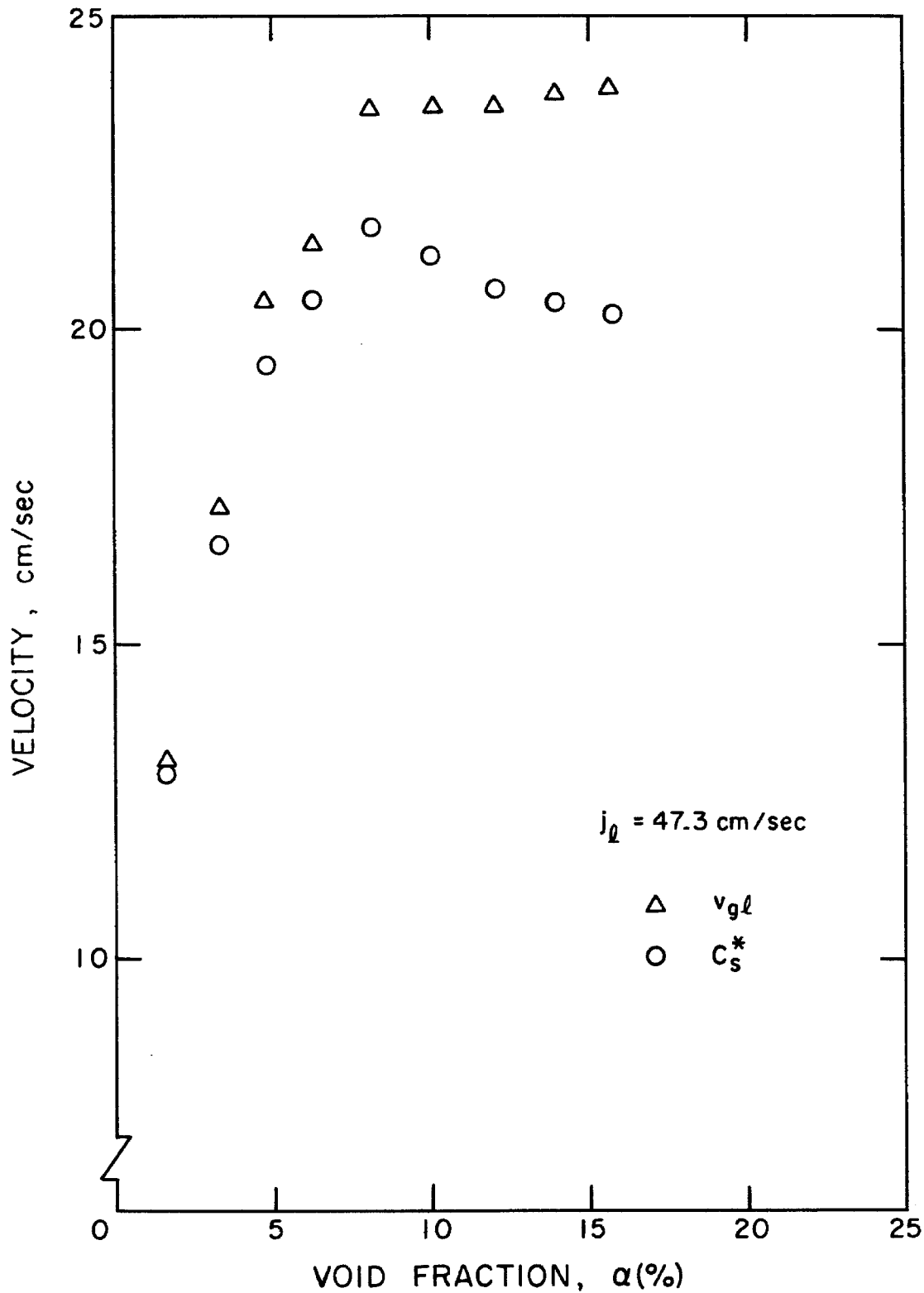
Figure 5.7   Kinematic shock velocity $C*_s$ relative to the liquid velocity below the shock. Also shown is the relative velocity of the disperse phase obtained from these measurements.
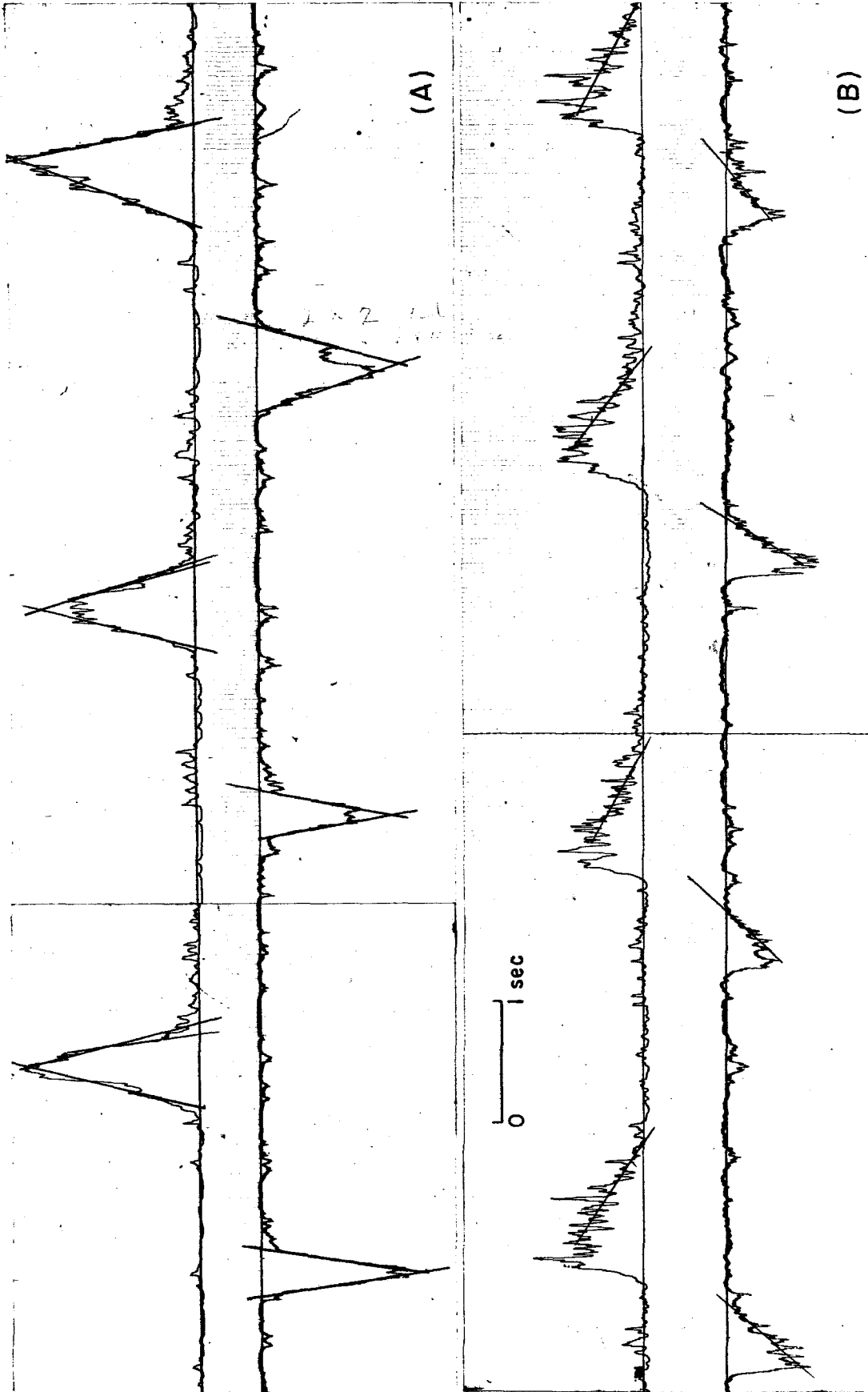
Figure 5.8 Strip chart recordings of void fraction pulses with a peak value less than 2%. The pulse is first detected by the upstream void fraction meter corresponding to the lower trace. The pulses were fitted with straight lines to calculate the propagation velocity. The pulse velocities are: (a) 29.8 cm/s (b) 68.1 cm/s. The distance separating the electrodes is 73 cm.
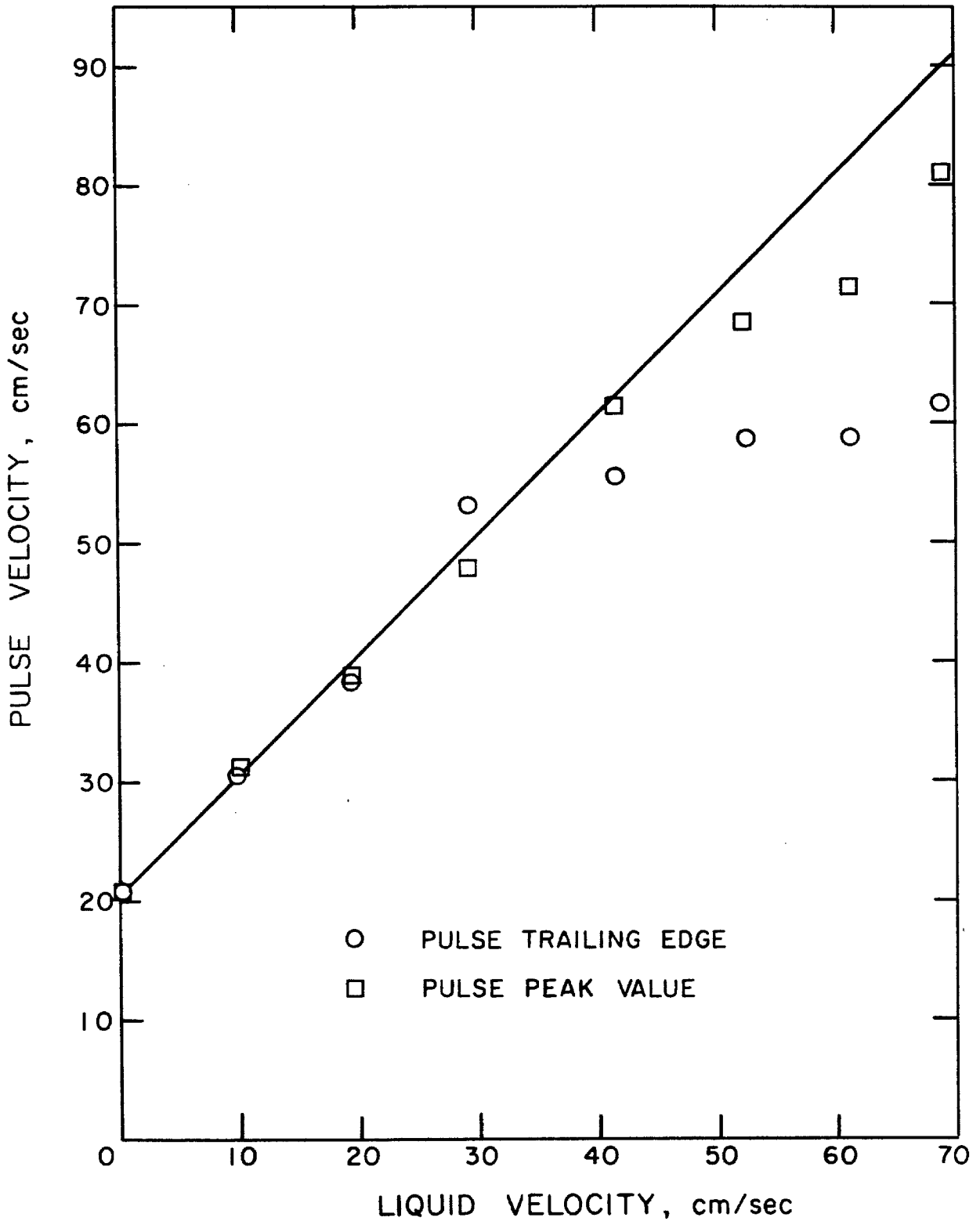
Figure 5.9   Propagation speed of the pulse as a function of the liquid
velocity. Data shown as circles and squares were evaluated
respectively by measuring the transit time interval from the
pulse trailing edges and from the pulse peak values. The
solid line indicated the speed of the pulses extrapolated
from the measurement at zero water velocity.
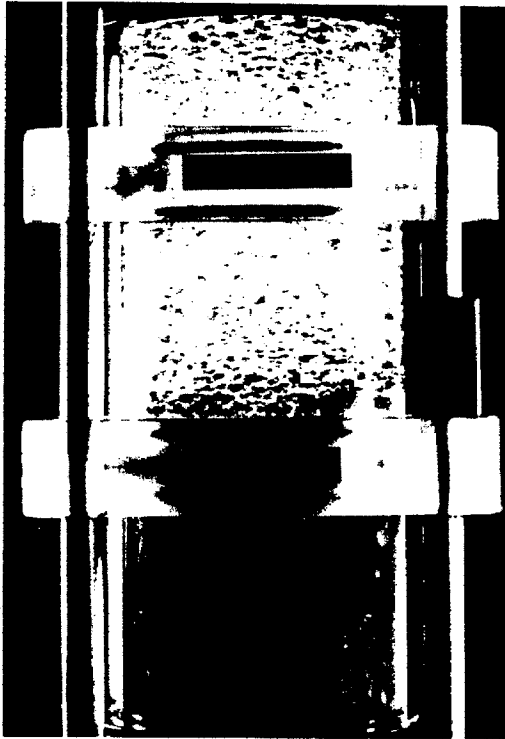
$\alpha = 12.3\%$ $j_\ell = 7.3\,cm/sec$ $\alpha = 11.7\%$ $j_\ell = 31.8\,cm/sec$
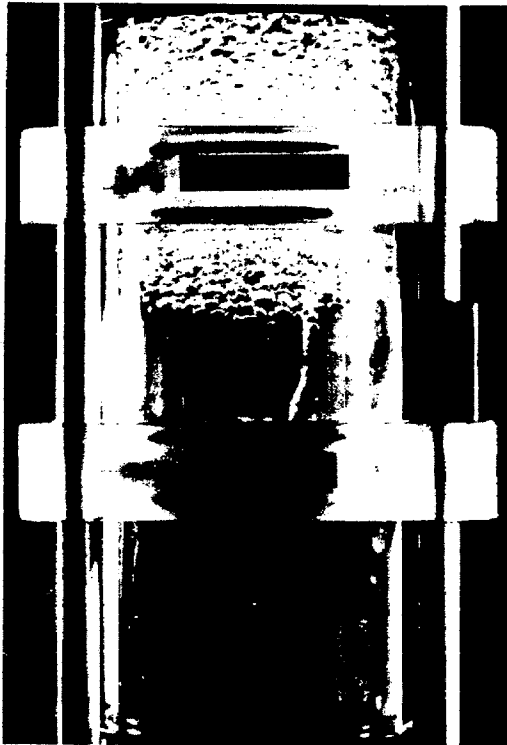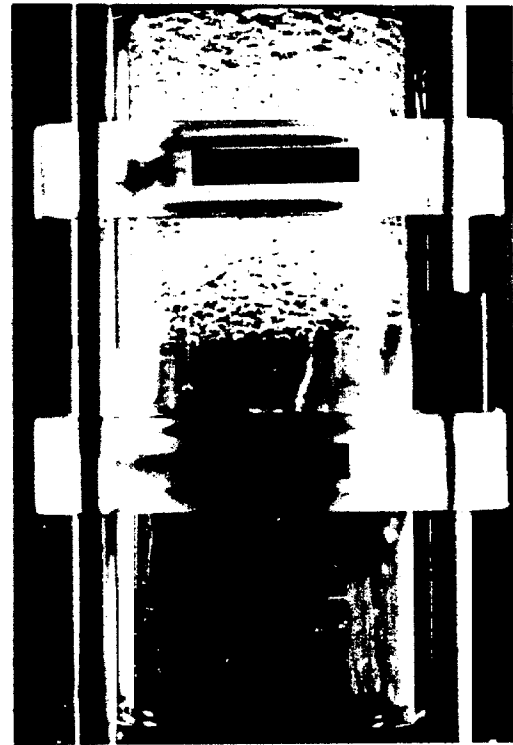
$\alpha = 21.3\%$ $j_\ell = 7.3\,cm/sec$ $\alpha = 20.1\%$ $j_\ell = 16.9\,cm/sec$

FIG.5.10   Photographs of kinematic shocks in air-water bubbly mixtures.
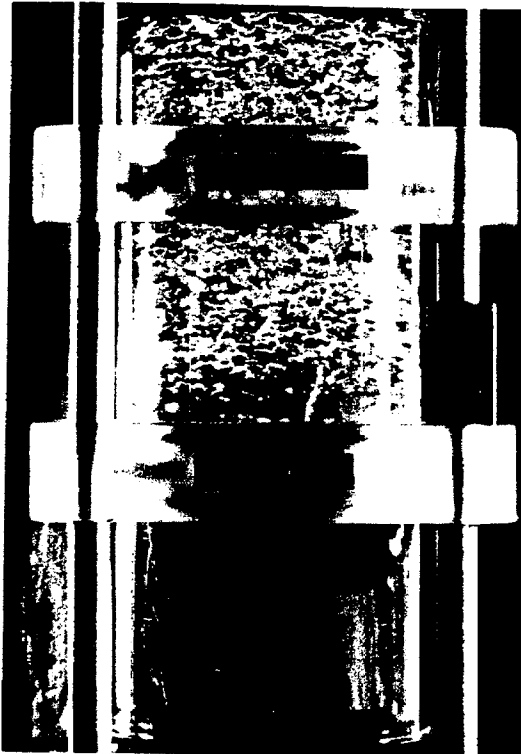
$\alpha = 6.1\%$ $j_\ell = 0$ cm/sec $\alpha = 4.7\%$ $j_\ell = 31.8$ cm/sec
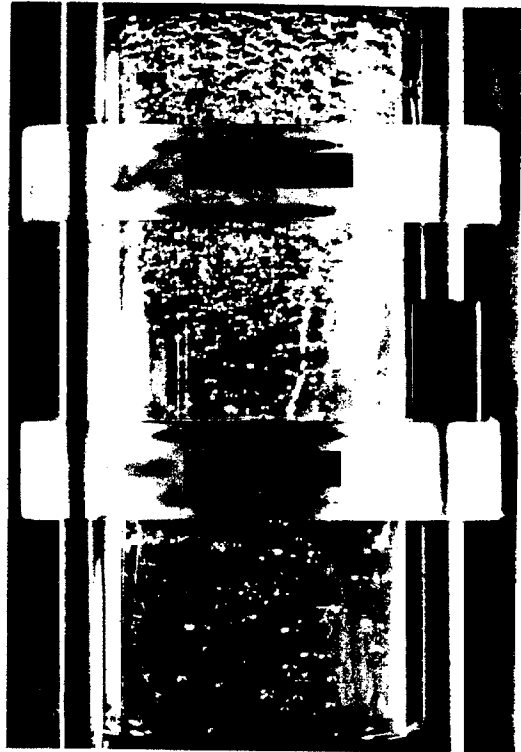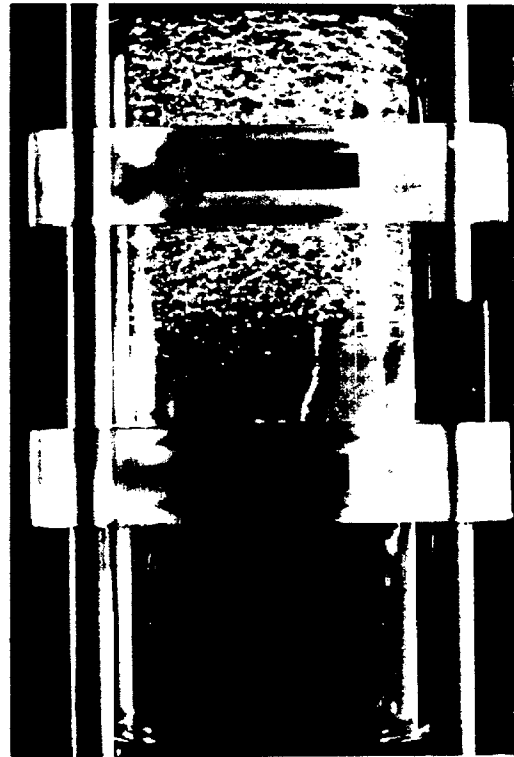
$\alpha = 1.9\%$ $j_\ell = 16.9$ cm/sec $\alpha = 8.7\%$ $j_\ell = 0$ cm/sec

FIG.5.11   Photographs of kinematic shocks in air-water bubbly mixtures.
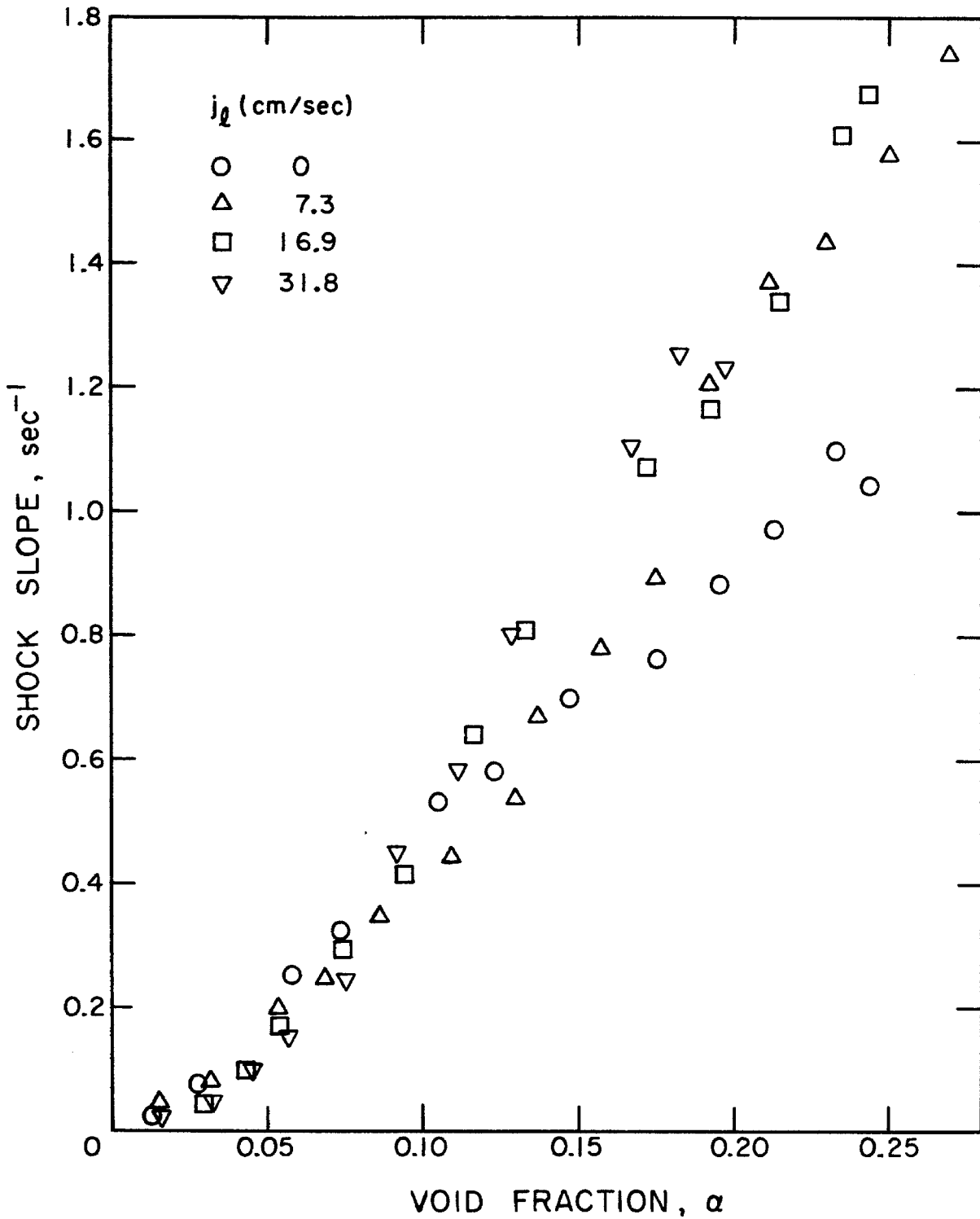
Figure 5.12   Measurements of the shock slopes for different water volu-
metric fluxes. These slopes were obtained from the strip
chart recordings of the upstream void fraction meter. The
void fraction below the shock is zero.
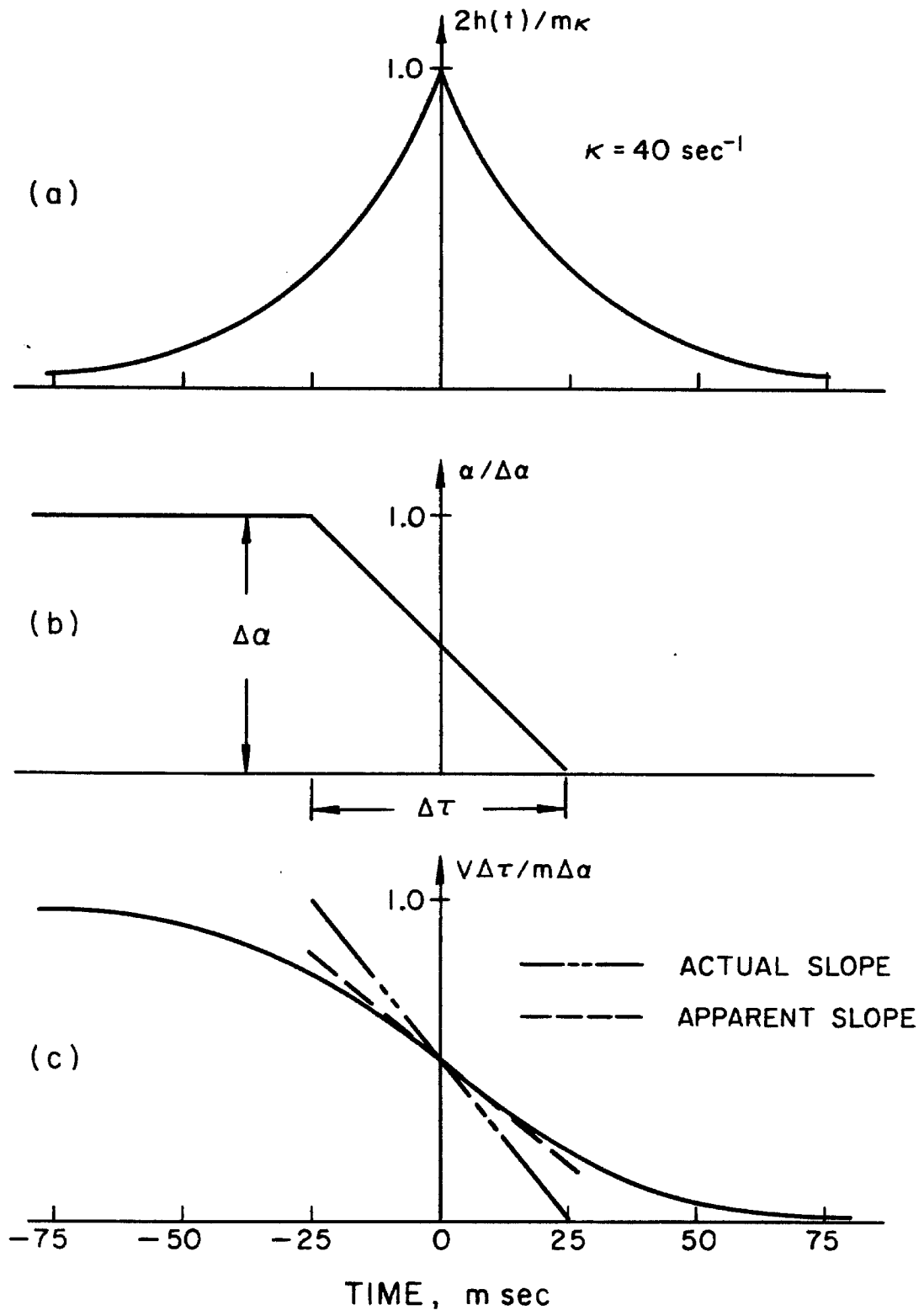
Figure 5.13 Illustration of the procedure used to correct the measured slope for the filtering effect: (a) filter function, (b) hypothetical wave before filtering with slope $\Delta\alpha/\Delta\tau$ (c) response of the void fraction meter; the apparent slope shown as a dotted line corresponds to the slope measured on the strip chart recordings while the other line is the actual slope before filtering.
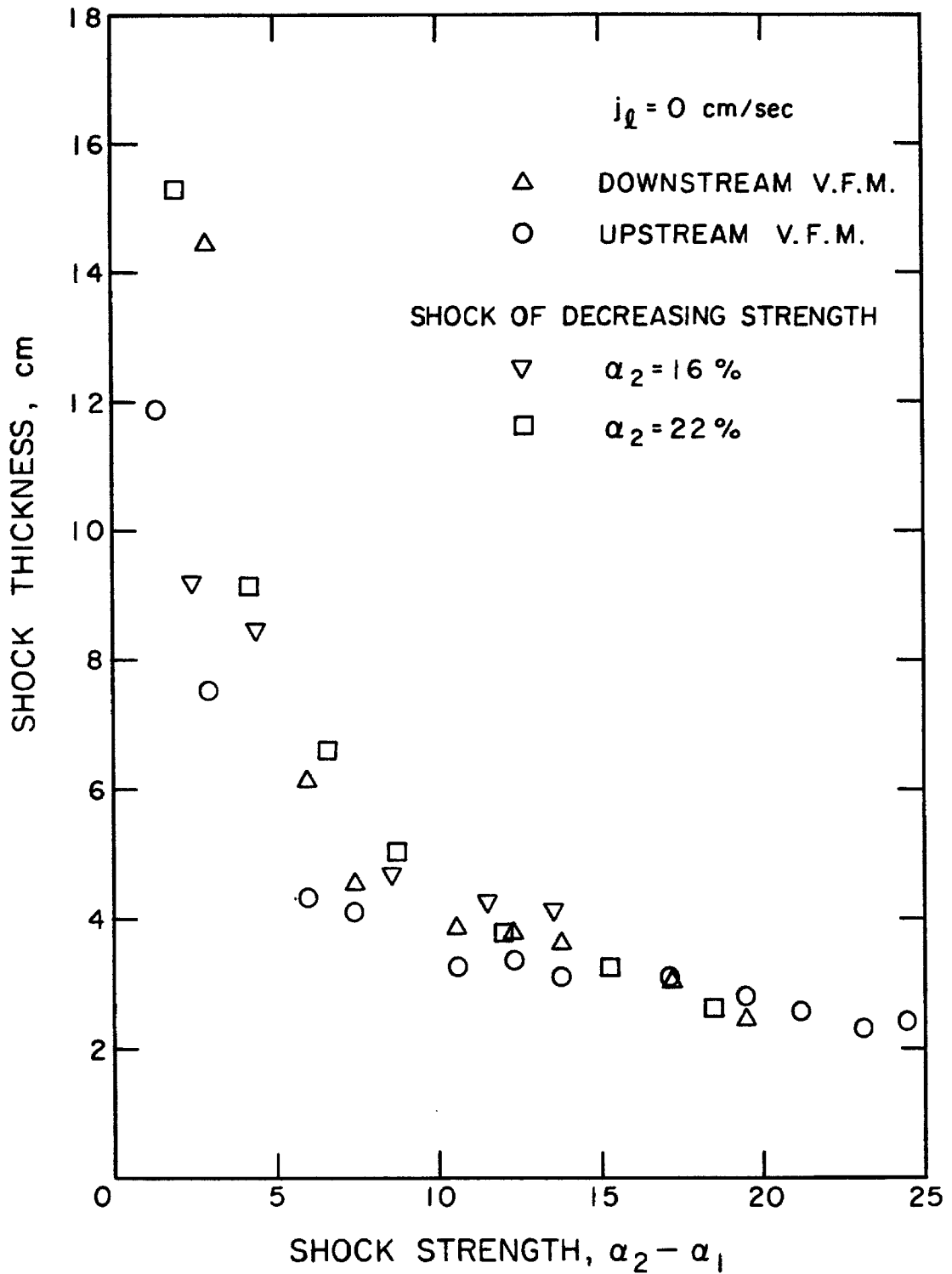
Figure 5.14   Shock thickness as a function of the shock strength. The
water volumetric flux below the shock is zero. Data shown
as circles and triangles correspond to a void fraction,
α_1, below the shock equal to zero. Also shown as squares
and inverted triangles are shock thicknesses for which α_1,
is different from zero.
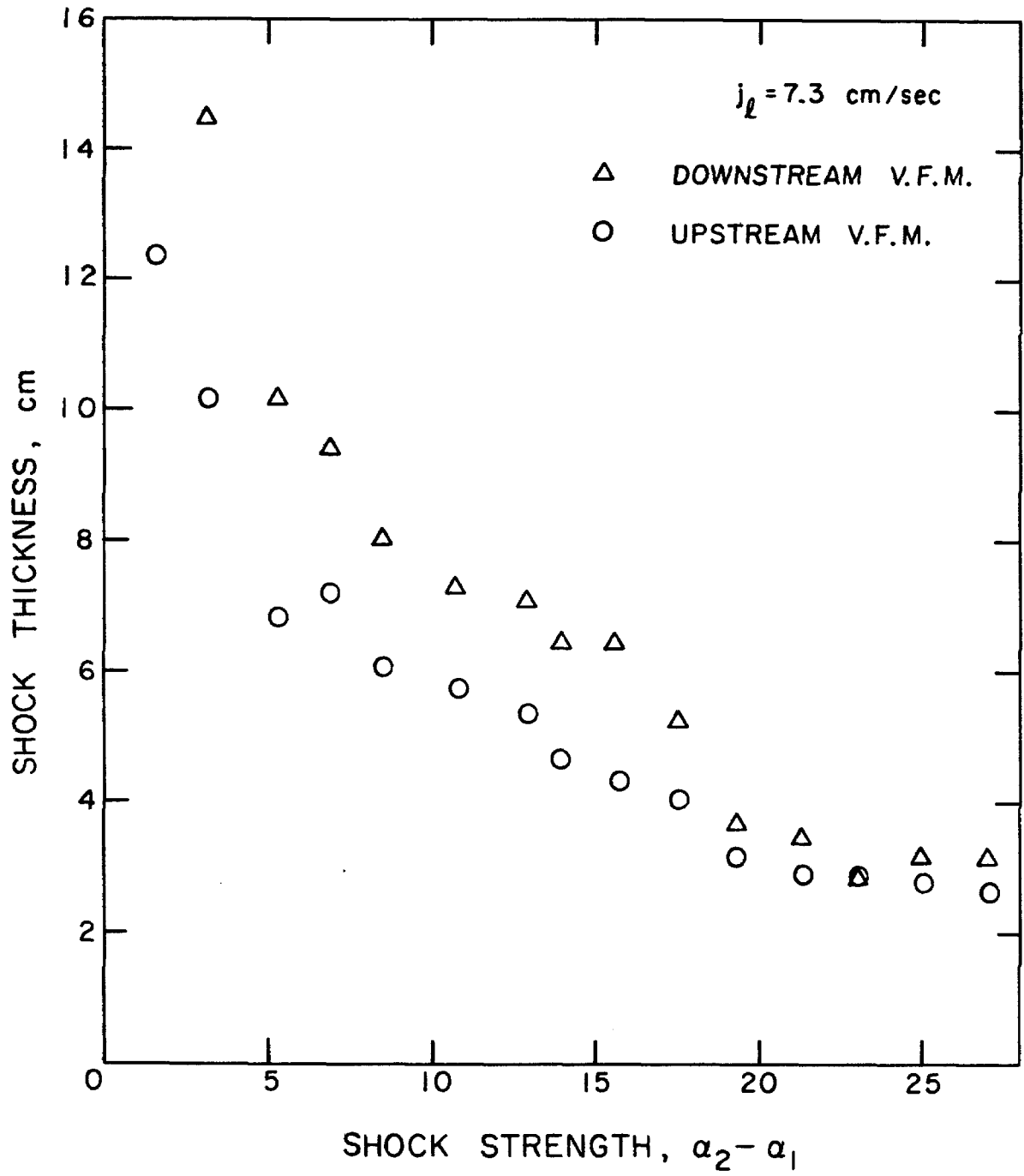
Figure 5.15   Shock thickness as a function of the shock strength; $\alpha_1 = 0$, $j_\ell = 7.3$ cm/s.
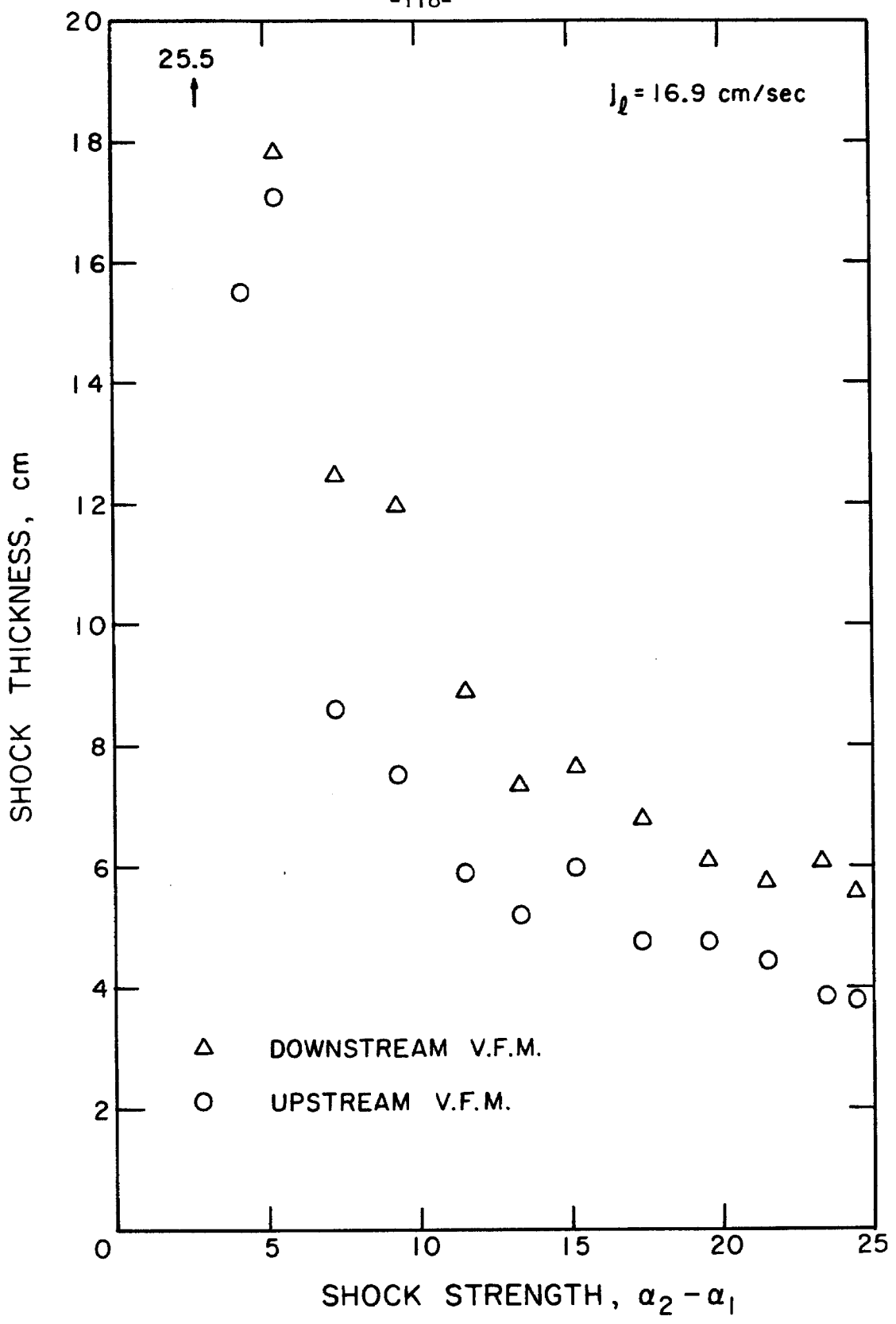
Figure 5.16   Shock thickness as a function of the shock strength; $\alpha_1 = 0$, $j_\ell = 16.9$ cm/s.
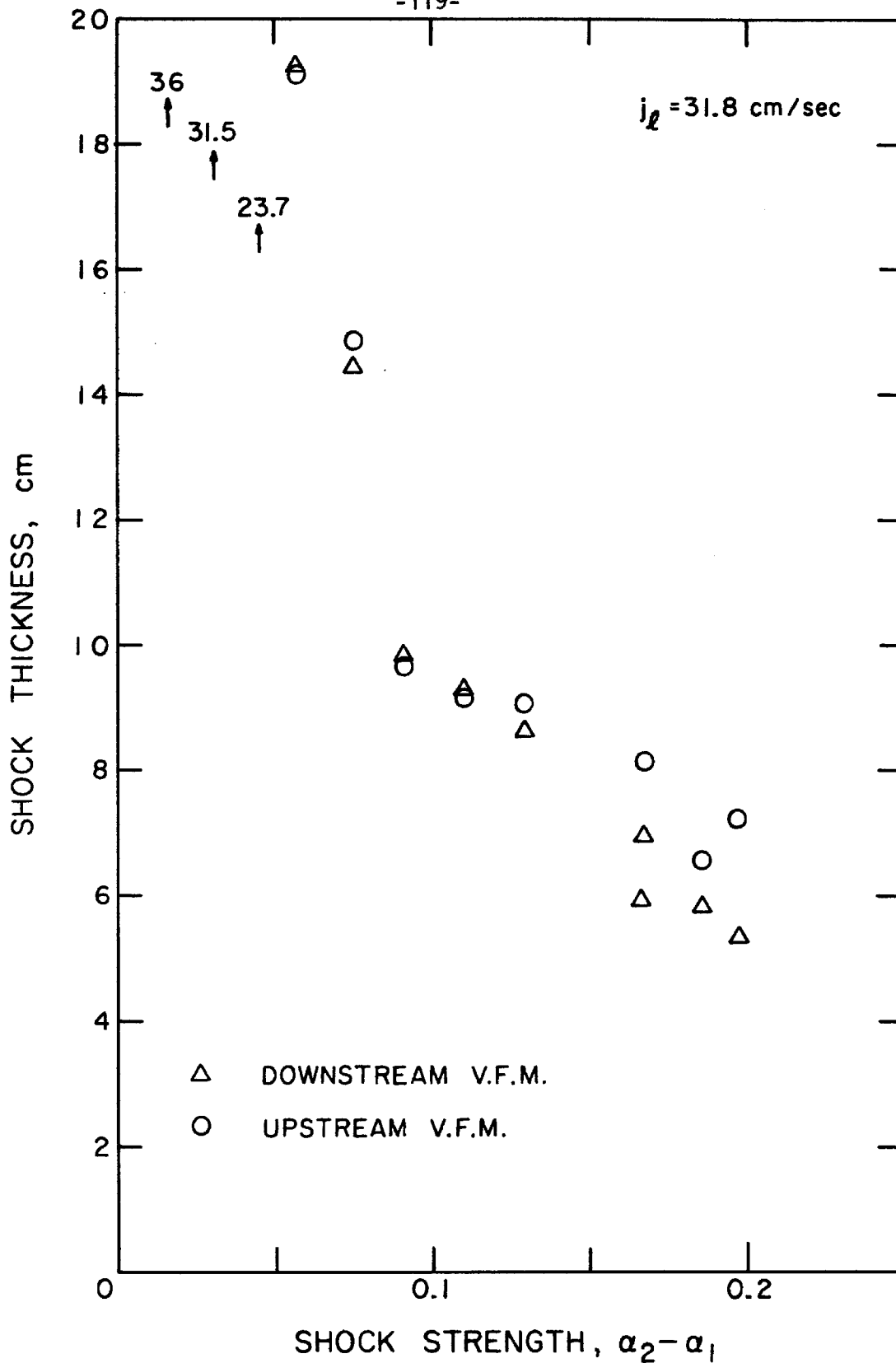
Figure 5.17   Shock thickness as a function of the shock strength;
$\alpha_1 = 0$, $j_\ell = 31.8$ cm/s.

VI. VOID FRACTION METER CROSS-CORRELATION IN STEADY BUBBLY FLOWS

6.1 Introduction

Some authors (Cimorelli and Evangelisti [10], Garrard and Ledwidge [16] for instance) have claimed that the average speed of the disperse phase in a steady bubbly flow can be determined by cross-correlation of the fluctuating voltages of two void fraction meters separated by a known distance. It is our intention to show that this technique does not measure the average gas speed velocity. We will show that a natural system of kinematic waves is at every time present in a steady bubbly flow, and that such cross-correlation measures the propagation speed of these waves.

6.2 Cross-Correlation Function

The randomness of the signal fluctuations in an air-water bubbly mixture does not rule out the existence of a structure propagating in a Lagrangian sense. The transport time of this structure can be measured by cross-correlation of the outputs of two void fraction meters. If $\tilde{V}_1(t)$ and $\tilde{V}_2(t)$ are the fluctuating voltages of the two void fraction meters, the cross-correlation function for stationary processes is given by

$$R_{\tilde{V}_1 \tilde{V}_2}(\tau) = \lim_{T \to \infty} \left\{ \frac{1}{T} \int_0^T \tilde{V}_1(t)\, \tilde{V}_2(t+\tau)\, dt \right\} \, . \tag{6.1}$$

The maximum value of $R_{\tilde{V}_1 \tilde{V}_2}(\tau)$ is achieved when the time delay τ

corresponds to the transport time of the structure. The quality of
the common information is assessed by a normalized form, $\Phi_{\tilde{V}_1\tilde{V}_2}(\tau)$, of
the cross correlation function. $R_{\tilde{V}_1\tilde{V}_2}(0)$ and $R_{\tilde{V}_2\tilde{V}_2}(0)$ being the mean
square value of the noise of each signal, $\Phi_{\tilde{V}_1\tilde{V}_2}(\tau)$ is defined as

$$\Phi_{\tilde{V}_1\tilde{V}_2}(\tau) = \frac{R_{\tilde{V}_1\tilde{V}_2}(\tau)}{[R_{\tilde{V}_1\tilde{V}_1}(0) \cdot R_{\tilde{V}_2\tilde{V}_2}(0)]^{1/2}} \qquad (6.2)$$

and $|\Phi_{\tilde{V}_1\tilde{V}_2}(\tau)|$ takes a value between zero and one.

6.3 Meaning of the Speed Measured by Cross-Correlation

Cross-correlograms of the fluctuating voltages of two void fraction meters were obtained on the digital signal processor for a steady bubbly flow mixture. The electrode system of two meters was aligned vertically a distance 10.8 cm apart in the middle of the test section. The cross correlograms were determined from a 40 second real time recording.

A selection of cross-correlograms is presented in Fig. 6.1 for various void fraction and water volumetric fluxes ranging from 0 to 31.8 cm/s. It can be seen that there is a maximum in the cross correlogram. The time τ^* at which this maximum occurs can be used to calculate the absolute velocity of the propagating bubbly structure. Figure 6.2 shows a summary of the absolute speed of the structure, v_s, as a function of the void fraction for constant water fluxes. To compare with the data obtained in the preceding chapter, the relative velocity, $v_{s\ell}$, of the structure with respect to the average liquid velocity was calculated according to the following expression

$$V_{s\ell} = V_s - \frac{j_\ell}{[1 - \alpha]} \qquad\qquad (6.3)$$

where j_ℓ is the water volumetric flux. The velocity of the disperse phase relative to the liquid, $v_{g\ell}$, (as given by Fig. 5.6 of the previous chapter) and the relative velocity of the structure, $v_{s\ell}$, are plotted both as functions of the void fraction in Figs. 6.3, 6.4, 6.5 and 6.6 for the water fluxes investigated. Although some scatter is observed in the $v_{s\ell}$ data, it is clear that it does not correspond to the relative velocity of the disperse gaseous phase; the latter being significantly larger.

The meaning of the velocities measured by cross-correlation has to be explained in terms of the kinematic wave theory described in Chapter V. The $v_{s\ell}$ data were compared to the relative infinitesimal wave speed C_i^* as defined by Eq.(5.27) and calculated from the data on kinematic shocks obtained previously. The results are shown as solid lines in Figs. 6.3 through 6.6. The agreement between $v_{s\ell}$ and C_i^* is very good and even remarkable in the case where j_ℓ is equal to 16.9 cm/s. This comparison leads us to the conclusion that $v_{s\ell}$ is the infinitesimal kinematic wave speed. The structure detected therefore appears to be a small amplitude kinematic wave.

The consequences of these results are important. They constitute a good verification of the kinematic wave theory and add weight to the evidence already reported in Section 5.3.3 for shocks of decreasing strength between regions of constant void fraction. They also clearly show that the cross-correlation technique in a steady bubbly flow does not measure the velocity of the disperse phase, but rather its

infinitesimal wave speed. The difference between the two speeds is small at low void fractions, but not negligible at large void fractions and moderate velocities of the liquid phase. From the infinitesimal wave speed it is <u>not</u> possible to calculate the velocity of the disperse phase unless the latter is independent of the void fraction.

6.4 Natural System of Kinematic Waves in Steady Bubbly Flows

The transport time of the bubbly structure will decrease with an increase in the water flow rate. Figure 6.7 shows a summary of the normalized cross correlation maxima $\Phi_{\tilde{V}_1 \tilde{V}_2}(\tau^*)$ plotted as a function of the corresponding transport time τ^*. In spite of the extensive scatter of the data, this figure offers a clear picture of the time history of the propagating structure. As time progresses, the structure is losing its identity. We conclude that, within a nominally steady bubbly flow, small amplitude kinematic waves are created and destroyed on a continuous basis. Moreover, because the flow is steady, the time average gas transport associated with these structures is zero.

6.5 Non-Dispersive Kinematic Waves

The propagating structure is made of disturbances having a wide range of frequencies. Symington [43] has shown that two sets of kinematic waves are present when the bubble inertia is not neglected. Both sets are frequency dispersive waves. However, the first set is damped within a few bubble diameters. The question therefore arises as to whether the structural decay is due to the dispersive nature of the waves.

The cross-spectral density $S_{\tilde{V}_1\tilde{V}_2}(\omega)$ of the fluctuating output voltages can provide information on this point. The cross-correlation is the inverse Fourier transform of the cross spectral density

$$R_{\tilde{V}_1\tilde{V}_2}(\tau) = \frac{1}{2\pi} \int_{-\infty}^{+\infty} S_{\tilde{V}_1\tilde{V}_2}(\omega) \, e^{j\omega\tau} \, d\omega \quad . \tag{6.4}$$

Rewriting the cross-spectral density as

$$S_{\tilde{V}_1\tilde{V}_2}(\omega) = |S_{\tilde{V}_1\tilde{V}_2}(\omega)| e^{j\theta_{\tilde{V}_1\tilde{V}_2}(\omega)} \tag{6.5}$$

with the phase shift $\theta_{\tilde{V}_1\tilde{V}_2}(\omega)$ defined as

$$\theta_{\tilde{V}_1\tilde{V}_2}(\omega) = \tan^{-1}\left\{\frac{\mathrm{Im}[S_{\tilde{V}_1\tilde{V}_2}(\omega)]}{\mathrm{Real}[S_{\tilde{V}_1\tilde{V}_2}(\omega)]}\right\} \tag{6.6}$$

Substituting Eq. (6.5) in (6.4), one gets:

$$R_{\tilde{V}_1\tilde{V}_2}(\tau') = \frac{1}{2\pi} \int_{-\infty}^{+\infty} |S_{\tilde{V}_1\tilde{V}_2}(\omega)| \, e^{j\omega\tau'} \, d\omega$$

where τ' is

$$\tau' = \tau - \frac{\theta_{\tilde{V}_1\tilde{V}_2}(\omega)}{\omega} \quad .$$

Therefore, for a given frequency of the disturbance, the time delay is simply $\theta_{\tilde{V}_1\tilde{V}_2}(\omega) / \omega$. For nondispersive waves this time delay is independent of the frequency, and consequently $\theta_{\tilde{V}_1\tilde{V}_2}(\omega)$ is proportional to ω.

The cross-spectral density modulus of the fluctuating voltages and the corresponding phase shifts were measured on the DSP and are shown in Fig. 6.8 for a void fraction of approximately 2% and an increasing velocity of the water. The cross-spectral density exhibits a trend similar to the frequency spectrum modulus presented in Fig.4.4, indicating that disturbances of small wavelengths have an attenuated output voltage. In the region where the spectral density has a significant amplitude, the phase shift plotted as a function of the frequency clearly indicates that these waves are nondispersive. As the speed of the water increases, the meaningful range of frequencies becomes larger on the cross-spectral density, and nondispersive waves are observed at higher frequencies. This is due to an improving response of the void fraction meter. Disturbances are convected at a faster speed through the volume of influence of the electrodes such that, measured in a laboratory frame, they exhibit higher frequencies. However, in terms of measurable wavelengths, the response of the void fraction meter is not improved (see Chapter III).

Because of the limit on the void fraction wavelength resolution, it is not possible to draw any conclusion for shorter wavelength disturbances which are most likely to show a frequency dispersive behavior. However, we can conclude that the non-dispersive waves are attenuated since the normalized cross-correlograms maxima measured were shown to be less than unity.

6.6 Discussion

We have shown in this chapter that the speed determined by cross-correlating the voltage fluctuations does not yield the average speed of the disperse phase, but rather its infinitesimal wave speed. Consequently, we have deduced that a natural system of kinematic waves is present at all times in a nominally steady bubbly flow. At least for large wavelength disturbances, these waves are nondispersive but are nevertheless diffused.

The mechanisms by which the large wavelengths are dissipated is not well understood. A possible explanation may be drawn from the work of Baker and Chao [2]. They have observed large fluctuations of the instantaneous terminal velocity of the bubbles in the vertical direction. These fluctuations are caused by the lateral motion of the bubbles and the liquid turbulence. Similar observations are reported by Zun [51] in a study on the transverse migration of spherical and nonspherical bubbles. These effects,which are not included in the present kinematic wave equation,are likely to modify significantly the structure of the waves as they propagate.

-127-
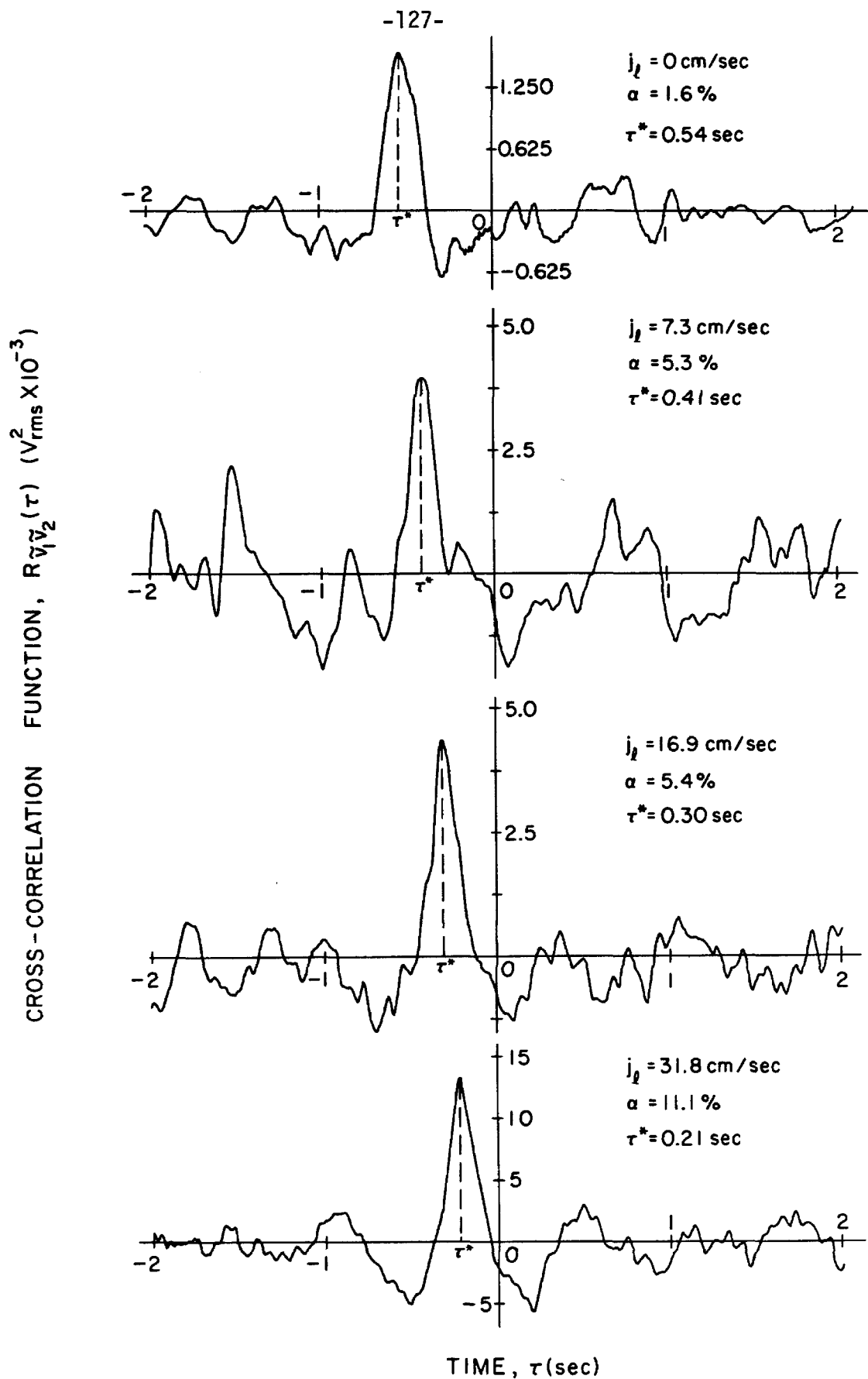
Figure 6.1   Cross-correlograms of the fluctuating voltages in a nominally steady air-water bubbly flow regime.
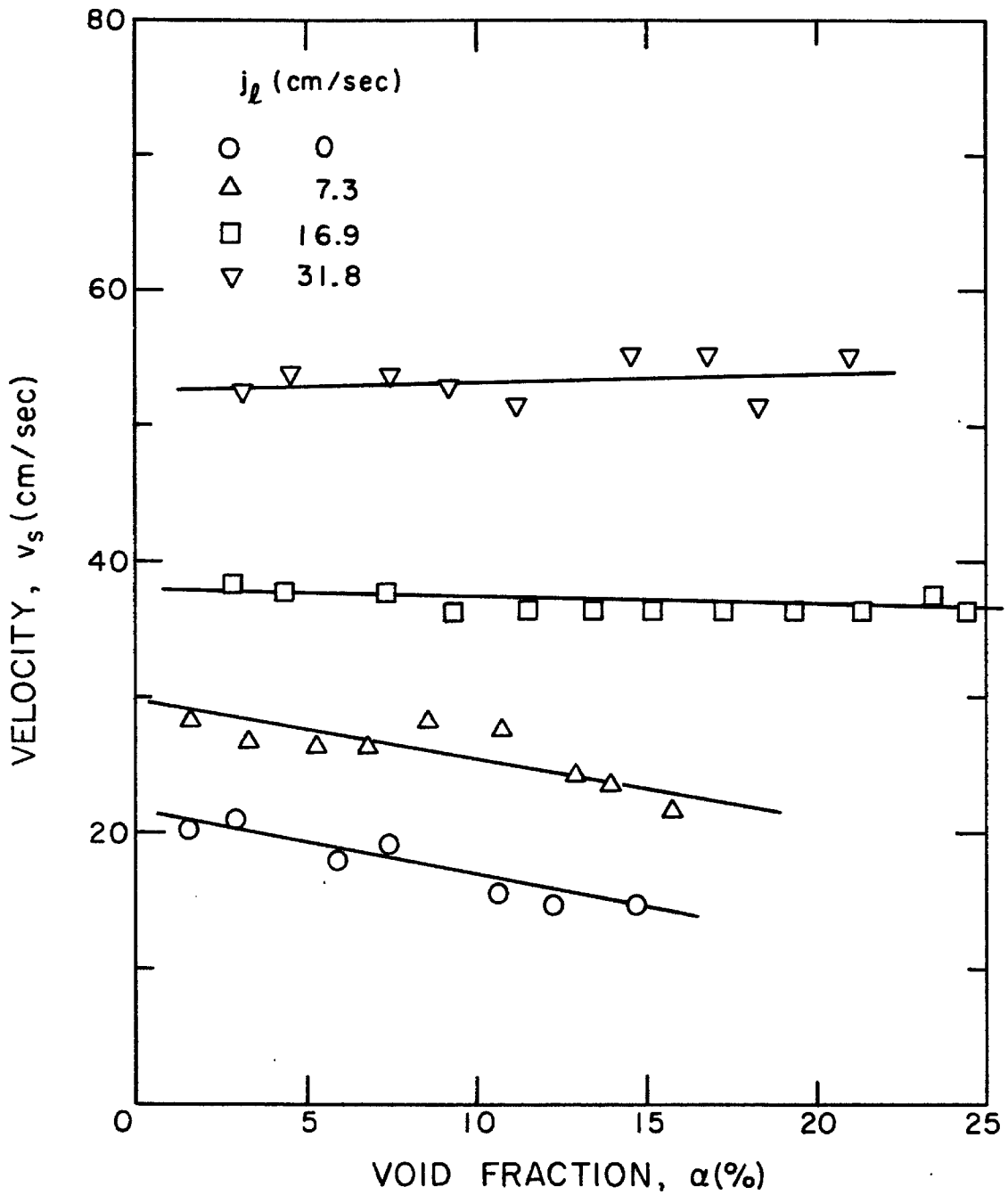
Figure 6. 2   Velocity of the disperse phase structure, v_s, measured by cross-correlation of the void fraction meter fluctuating voltages in a steady air-water bubbly flow regime. The solid lines are to emphasize the data trend as a function of the void fraction for a constant volumetric water flux. The distance separating the two electrode systems is 10.8 cm.

-129-
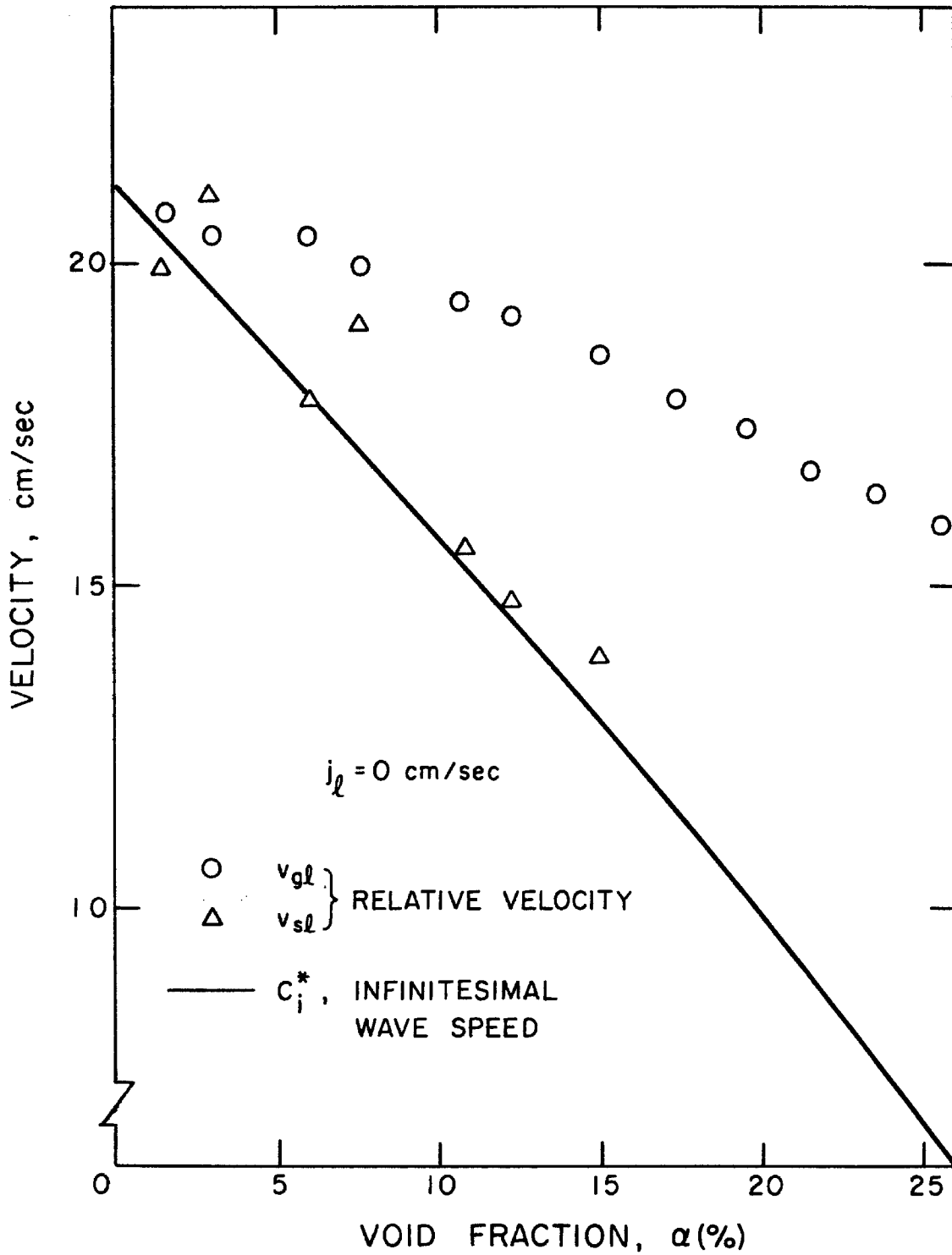
Figure 6.3   Comparison between the disperse phase relative velocity
$v_{g\ell}$, the structure velocity, $v_{s\ell}$, and the infinitesimal wave
speed C_i^* relative to the liquid velocity; $v_{g\ell}$ and C_i^*
are calculated from the kinematic shock propagation speed
data according to Eq.5.25 and Eq.5.27 respectively. These
speeds are also absolute speeds since j_ℓ is equal to zero.
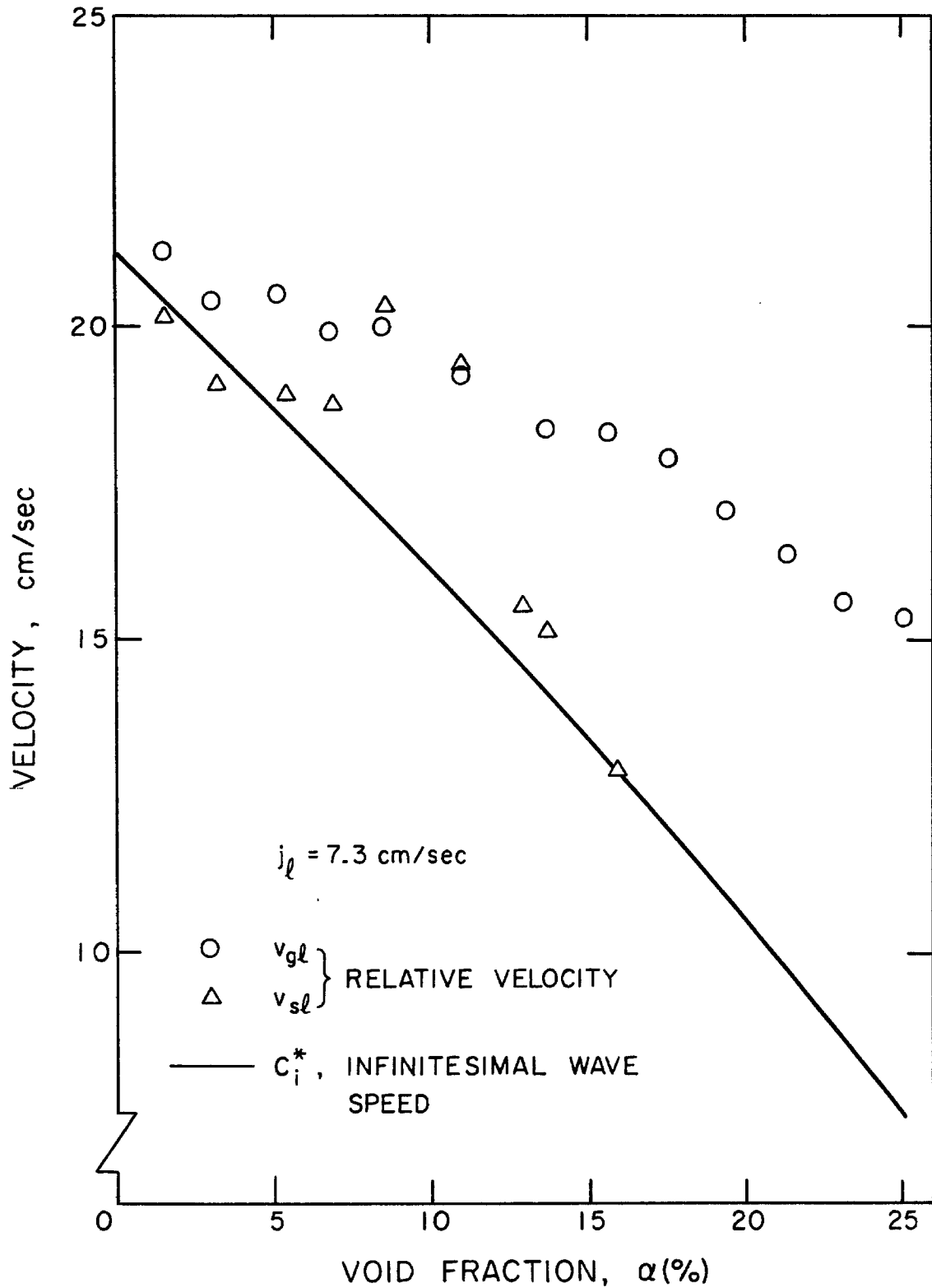
Figure 6.4   Comparison between the relative velocity of the disperse
phase, $v_{g\ell}$, the relative velocity of the structure, $v_{s\ell}$,
and the relative velocity of the infinitesimal wave speed
C_i^*; $j_\ell = 7.3$ cm/s.
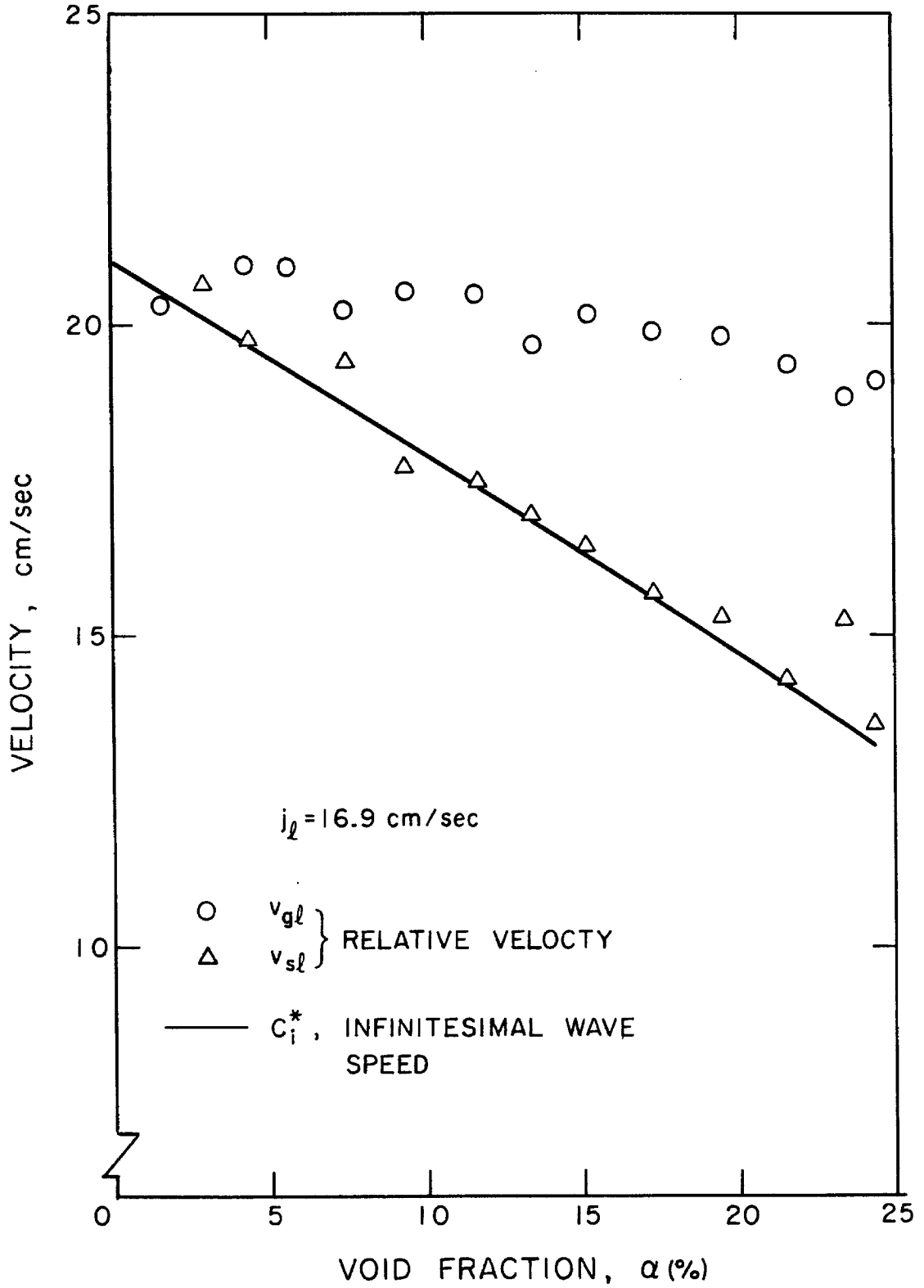
Figure 6.5   Comparison between the relative velocity of the disperse
phase, $v_{g\ell}$, the relative velocity of the structure, $v_{s\ell}$,
and the relative velocity of the infinitesimal wave speed
c_i^* ; j_ℓ = 16.9 cm/s.
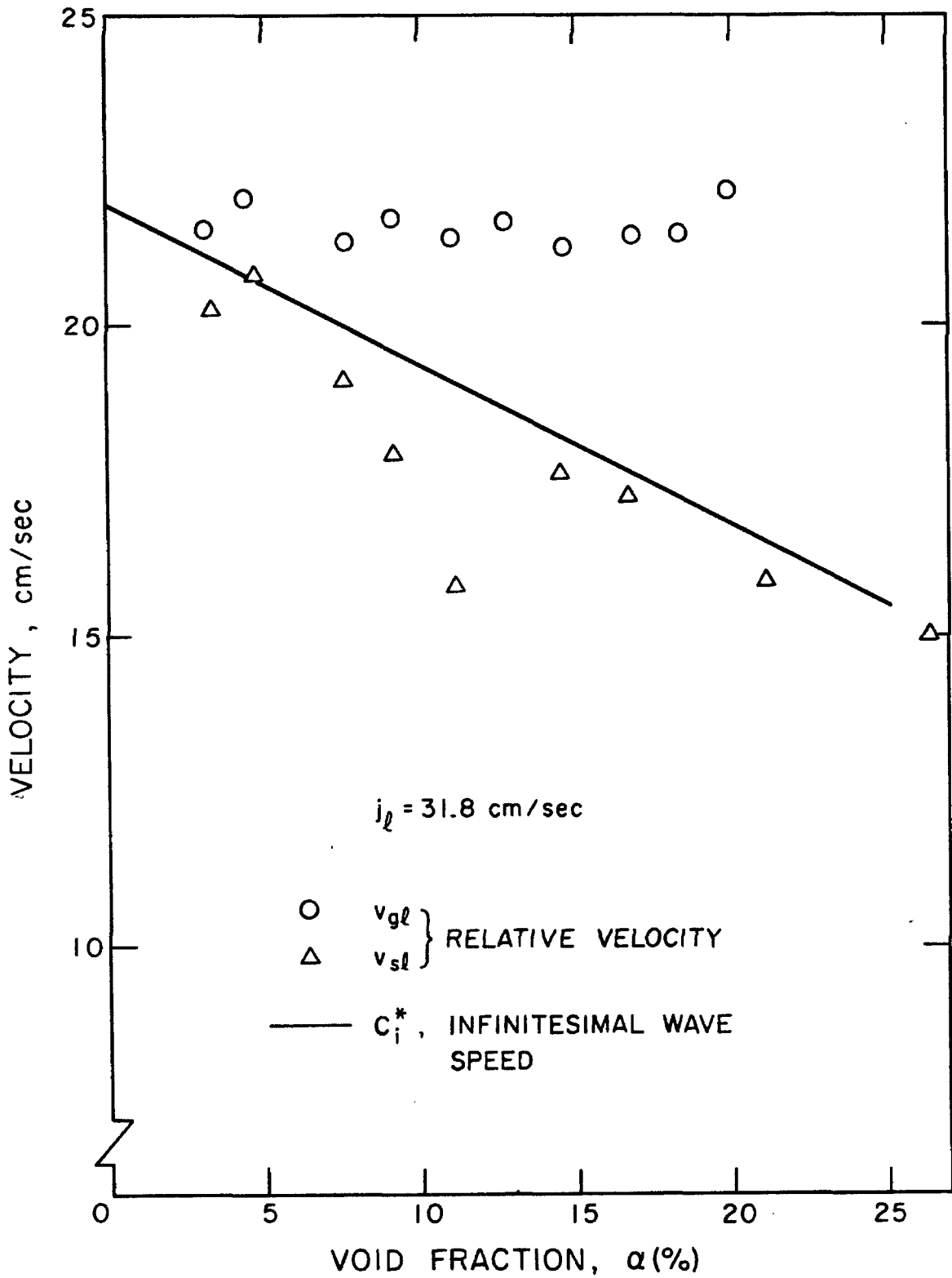
Figure 6.6   Comparison between the relative velocity of the disperse phase, $v_{g\ell}$, the relative velocity of the structure, $v_{s\ell}$, and the relative velocity of the infinitesimal wave speed C_i^*; $j_\ell = 31.8$ cm/s.
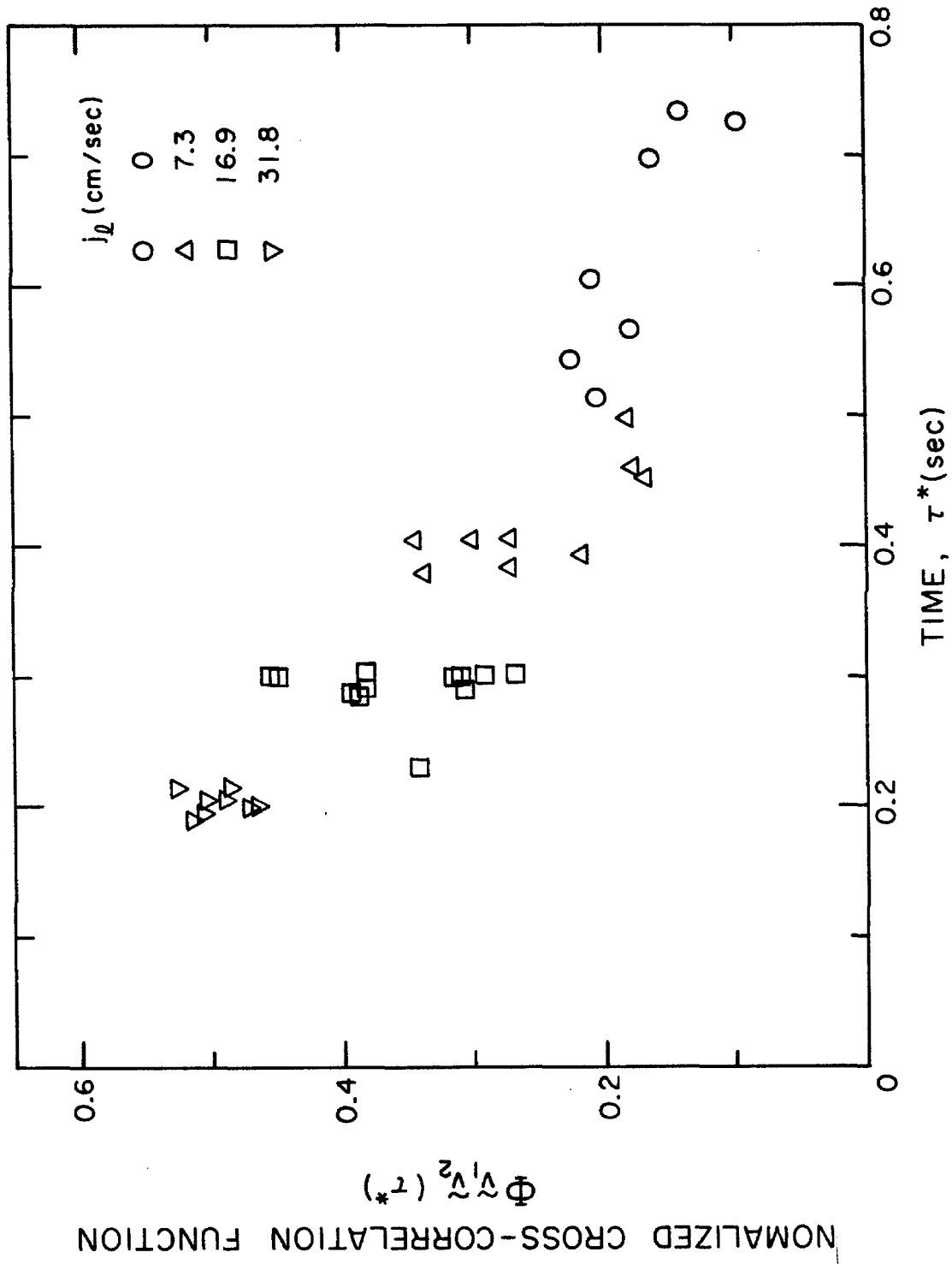
Figure 6.7 Maxima of the normalized cross-correlation function measured in a steady air-water bubbly flow regime as a function of the time delay τ^*. The distance between the center of the two electrode systems is 10.8 cm for each water volumetric flux considered.
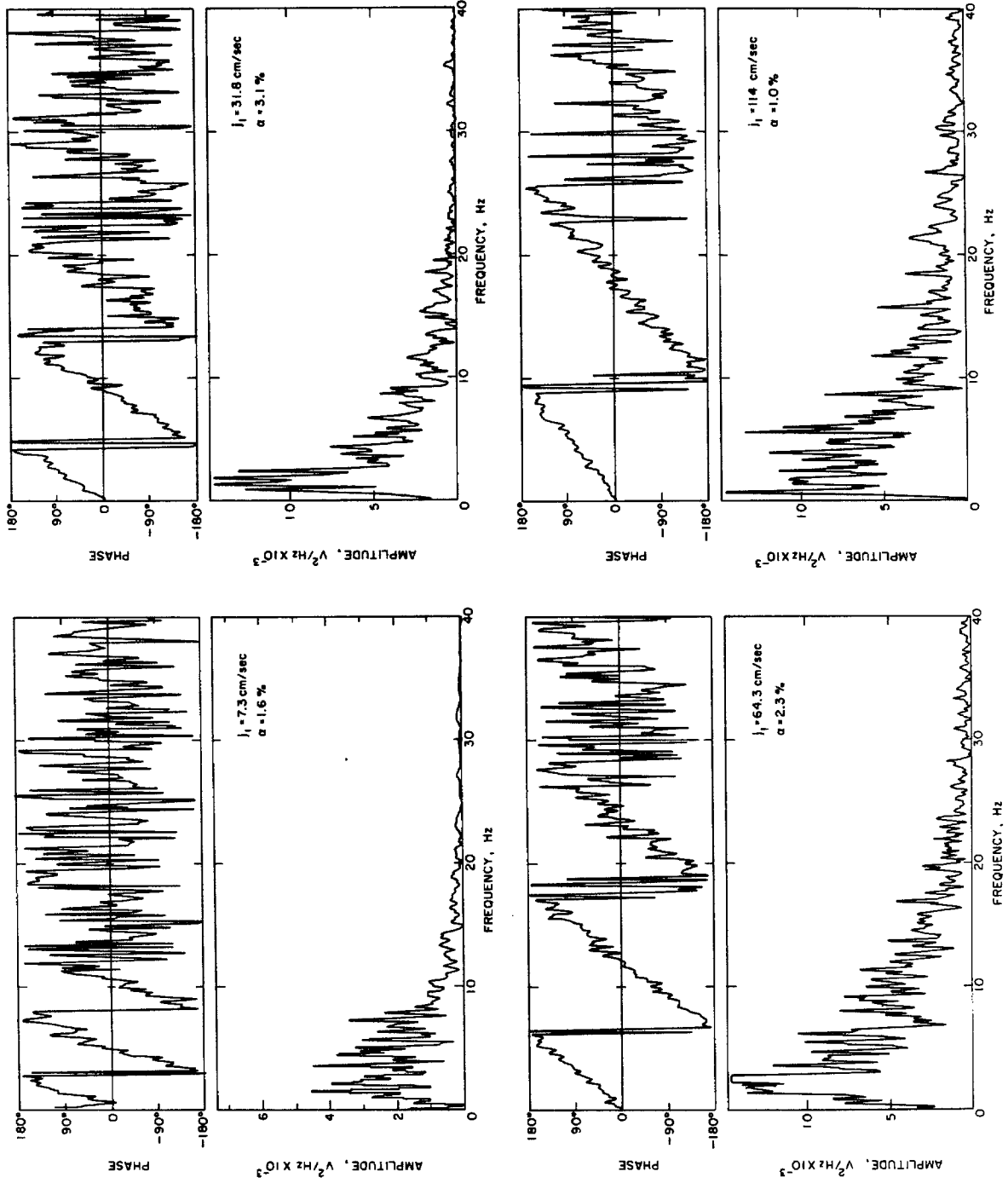
Figure 6.8 Cross-spectral power density amplitude and phase of the void fraction fluctuating voltages in a steady air-water bubbly flow regime showing the nondispersive nature of the infinitesimal wave speed.

VII. SUMMARY AND CONCLUSIONS

One of the aims of this thesis has been to contribute to the development of two-phase flow instrumentation capable of a good dynamic response. The transverse field electromagnetic flowmeter was investigated both analytically for disperse and annular flow regimes and experimentally in a steady air-water bubbly mixture. The instrument proved to be most valuable for two-phase flow applications, since it measures the average velocity of the continuous phase and not, as sometimes postulated, the liquid volumetric flow rate. The flowmeter not only performed well in a bubbly flow regime, but also in a churn turbulent flow, where the velocity profile is no longer axisymmetric. The RMS noise measurements also indicated that this instrument is suitable for unsteady two-phase flow, provided the magnetic field excitation frequency is adequate.

The other instrument investigated was the impedance void fraction meter. The motivation for choosing this method was twofold. First, the technique has potential for dynamic measurements,and second, the simplicity of its design and construction requires a minimal cost investment compared to the beam attenuation techniques. In order to improve its dynamic potential, we proceeded with a design of our own characterized by the use of short electrodes excited by voltages of opposite polarity and a very sensitive low-noise signal processor. However, as shown by the steady state calibration curves, the design is still somewhat sensitive to the void fraction distribution and change in flow regimes. Because little is said in the literature about the

dynamic capability of the impedance void fraction meter, a special effort was made to estimate the dynamic response of the present meter. This was accomplished by means of a statistical analysis of the fluctuating voltages in a nominally steady bubbly flow, in combination with a shot-noise model. The agreement between the statistical properties of the model and those measured experimentally permitted the determination of the time constant associated with the dominant filter of the void fraction meter. This filter is due to the finite volume swept by the electric field inside the fluid cell. Because of this volume, the dynamic capability of the void fraction meter is best characterized by the 3 dB attenuated wavelength in the output rather than the usual time constant of the filter which changes with the speed of the disperse phase. The large value of these wavelengths compared to the axial length of the electrodes illustrates that the fundamental problem affecting these devices is the axial dispersion of the electric field in the fluid. It was also shown that the shot-noise autocorrelation function evaluated at time zero contained information about various parameters of the disperse phase. The analytical expression was then used to estimate the average bubble diameter present in the disperse phase which agreed well with the one observed.

The other purpose of this thesis has been to investigate how the kinematic wave theory could be used to obtain information on the fluid mechanics of the disperse phase and its interaction with the continuous phase. This was accomplished by the detection of propagating kinematic shocks with a zero void fraction below the discontinuity. Various water volumetric fluxes were considered. The relative velocity

of the disperse phase calculated from these measurements was found to be a decreasing function of the void fraction. However, the increase in the water flux had the effect of reducing this dependency on the void fraction. The mechanism responsible for this behavior is thought to be an effect of the turbulence level, but this could not be verified. The shock technique could not be extended to water volumetric flux higher than 31.8 cm/s because of the significant error in determining the shock transit time. The experiment on propagating shocks of decreasing strength provided a good verification of the kinematic wave formulation. The measured speeds and those predicted were in good agreement. Furthermore, the dynamic capability of the void fraction meter allowed us to measure the thickness of the kinematic shock. It was observed that this thickness decreases with an increase of the shock strength. By including a diffusion term in the kinematic wave equation, the calculation of the shock thickness yielded a relation qualitatively similar to that observed. However, this term could not be justified from first principles.

Cross-correlation measurements of the fluctuating voltage of two void fraction meters in a nominally steady bubbly flow were presented. Using the results for kinematic shocks, it has been shown that the speed of the propagating structure is the infinitesimal kinematic wave speed and not the velocity of the disperse phase as previously believed. This finding leads to the conclusion that a natural system of small amplitude void fraction waves is present at all times in a steady bubbly flow. These waves, although not dispersive, are quickly damped as indicated by the normalized cross-correlation function. These

observations, along with the finite shock thickness, emphasize the existence of the diffusion mechanism within a bubbly two-component flow.

The air-water bubbly flow investigated in this thesis is a simple two-component flow. However, the instrumentation, the measurement techniques, and the experimental results indicate that they can be of some use in more complicated situations as in non-equilibrium liquid-vapor systems and three-component flows for which there is a fundamental lack of information. In the latter case, the possibility of measuring the volume fraction of the two disperse phases by taking advantage of the difference in their kinematic wave speed is worth investigating.

REFERENCES

1. Arave, A.E. and Fickas, E.T., 1979, "Progress Report on LOFT Ultrasonic Density Detector for Fuel Inlet Blowdown Measurements", Proceedings of the U.S. Nuclear Regulatory Commission, Review Group Meeting on Two-Phase Flow Instrumentation, March 13-14, 1979, Troy, N.Y., (NUREG/CP-0006).

2. Baker, J.L.L. and Chao, B.T. 1963, "An Experimental Investigation of Bubble Motion in Turbulent Liquid Stream", University of Illinois, Dept. of Mechanical and Industrial Engineering, Report ME-TN-1069-1, June 1963, Urbana, Illinois.

3. Batchelor, G.K., 1967, Fluid Dynamics, Cambrdige University Press.

4. Batchelor, G.K., 1972, "Sedimentation in a Dilute Dispersion of Spheres", J. Fluid Mech. 1972, Vol. 52, pp. 245-268.

5. Belblidia, L.A. and Batrianu, C., 1979, "Density Wave Oscillations", Annals of Nuclear Energy, 1979, Vol. 6, pp. 425-444.

6. Bouré, J.A., Bergles, A.E. and Tong, L.S., 1971, "Review of Two-Phase Flow Instabilities", ASME-AIChE Heat Transfer Conference, August 15-18, 1971, Tulsa, Okla.

7. Butterworth, D. and Hewitt, G.F., 1977, Two-Phase Flow and Heat Transfer, 1977, Oxford University Press, Chap 2.

8. Chernyy, I.M., 1973, Concerning the Dynamics of Bubble-Type Flows in Gas-Liquid Nozzle", Fluid Mechanics-Soviet Research, 1973, Vol. 2, No. 6, pp. 92-99.

9. Cimorelli, L. and Evangelisti, R., 1967, "The Application of the Capacitance Method for Void Fraction Measurement in Bulk Boiling Conditions", Int. J. Heat Mass Transfer, 1967, Vol. 10, pp. 277-288.

10. Cimorelli, L. and Evangelisti, R., 1969, "Experimental Determination of the Slip Ratio in a Vertical Boiling Channel, under Adiabatic Conditions at Atmospheric Pressure", Int. J. Heat Mass Transfer, 1969, Vol. 12, pp. 713-726.

11. Coughlin, J.L. and Brennan, M.F., 1980, "Control Valves for Erosion Services", The Proceedings of the 1980 Symposium on Instrumentation and Control for Fossil Energy Processes, June 9-11, 1980, (ANL 80-62, CONF-8000602).

12. Cushing, V., 1952, "Induction Flowmeter", The Review of Scientific Instruments, 1952, Vol. 29, No. 8, pp. 692-697.

13. Einstein,A., 1906, "Eine Bestimmung der Moleküldimensionen", Annalen der Physik, 1906, Vol. 19, p. 289-306.

14. Filderis V. and Whitmore, R.L., 1961, "The Physical Interaction of Spherical Particles in Suspensions", Rheologica Acta, 1961, Vol. 1, pp. 573-580.

15. Fitremann, M., 1972, "La Debitmétrie Electromagnétique Appliquée aux Emulsions", Société Hydrotechnique de France, XIImes Journées de l'Hydraulique, 1972, Question IV, Rapport 6, Paris.

16. Garrard, G. and Ledwidge, T.J., 1971, "Measurement of Slip Distribution and Average Void Fraction in an Air-Water Mixture", Australian Atomic Energy Research Establishment, 1971, Lucas Heights, Sutherland, N.S.W.

17. Glass, G. and Kadlec, J.,1976, "Survey of the Behavior of BWR Pressure Suppression Systems During the Condensation Phase of of a LOCA", Paper contributed to the American Nuclear Society, 1976, International Conference, Nov. 15-19, 1976, Washington, D.C.

18. Heineman, J.B., Marcheterre, J.F. and Mehta, S., 1963, "Electro-magnetic Flowmeters for Void Fraction Measurement in Two-Phase Metal Flow", The Review of Scientific Instruments, 1963, Vol.34, No. 34, pp. 399-401.

19. Herbich, J.B., 1975, Coastal and Deep Ocean Dredging, Gulf Publ. Co., Houston, p. 158.

20. Hewitt, G.F., 1972, "Role of Experiments in Two-Phase Flow with Particular Reference to Measurement Techniques", Progress in in Heat and Mass Transfer, Pergamon Press, 1972, Vol. 6.

21. Hewitt, G.F., 1978, Measurement of Two Phase Flow Parameters, Academic Press, New York.

22. Hori, M., Kobori, T. and Ouchi, Y., 1966, "Method for Measuring Void Fraction by Electromagnetic Flowmeters", JAERI-1111,August 1966.

23. Ishii, M., 1975, Thermo-Fluid Dynamics Theory of Two-Phase Flow, Eyrolles publication, Chapters 9 and 10.

24. Jallouk, P.A., Leavell, W.H., Shahrokhi, F. and Hardy, J.E., 1979, "Advanced Instrumentation for Reflood Studies", Proceedings of the U.S. Nuclear Regulatory Commission, Review Group Meeting on Two-Phase Flow Instrumentation, March 13-14, 1979, Troy, N.Y., (NUREG/CP-0006).

25. Jones Jr., O.C. and Delhaye, J.-M., 1976, "Transient and Statistical Measurement Techniques for Two-Phase Flows: A Critical Review", Int. J. Multiphase Flow, 1976, Vol. 3, pp. 89-113.

26. Kinch, G.J., 1952, "A Theory of Sedimentation", Trans. Faraday Society, 1952, Vol. 48, pp. 166-176.

27. Knapp, R.T., Daly, J.W. and Hammitt, F.G., 1970, Cavitation, McGraw-Hill.

28. Leviens, E.J., 1980, "Overview of The DOE Coal Conversion Program: Challenge for the 80's", The Proceedings of the 1980 Symposium on Instrumentation and Control for Fossil Energy Processes, June 9-11, 1980, (ANL-80-62, CONF-800602).

29. Liepmann, H.W. and Roshko, A., 1957, Elements of Gas Dynamics, John Wiley and Sons.

30. Lighthill, M.J. and Whitham, G.B., 1955, "On Kinematic Waves, I-Flood Movement in Long Rivers", Proceedings of the Royal Society, 1955, Vol. 229, pp. 281-316.

31. Lighthill, M.J. and Whitham, G.B., 1955, "On Kinematic Waves, II-A Theory of Traffic Flow on Long Crowded Roads, 1955, Vol. 6, pp. 317-347.

32. Lockhart, R.W. and Martinelli, R.C., 1949, "Proposed Correlation of Data for Isothermal Two-Phase, Two-Component Flow in Pipes", Chem. Engng. Progress 1940, Vol, 45, No. 1, pp. 39-48.

33. Maxwell, J.D., 1881, A Treatise on Electricity and Magnetism, Clarendon Press, Oxford, Vol. 1. p. 435, 2nd Ed.

34. Meridith, R.E. and Tobias, C.W., 1960, "Resistance to Potential Flow Through a Cubical Array of Spheres", J. App. Phys., 1960, Vol. 34, No. 7.

35. Merilo, M., Dechene, R.L. and Cichowlas, W.M., 1977, "Void Fraction Measurement with a Rotating Electric Field Conductance Gauge", Transactions of the ASME, May 1977, Vol 99, p. 330-332.

36. Nicklin, D.J., 1962, "Two-Phase Bubbly Flow", Chemical Engineering Science, 1962, Vol. 17, pp. 693-702.

37. Olsen, H.O., 1967, "Theoretical and Experimental Investigation of Impedance Void Meters", Institutt for Atomenergi, Kjeller Research Establishment, August 1967, Kjeller, Norway.

38. Orbeck, I., 1962, "Impedance Void Meter", Institutt for Atomenergi, Kjeller Research Establishment, November 1962, Kjeller, Norway.

39. Papoulis, A., 1965, Progability, Random Variables, and Stochastic Processes, McGraw-Hill.

40. Prosperetti, A. and Van Wijngaarden, L., 1976, "On the Characteristics of the Equations of Motion for Bubbly Flow and the Related Problem of Critical Flow", Journal of Engineering Mathematics, 1976, Vol. 10, pp. 153-162.

41. Schrock,V.E. and Selph, F.B., 1963, "Reactor Heat Transient Research. An X-ray Densitometer for Transient Steam-Void Measurement", U. California Inst. Engng. Report No. SAN-1005, TID-4500, 1963.

42. Shercliff, J.A., 1962, The Theory of Electromagnetic Flow-Measurement, Cambridge University Press.

43. Symington, W.A., 1978, "Analytical Studies of Steady and Non-Steady Motion of a Bubbly Liquid", Ph.D. Thesis, California Institute of Technology, May 1978.

44. Taylor, D.G., Porter, E.H. and Orvis, W.J., 1979, "PBF Radiation Hardened Gamma Densitometer", Proceedings of the U.S. Nuclear Regulatory Commission, Review Group Meeting on Two-Phase Flow Instrumentation, March 13-14, 1979, Troy, N.Y. (NUREG/CP-0006).

45. Wallis, G.B., 1962, "A Simplified One-Dimensional Representation of Two Component Vertical Flow and Its Application to Batch Sedimentation", Proc. Symp. on Interaction Between Fluid and Particles, Inst. of Chem. Engrs., 1962, London.

46. Wallis, G.B., 1969, One Dimensional Two-Phase Flow, McGraw-Hill, New York.

47. Weiner, O., 1912, "Die Theorie des Mischkörpers für das Feld der Stationären Strömung, Abh. Sächs. Ges.d.Wiss., Math.-Phys., 1912, Kl.32.S.509.

48. Zuber, N., 1964, "On the Disperse Two-Phase Flow in Laminar Flow Regime", Chemical Engineering Science, 1964, Vol. 19, pp. 897-917.

49. Zuber, N. and Staub, F.W., 1966, "The Propagation and Wave Form of the Vapor Volumetric Concentration in Boiling Forced Convection System Under Oscillatory Conditions", Journal of Heat Transfer, 1966, Vol. 9, pp. 871-895.

50. Zuber, N. Staub, F.W., Bijwaard, G. and Kroeger, P.G., 1967, "Steady State and Transient Void Fraction in Two-Phase Flow Systems-Final Report for the Program of Two-Phase Flow Investigation", EURAEC GEAP-5417, Volume I, January 1967.

51. Zun, I., 1980, "The Transverse Migration of Bubbles Influenced by Walls in Vertical Bubbly Flow", Int. J. Multiphase Flow, 1980, Vol. 6, pp. 583-588.

Appendix A - TECHNICAL DESCRIPTION OF THE SIGNAL PROCESSOR

A.1 Content

The present appendix includes a description of the void fraction meter electronics, circuit diagrams, and a list of components (Table A.1). Illustrated in Fig. A.1 is the functional block diagram, showing the three major units of the design. These are:

    i)   The sine wave generator;

    ii) The bridge;

    iii) The signal conditioner.

Each unit is a collection of standard circuits built around operational amplifiers.

A.2 Sine Wave Generator

The sine wave generator diagram is shown in Fig. A.2. The basic circuits used are:

1. Variable frequency Wein Bridge Oscillator,(A1),

2. Half-wave rectifier, (A2),

3. Integrator, (A3),

4. WBO follower, (A4),

5. 20-40 dB attenuator, (A5),

6. Attenuator follower, (A6).

The amplitude regulation of the Wein Bridge Oscillator (WBO) is accomplished by an active gain control made of the half-wave rectifier, the integrator, and a Field Effect Transistor (FET) used as a variable

resistor which is part of the negative feedback loop of the WBO. A D.C. bias voltage acting on the FET provides the coarse adjustment of the WBO signal amplitude, while the 20-40 dB attenuator was used as a means of fine adjustment. The range of the sine wave amplitude available at the output is .02 to 1 V rms for frequencies between 10 and 100 KHz.

A.3 Bridge

As mentioned in Chapter 3, the bridge is made of two bridges acting independently. The bridge circuit diagram shown in Fig. A.3 is composed of

1. Inverting amplifier, (A7),

2. Non-inverting amplifier, (A8),

3. 2 bridges.

Each electrode in contact with the fluid is part of a bridge. The two bridges share a common variable resistor in parallel with a variable capacitor. These two elements are needed to null the bridge prior to the injection of the gas phase. The capacitance of the water being small, the function of the variable capacitor is mainly to account for the parasitic capacitances of the processor and the BNC cables. The directionality of the electric field inside the fluid cell is ensured by inverting the excitation voltage of one of the bridges. The 180° phase between the voltage of each electrode is accomplished by means of non-inverting and inverting amplifiers having a gain of 10. The inverting amplifier is provided with a trimmer to adjust its output amplitude to the non-inverting amplifier.

A.4 Signal Conditioner

Figure A.4 illustrates the signal conditioner circuit. This unit is conveniently broken down into the following basic circuits:

1. Instrument differential amplifiers, (A9 to A14),
2. Variable gain adder, (A15),
3. Carrier amplifier, (A16),
4. Multiplier, (M1),
5. Two-pole Butterworth low pass filter, (A17),
6. D.C. output amplifier, (A18),
7. D.C. follower, (A19),
8. A.C. follower, (A20).

Subsequent to a change in the resistance of the fluid cell, the unbalanced voltage of each bridge is processed through an Instrument Differential Amplifier (IDA) with a two-stage 30 dB amplification. The particular configuration of this amplifier yields a high Common Mode Rejection Ratio (CMRR). The inputs of one of the IDAs are inverted to obtain output voltages with the same polarity prior to their addition in the Variable Gain Adder (VGA). The variable gain of the adder is provided to adjust the full scale response of the meter which is determined by the bubbly-to-churn-turbulent transition point for zero water flux. The VGA signal output is directed to a follower whose signal can be displayed on the oscilloscope for zeroing the bridge. The VGA signal is further processed by a demodulator circuit. The amplitude demodulation is obtained by multiplying the VGA output with a signal of the same

frequency and constant amplitude. This signal is provided by the carrier amplifier whose input is tapped from one of the bridge voltage sources. The multiplier output yields a signal at twice the input signal frequency with a D.C. offset proportional to the amplitude of the unbalanced voltage measured at the bridge. The high frequency content is then removed by a two-pole low pass Butterworth filter with a 3 dB cut-off frequency of 500 Hz. After a final amplification of 20 dB, the D.C. signal is routed to a follower and is then available for measurement.
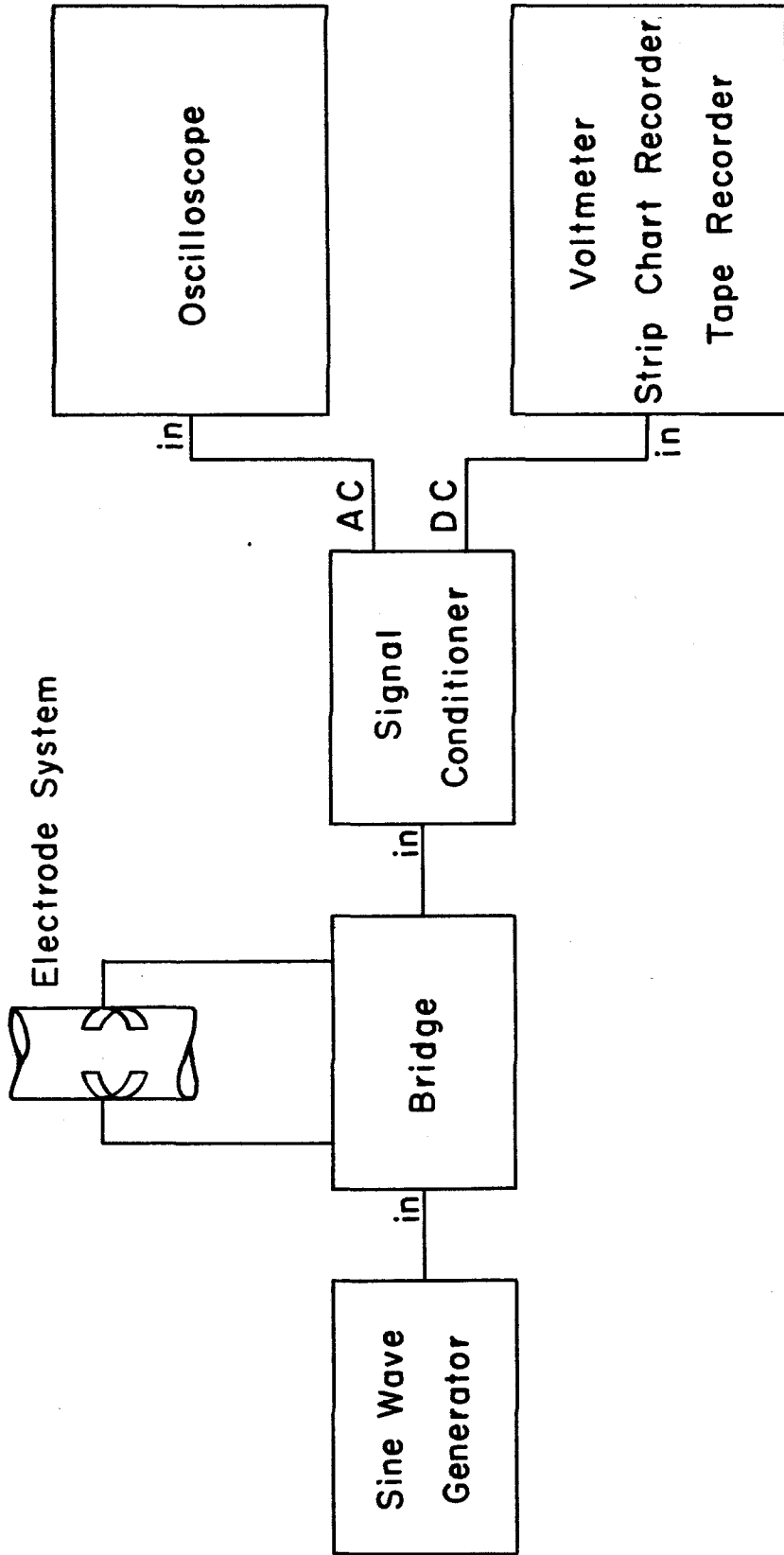
Figure A.1   Schematic diagram of the impedance void fraction meter major systems; the sine wave generator, the bridge and the signal conditioner.
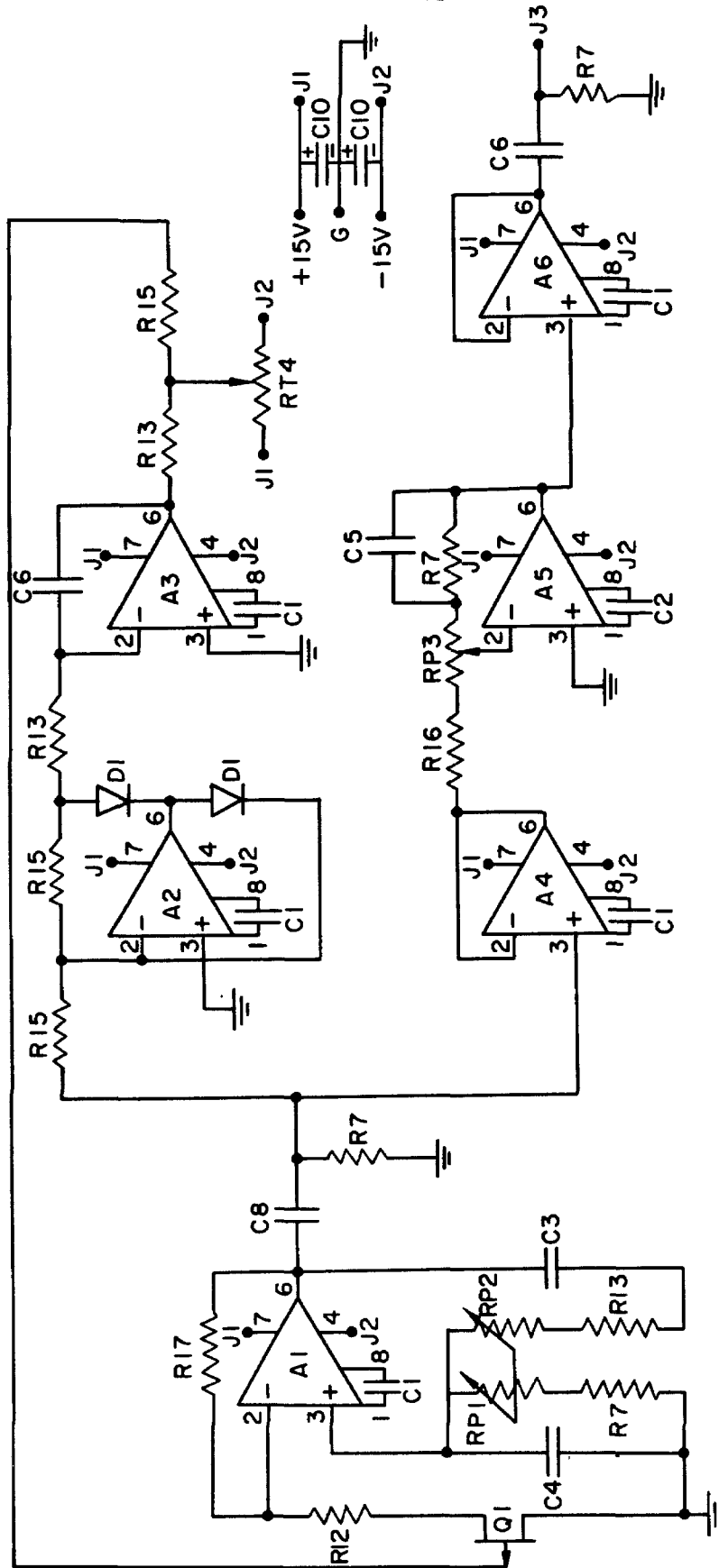
Sine Wave Generator

Figure A.2 Circuit diagram of the sine wave generator. The particular function of the operational amplifiers A1 to A6 is described in Appendix A. The component values are listed in Table A.1.

-149-
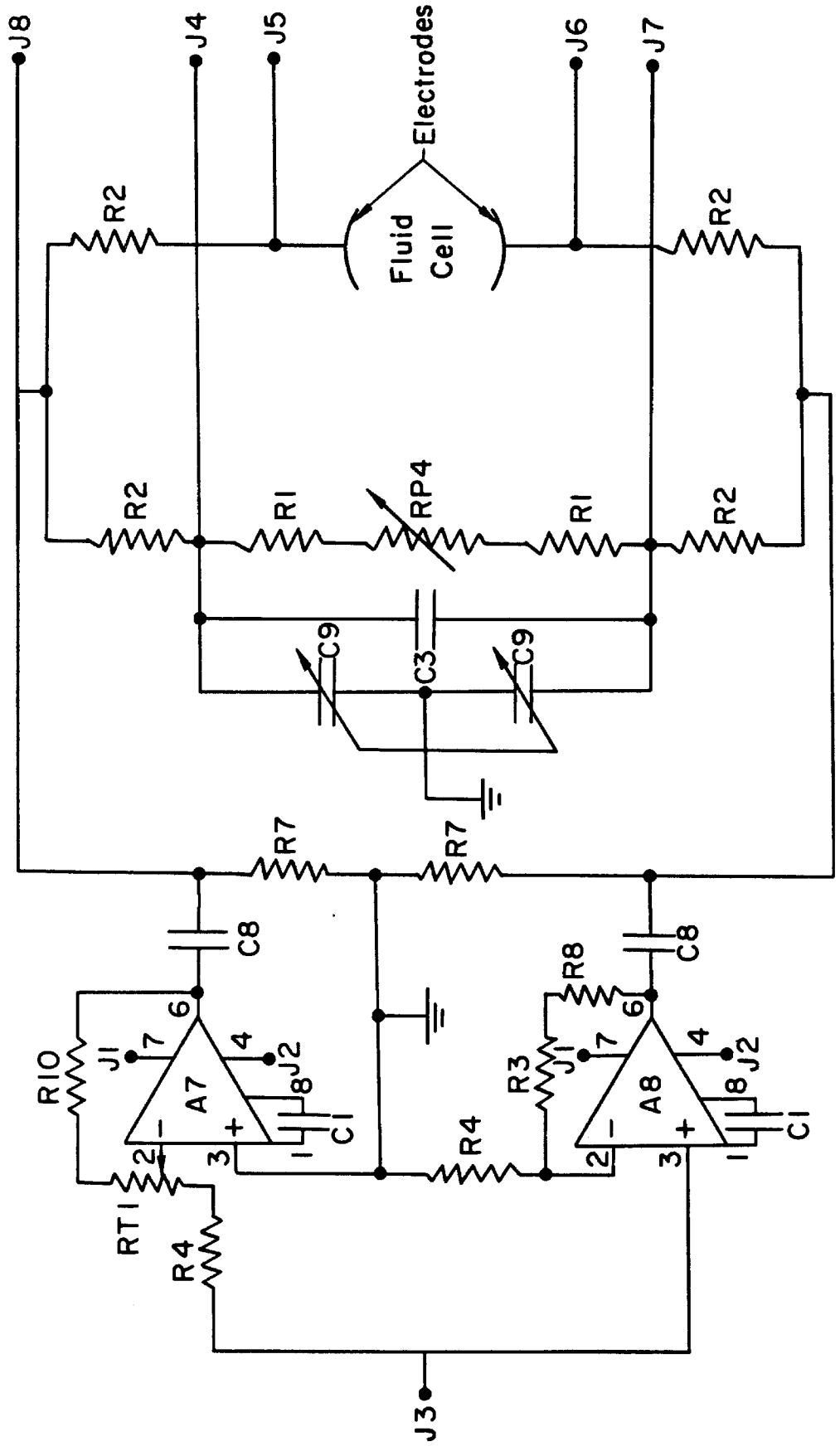
Bridge

Figure A.3   Circuit diagram of the bridge. The particular function of the operational amplifiers A7 and A8 is described in Appendix A. The component values are listed in Table A.1.
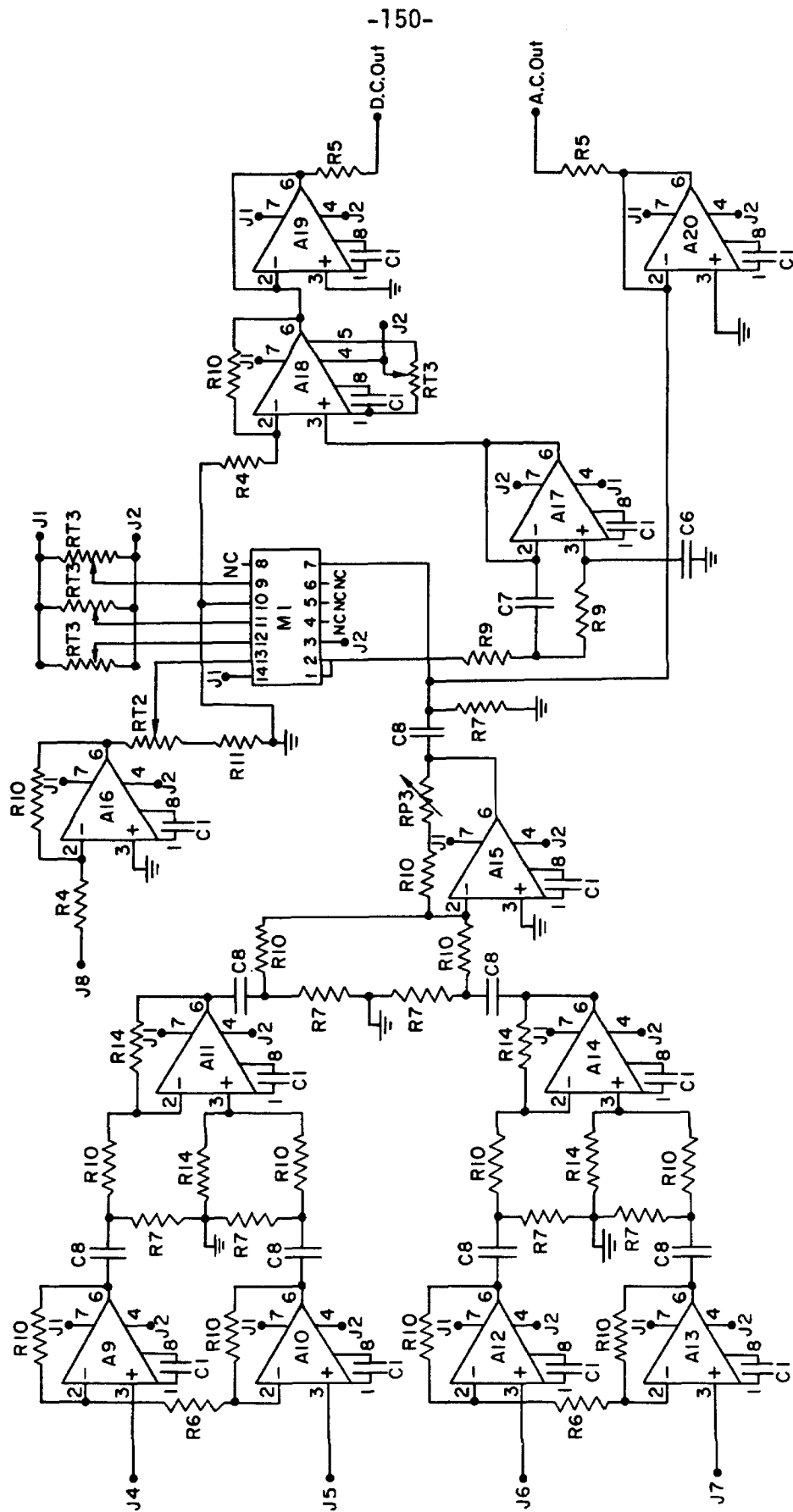
Signal Processor

Figure A.4 Circuit diagram of the signal conditioner. The particular function of the operational amplifiers A9 to A20 is described in Appendix A. The component values are listed in Table A.1.

TABLE A.1

Resistor	Value	Quantity	Description
R1	10 Ω	2	
R2	20 Ω	4	
R3	162 Ω	1	
R4	221 Ω	4	
R5	619 Ω	2	
R6	825 Ω	2	
R7	1.0 KΩ	13	
R8	1.82 KΩ	1	
R9	2.15 KΩ	2	All 1% - .25 W
R10	2.21 KΩ	14	
R11	4.99 KΩ	1	
R12	7.5 KΩ	1	
R13	10.0 KΩ	3	
R14	11.0 KΩ	4	
R15	20.0 KΩ	3	
R16	100.0 KΩ	1	
R17	200.0 KΩ	1	

Trimmer

RT1	100 Ω	1	
RT2	5 KΩ	1	
RT3	10 KΩ	4	All 10 turns
RT4	1 MΩ	1	

Potentiometer

RP1	10 K	1	5% Cermet, 1 Watt, 16 turn Vernier ⎫ Dual
RP2	100 K	1	5% " " " " ⎭
RP3	10 K	3	10 turns W.W.
RP4	1 K	1	10 turns W.W.

Table A.1.   List of the electrical components used in the construction of the impedance void fraction meter.

TABLE A.1 (Continued)

Capacitor	Value	Quantity	Description
C1	15 pf	19	10% ceramic, 50 WVDC
C2	25 pf	1	" " " "
C3	150 pf	2	10% mica, 100 WVDC
C4	1.5 nf	1	" " " "
C5	10.0 nf	1	10% uramic, 50 WVDC
C6	100.0 nf	3	10% " " "
C7	200.0 nf	1	10% " " "
C8	470.0 nf	10	10% ceramic, 50 V WVDC
C9	0-100 pf	2	Dual Air Capacitor
C10	15 μf	2	Tantalum, 20 V

Diode

D1	1 N 5252	2	All purpose

Transistor

Q1	2 N 5462	1	Field effect transistor

Operational Amplifiers

A1-A20	RCA 3100	20	

Multiplier

M1	AD 530 JD	

D.C. Power Supply

±15V - 700 ma